Report No. 772

INVESTIGATION OF THE EFFECTS OF PILE JETTING AND PREFORMING

State Project 99700-3304-010
WPI 0510727
FL/DOT/RMC/B-9479

M.Gunaratne, Ph.D., P.E., R.A. Hameed, Ph.D. and C.Kuo, Ph.D., P.E.

Department of Civil and Environmental Engineering
College of Engineering
University of South Florida
Tampa, Florida 33620

D.V. Reddy, Ph.D., P.E.

College of Engineering
Florida Atlantic University
777 Glades Road
Boca Raton, FL 33431-0991

and

Sastry Putcha, Ph.D., P.E.
State Geotechnical Construction Engineer
FDOT

July 1999

FINAL REPORT

Document is available to the U.S. public through the
National Technical Information Service
Springfield, Virginia 22161

prepared for the

FLORIDA DEPARTMENT OF TRANSPORTATION

and the

U.S. DEPARTMENT OF TRANSPORTATION
FEDERAL HIGHWAY ADMINISTRATION

INVESTIGATION OF THE EFFECTS OF PILE JETTING AND PREFORMING

M.Gunaratne, R.A. Hameed and C.Kuo

Department of Civil and Environmental Engineering
College of Engineering
University of South Florida
Tampa, Florida 33620

D.V. Reddy

College of Engineering
Florida Atlantic University
777 Glades Road
Boca Raton, FL 33431-0991

Sastry Putcha, Ph.D., P.E.
State Geotechnical Construction Engineer
FDOT

July 1999

CONVERSION FACTORS
U. S. CUSTOMARY TO METRIC (SI) UNITS OF MEASUREMENT

U. S. customary units of measurement used in this report can be converted to metric (SI) units as follows:

MULTIPLY	BY	TO OBTAIN
inches	2.54	centimeters
feet	0.3048	meters
square inches	6.4516	square centimeters
inches/second	2.54	centimeters/second
feet/second	0.3048	meters/second
cubic feet/second	0.02831685	cubic meters/second
pounds (mass)	0.4535924	kilograms
pounds (force)	4.448222	newtons
kips (1000 pounds)	4448.222	kilograms
pounds/sq. inch	6894.757	pascals
pounds/cubic foot	16.0185	kilograms/cubic meter
tons/square foot	9764.86	kilograms/square meter
kips/square inch	6894757	kilopascals

1. Report No.	2. Government Accession No.	3. Recipient's Catalog No.
727		

4. Title and Subtitle
nvestigation of the effects of pile jetting and performing

5. Report Date
July 1999

6. Performing Organization Code
FL/DOT

8. Performing Organization Report No.
USF contract 2104-224-L0

7. Authors
Hameed, R.A., Kuo, C., Reddy, D.V., and Sastry, P.

9. Performing Organization Name and Address
Department of Civil and Environmental Engineering
University of South Florida
4202 E. Fowler Avenue
Tampa, FL 33620-5350

Dept. of Ocean Engineering
Florida Atlantic University
777 Glades Rd.
Boca Raton, FL 33431

10. Work Unit No. (TRAIS)

11. Contract or Grant No.
B-9479

13. Type of Report and Period Covered
Final Report
January 1995 - July 1999

12. Sponsoring Agency Name and Address
Florida Department of Transportation
Office of Research Management
Tallahassee, FL 32399-0450

14. Sponsoring Agency Code
FHWA

15. Supplementary Notes
Prepared in cooperation with FHWA

16. Abstract
Both jetting and preforming of piles cause substantial disturbance to the surrounding soil resulting in a notab change in the lateral load behavior. This report presents the results of an experimental study performed with simil model piles installed using (1) impact driving (2) jetting and (3) preforming in a sandy soil (with 10% cla compacted to different unit weights under unsaturated and saturated conditions. The effects of jetting pressure ar preformed borehole diameter on the lateral load behavior of piles are presented in terms of normalized desig curves. In addition, a computational model that can predict the effects of preforming on the lateral load behavi of piles is also formulated. Then, the measured load-deformation behavior of preformed piles is compared to t computational predictions. The zone of influence of jetting on existing piles is also explored. This is achiev through a testing program where the effects of axial and lateral load characteristics of existing driven piles, due jetting of other piles at designated locations, are monitored. The results indicate that the influence of jetting *und dry soil conditions* extends up to about five times the pile diameter with respect to the lateral load characteristic On the other hand, no significant jetting influence zone was detected in *completely saturated* soils.

17. Key Words
jetting, preforming, lateral loading, pile

18. Distribution Statement
Document is available to the U.S. Public through the National Technical Information Service, Springfield, VA 22161

19. Security Classif.(of this report)	20. Security Classif. (of this page)	21. No. of Pages	22. Price
Unclassified	Unclassified	122	

Form DOT F 1700.7 (8-72)

Acknowledgment

The authors are indebted to Dr. Sastry Putcha , FDOT State Construction Geotechnical Engineer for continued guidance, support and inspiration throughout the entire research period. The FDOT grant B-9479 is gratefully acknowledged as well.

TABLE OF CONTENTS

LIST OF TABLES iii

LIST OF FIGURES v

ABSTRACT viii

CHAPTER 1 PROBLEM STATEMENT

1.1 Introduction 1
1.2 Problem Statement 2
1.3 Scope of Study 4
1.4 Organization 5

CHAPTER 2 LATERAL LOAD BEHAVIOR OF JETTED PILES

2.1 Introduction 6
2.2 Theoretical Aspects of Model Testing 7
2.3 Experimental Details of Model Testing 10
2.3.1 Evaluation of Results 17
2.3.2 Numerical Example 34
2.4 Conclusions 37

CHAPTER 3 LATERAL LOAD BEHAVIOR OF PREFORMED PILES

3.1 Introduction 39
3.2 Experimental Details of Model Preformed Pile Testing 40
3.2.1 Evaluation of Test Results 46
3.2.2 Numerical Example 58
3.3 Numerical Modeling of the Lateral Load Behavior of Preformed piles 60
3.3.1 Introduction 60
3.3.2 Estimation of Existing Confining Stress 61
3.3.3 Material Constitutive Laws 72
3.3.3.1 Pile Model 72
3.3.3.2 Soil Model 73

	3.3.3.3 Interface Model	76
	3.3.4 The Finite Element Mesh	80
	3.3.5 Stages in the Finite Element Analysis	80
	3.3.6 Numerical Analysis	82
3.4	Conclusions	87

CHAPTER 4 INVESTIGATION OF THE JETTING INFLUENCE ZONE

4.1	Introduction	89
4.2	Experimental Details	90
	4.2.1 Axial Load Test Results	94
	4.2.1.1 Unit Load-Transfer Characteristics	97
	4.2.2 Lateral Load Test Results	103
	4.2.2.1 Lateral Load-Transfer Characteristics	106
4.3	Finite Element Model	111
	4.3.1 Analysis for the lateral Spread of Pore Pressure Due to Pile Jetting	112
	4.3.2 Load testing of Piles	113
4.4	Conclusions	115

REFERENCES 116

Appendix A 118

LIST OF TABLES

Table 2.1	Applicable model variables	8
Table 2.2	Definition of Pi terms	9
Table 2.3	Engineering properties of foundation soil	11
Table 2.4	Nomenclature used for piles in the testing program	13
Table 2.5	Influence of pile installation procedure on lateral capacities	16
Table 2.6	Comparison of curve fitted K_{max} and p_u values	28
Table 2.7	Constants for Eqns. (2.9) and (2.10)	33
Table 2.8	Interpolated constants for use in Eqns. (2.9) and (2.10)	36
Table 3.1	Nomenclature used for preformed piles in the testing program	41
Table 3.2	Influence of pile installation procedure on lateral capacities	43
Table 3.3	Comparison of curve fitted K_{max} and p_u values	55
Table 3.4	Parameters for Eqns. (3.3) and (3.4)	58
Table 3.5	Interpolated constants for use in Equs. (3.3) and (3.4)	60
Table 3.6	E_i and $(\sigma_1-\sigma_2)_f$	64
Table 3.7	σ_c and ε_x	70
Table 3.8	Initial elastic moduli used in modeling	71
Table 3.9	Basic properties of aluminum model pile	72
Table 3.10	E and τ_f	77
Table 3.11	Interface element stiffness	79

Table 3.12	Interface element stiffness (soft material)	79
Table 4.1	Nomenclature used for piles in the testing program	91
Table 4.2	Influence of driven pile spacing on axial capacities	94
Table 4.3	Influence of driven pile spacing on lateral capacities	103

LIST OF FIGURES

Figure 1.1	Configuration of a typical jet hole	3
Figure 2.1	Permeability vs dry density	10
Figure 2.2	Friction angle vs dry density	11
Figure 2.3	Test pit and hammer frame system	12
Figure 2.4	Water jet system	14
Figure 2.5	Lateral load test setup	15
Figure 2.6	Lateral load vs lateral displacement at 0.12 m (5 inch) from ground surface	17
Figure 2.7	Relative rigid vs flexible pile behavior	18
Figure 2.8	Polynomial fitted measured strain data	21
Figure 2.9	Calculated pile displacement	21
Figure 2.10	Calculated soil pressure	22
Figure 2.11	Measured and calculated lateral load displacement	23
Figure 2.12	p-y curves	24
Figure 2.13	Variation of K_{max} vs z/D	27
Figure 2.14	Variation of p_u vs z/D	28
Figure 2.15	Normalized p-y curves	30
Figure 2.16	Non dimensional K ratio vs jetting pressure	32
Figure 2.17	Non dimensional p_u vs jetting pressure	33
Figure 2.18	Schematic presentation of load transfer relationship	35

Figure 2.19	Predicted p-y curves	37
Figure 3.1	Schematic diagram of Preformed pile	41
Figure 3.2	Auger used in this study	42
Figure 3.3	preformed 50.8 mm (2.0 inch) hole and pile	43
Figure 3.4	Component of soil resistance	44
Figure 3.5	Lateral load vs lateral displacement of Preformed piles	45
Figure 3.6	Principle of p-y curves	46
Figure 3.7	Stress on the pile segment	47
Figure 3.8	Polynomial fit pile strain data vs depth (γ_d = 16.2 kN/m^3 – Unsaturated)	49
Figure 3.9	Calculated pile displacement vs depth (γ_d = 16.2 kN/m^3 – Unsaturated)	49
Figure 3.10	Calculated soil pressure vs depth (γ_d = 16.2 kN/m^3 – Unsaturated)	50
Figure 3.11	Comparison of measured and analytical load-displacement behavior	50
Figure 3.12	p-y curves	51
Figure 3.13	Variation of K_{max} and p_u with depth	53
Figure 3.14	K-ratio and p_u-ratio	56
Figure 3.15	Predicted p-y curves	59
Figure 3.16	Drained test results on test pit soil at different confining pressure	63
Figure 3.17	Variation of E_i vs σ_c	65
Figure 3.18	Isotropic triaxial compression test results	66
Figure 3.19	$(\varepsilon_v)_{failure}$ vs $(\sigma_c)^{0.78}$	67
Figure 3.20	Normalized stress-strain curve	71

Figure 3.21	Modified Drucker-Prager Cap model: yield surface in the p-t plane	73
Figure 3.22	Typical yield/flow surface in the deviatoric plane	74
Figure 3.23	Undrained Triaxial test paths for the tested clayey sand in the p-t plane	75
Figure 3.24	CD direct shear test results	76
Figure 3.25	E vs σ_N	78
Figure 3.26	Finite Element Mesh (Plan and Elevation)	81
Figure 3.27	Computed lateral load-displacement curve	82
Figure 3.28	Distribution of strain	84
Figure 3.29	Pile lateral displacement	85
Figure 3.30	Deflected pile shape with pile-soil separation	86
Figure 4.1	Overlapping of influence zones of a pile group	89
Figure 4.2	Model pile test setup	91
Figure 4.3	Jetting at a pile adjacent to an axially loaded driven pile	92
Figure 4.4	Isolated driven pile arrangement	93
Figure 4.5	Axial load setup	94
Figure 4.6	Axial load test results	95
Figure 4.7	Strain distribution along the pile IUD$_1$	98
Figure 4.8	f-w and q-w relation ship	99
Figure 4.9	Lateral load and lateral displacement	104
Figure 4.10	Cavity due to jetting	105
Figure 4.11	p-y curves for long and short pile	106
Figure 4.12	8-node composite type element used in the analysis	111

ABSTRACT

In pile installation, water jetting and preforming can be utilized as effective aids to impact driving whenever hard strata are encountered above the designated pile tip elevation. In the case of jetting, the immediate neighborhood of the pile is first liquefied due to high pore pressure induced by water jetting and subsequently densified with its dissipation. In addition, the percolating water also creates a filtration zone further away from the pile. Hence jetting invariably causes substantial disturbance to the surrounding soil which results in a notable change in the expected lateral load behavior. The first part (Chapter 2) of this report presents the results of an experimental study performed with similar model piles installed using (1) impact driving and (2) jetting in a sandy soil (with 10% clay) compacted to different unit weights under unsaturated and saturated conditions. The beam theory and polynomial approximations are used to convert measured load-strain data to conventional lateral load characteristics (p-y curves). Then, the effect of jetting pressure on the lateral load behavior of piles is presented in terms of normalized design curves.

In the case of preforming (preboring), due to the removal of insitu confining stress, a substantial disturbance is caused in the surrounding soil resulting in a significant change in the lateral load behavior of driven piles. The second objective of this research project was to quantify the possible reduction in the lateral load behavior of driven piles when preforming is employed as an aid to driving. The second part (Chapter 3) of this report presents the results of the above described model study extended to piles preformed under

different borehole diameters. The effect of the preformed borehole diameter on the lateral load behavior is also presented in terms of normalized design curves. In addition, a computational model that can predict the effects of preforming on the lateral load behavior of piles is also formulated. In this model, the embedded pile and the foundation soil are modeled by *8-node brick* type finite elements. The pile material is considered to be *elastic-perfectly plastic* while the soil stress-strain behavior is represented by the *Drucker-Prager cap model*. Further, specially designed *interface elements* are utilized to accurately model the finite deformation and slipping at the pile/soil interface during lateral loading. Moreover, the effect of the diameter of the preformed borehole is incorporated by introducing the corresponding initial driving stresses computed by the cavity expansion theory. Then, the measured load-deformation behavior of preformed piles is compared to the computational predictions.

The final objective of the research project was to investigate the zone of influence of jetting on existing piles. This is achieved through an additional model testing program that involved monitoring the effects of axial and lateral load characteristics of existing driven piles, due to jetting of other piles at designated locations in the neighborhood. The results indicate that the influence of jetting extends up to about five times the pile diameter with respect to the lateral load characteristics.

CHAPTER 1

PROBLEM STATEMENT

1.1 Introduction

An understanding of the soil-structure interaction is the key to rational and economical design of laterally loaded deep foundations. However, this understanding is difficult to transform into a general design methodology because of the inherent soil non-linearity and non-homogeneity enhanced by the three-dimensional, asymmetric nature of the problem. These difficulties have led to a variety of design methods, approaches, and recommendations. Such issues are even more conspicuous when one deals with deep foundations installed using numerous construction techniques.

Although the behavior of deep foundations is influenced by the method of construction (driving, jetting, preforming, etc.), the same general design analysis procedure should be applicable to all cases, as long as a "method of construction" factor is included. The procedures generally used in practice do not include a "method of construction" factor explicitly. However, this factor could be considered as being included indirectly wherever back-calculated soil properties and design parameters are used to develop the design method.

In the currently available procedures employed for design of jetted and preformed piles, technically derived factors to account for the method of construction are not incorporated. Hence a research program was needed to investigate the effects of the

common pile construction techniques of jetting and preforming on the lateral load design capacities.

1.2 Problem Statement

As a general practice, Florida Department of Transportation (FDOT) uses either pile jetting or preforming to install piles in construction situations where hard soil strata are encountered above the minimum pile tip elevation or the estimated tip elevation required to obtain adequate bearing. These techniques are also utilized under conditions where control of construction vibration is essential which becomes a critical issue during pile driving operations amidst structures within a city zone. In general, wherever appropriate, installation of piles by means of jetting or preforming should accomplish major construction time and cost savings. This can be achieved only when the uncertainties and empiricism in evaluating the pile capacities and settlements associated with the above techniques are eliminated or at least minimized.

Due to the excessive water velocity introduced in jetting soil in the immediate neighborhood is eroded thus creating a narrow water path along which eroded material is brought to the surface. In addition, the portion of water that is unable to escape penetrates the intact soil mass thereby liquefying it (liquefaction zone in Fig. 1.1) due to the high pressure. The presence of a low strength zone adjacent to the pile certainly eases driving. Subsequently this zone is densified due to driving vibrations and dissipation of excess pore pressure. Therefore, the original soil structure is invariably altered. Hence, although pile jetting may be an effective alternative to hammer driving as a penetration aid in

saving time and energy, the accompanying reduction in friction and lateral load capacities in comparison to hammer driven piles is a predominant limitation of the technique.

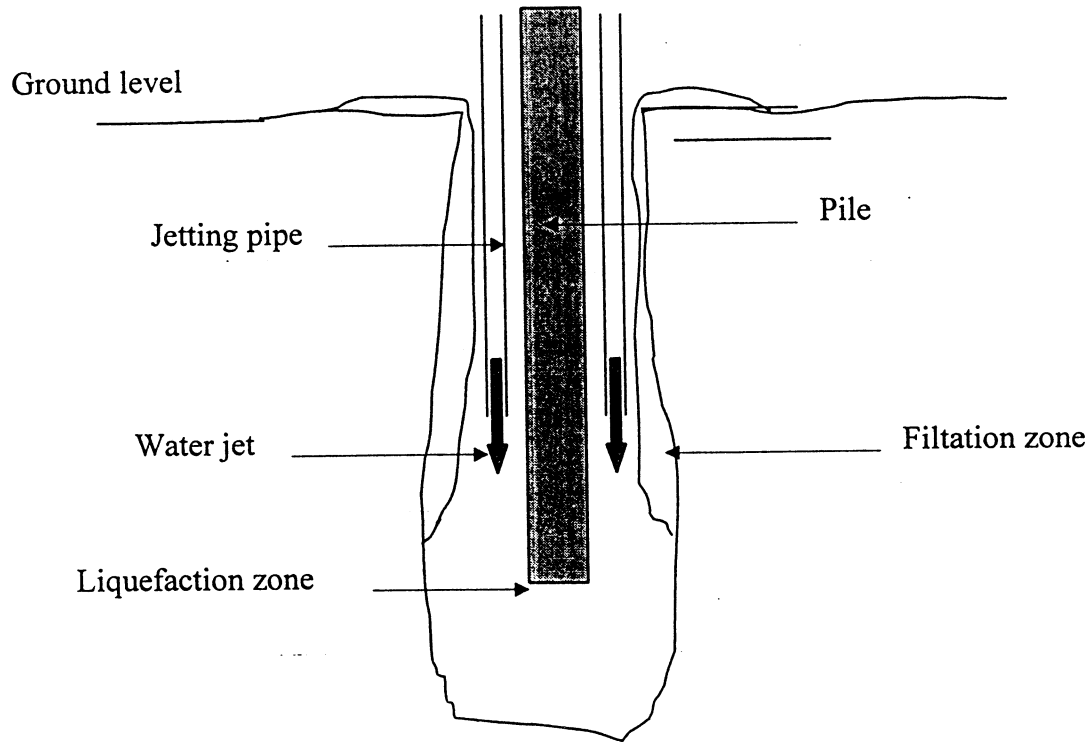

Figure 1.1 Configuration of a typical jet hole

In addition, the large volumes of water used in jetting can cause problems by undermining the neighboring piles or other structures as it escapes toward the surface. During the jetting process some water also infiltrates into the adjacent area (filtration zone in Fig. 1.1) maintaining a high pore pressure. Thus, the combined liquefaction and filtration zones known as the zone of influence of jetting could affect the load carrying capacities of the adjacent piles in a pile group.

Structurally intact bridges are often widened to meet increasing traffic demand. Currently, when jetting is utilized to install the additional piles required to support the expanded bridge, the safe zone of jetting is determined based on subjective judgment of the designers and the consultants in the absence of well defined technical criteria. Furthermore, the issue of the reduction in skin-friction and the lateral load capacities due to jetting themselves are currently resolved using arbitrary criteria. Similarly, the FDOT does not account for possible strength changes induced in different soil types during preforming. Adoption of such subjective and arbitrary guidelines can result in either conservative over-prediction or risky under-prediction of the impact of jetting or preforming. Hence, a research that can clearly identify the extent of the influence zone of jetting and the effects of jetting and preforming on the lateral and skin friction capacities of piles is essential to the utilization of these two techniques as effective penetration aids to pile installation in the ground.

1.3 Scope of Study

In this study, the drained behavior of model aluminum piles subjected to monotonic lateral and axial loading is evaluated with the following goals:

1. Experimental Investigation of (a) the effects of jetting on the skin-friction capacities of piles; (b) the effects of preforming on the skin-friction capacities of pile; (c) the effects of jetting on the subgrade modulus, lateral load capacity and deflection of pile; (d) the effects of preforming on the subgrade modulus, lateral load capacities and deflection of pile.

2. Exploration of the zone in which pile jetting can affect the load carrying capacity of an existing pile foundation.
3. Examination of the soil strength changes due to impact of the jetting and preforming.
4. Formulation of analytical models to quantify effects of jetting and preforming based on the test data.

CHAPTER 2

LATERAL LOAD BEHAVIOR OF JETTED PILES

2.1 Introduction

Although driven piles are installed in the ground mostly by impact driving, jetting can be used as a driving aid when hard soil strata are encountered above the designated minimum pile tip elevation or the estimated tip elevation required to obtain adequate bearing. However, the final set is usually obtained by impact driving the last few meters without jetting. This practice is often desirable since the dynamic driving action effectively increases the density of the soil medium surrounding the pile tip, thus restoring the possible loss of axial load bearing capacity due to jetting. Yet, it has been reported (Tsinker, 1988) that impact driven piles have better load bearing characteristics than jetted-driven piles under comparable soil conditions. This may be due to the fact that the soil in the immediate neighborhood is first liquefied and subsequently remolded as a result of the excessive water velocity introduced in jetting and the dissipation of excess pore pressure, thereby altering the original in-situ soil structure and the skin-friction characteristics.

The primary objectives of the first phase of the experimental program was to gain a deeper understanding of the lateral load performance of driven and jetted-driven model piles installed under the same in-situ soil conditions. This objective was achieved by, (a) determining the normalized experimental load transfer curves (p-y curves) along the pile depth and comparing the p-y curves of driven piles to those of jetted-driven piles, (b)

exploring the effect of jet water pressure, soil unit weight and saturated conditions on the p-y characteristics. The second objective of this phase of the experiment was to develop approximate guidelines for predicting the lateral load behavior of jetted piles based on that of impact driven piles, under the same soil conditions.

2.2 Theoretical Aspects of Model Testing

Design of model tests and interpretation of results are founded on a special application of dimensional analysis known as the Buckingham Pi theorem. According to this theorem, a unique relationship exists among all of the possible non-dimensional groups (π parameters) relevant to the given problem. The variables (Table 2.1) chosen for composing the π parameters relevant to the current problem are shown in Table. 2.2. According to the Buckingham Pi theorem, the number of π terms (n) is given by $n = t - m$, where t = total number of variables relevant to the given problem and m = number of basic dimensions (M, L and T). As seen from Table. 2.1 and 2.2, since the total number of variables (t) relevant to the current problem is 12, the number of independent non-dimensional quantities (π parameters) must be 9. However, one should be aware of the presence of scale effects that are not quite accounted for by the use of non-dimensional parameters. No attempt was made in this study to address this issue.

Table 2.1 Applicable model variables

Variables	Dimensions	Description
y	L	lateral deflection (m)
z	L	depth (m)
d	L	pile width (or diameter) (m)
k	LT^{-1}	Permeability of soil (m/s)
γ	$ML^{-2}T^{-2}$	unit weight of soil (kN/m^3)
ρ	ML^{-2}	mass density (kg/m^3)
P_0	$ML^{-1}T^{-2}$	jet water pressure (kPa)
p	$ML^{-1}T^{-2}$	soil pressure (kN/m^2)
P_L	MLT^{-2}	applied lateral load (kN)
E_PI	$ML^{-1}T^{-2}$	flexural rigidity of pile (kNm^2)
K_P		Coefficient of passive earth pressure
Q	L^3T^{-1}	water flow rate out of the jet (m^3/s)
E_S	$ML^{-1}T^{-2}$	modulus of elasticity of soil (kN/m^2)

Table 2.2 Definition of Pi terms

Pi term	Non-dimensional quantity	
π_1	$\frac{y}{D}$	non-dimensional deflection
π_2	$\frac{z}{D}$	non-dimensional depth
π_3	$\frac{P_0}{k^2\rho}$	non-dimensional jet pressure
π_4	$\frac{P_L}{D^3\gamma}$	non-dimensional lateral load
π_5	$\frac{p}{DE_S}$	non-dimensional soil pressure
π_6	$\frac{E_S}{D\ \gamma}$	non-dimensional soil modulus
π_7	$\frac{E_P I}{D^4 E_S}$	non-dimensional pile rigidity
π_8	K_P	non-dimensional soil strength
π_9	$\frac{Q}{D^2 k}$	non-dimensional flow rate

2.3 Experimental Details of Model Testing

Although the minimum recommended jetting pressure is 344.75 kPa (50 psi, FDOT, 1996), typically used jetting pressures even exceed 1379 kPa (200 psi). However, due to the magnitude of the model testing apparatus, the model jetting pressure had to be limited to a maximum of 758.45 kPa (110 psi), a two-fold reduction of the typical jetting pressure. According to π_3 (Table 2.2), this can be achieved only by using a foundation soil type where the denominator $k^2\gamma$ is changed by a factor of 2.0 within a practical range of unit weights achieved by compaction. In order to "engineer" such a soil, the permeability and density characteristics of different clay-sand mixtures were obtained from a series of falling head permeability and Proctor compaction tests. Fig. 2.1 illustrates the dry unit weight and the corresponding coefficient of permeability, k_{20}, obtained from the falling head permeability test.

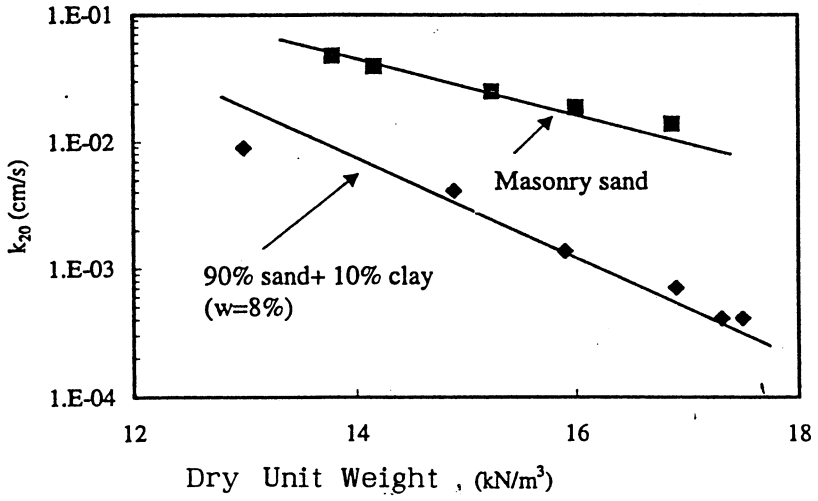

Figure 2.1 Permeability vs dry unit weight

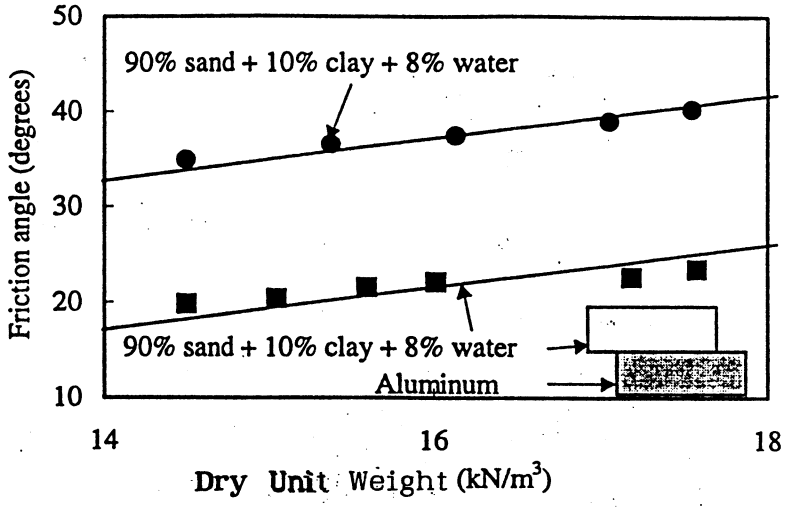

Figure 2.2 Friction angle vs dry unit weight

Based on the above results, the most suitable clay-sand ratio was determined to be 90% fine uniformly graded masonry sand (mean diameter, D_{50}, of 0.25 mm and maximum and minimum unit weight of 13.75 kN/m^3 and 17.45 kN/m^3 respectively) and 10% commercially available kaolinite clay (PI = 22 and LL = 60) at an approximate water content of 8%. Direct shear tests on clay-sand mixture was also conducted to determine the angle of internal friction (φ) (Figure 2.2, at γ_d = 14.8 kN/m^3 $\varphi = 35.32^o$ and γ_d = 16.2 kN/m^3 $\varphi = 37.74^o$). Other relevant properties of the selected soil are shown in Table 2.3.

Table 2.3 Engineering properties of foundation soil

Soil	Percentage finer than number 40 sieve	Percentage finer than number 200 sieve	G_S	Optimum moisture content (OMC %)	γ_d at OMC (kN/m^3)
90 %masonry sand + 10 % kaolinite clay	88.15	10.2	2.68	10.22	17.47

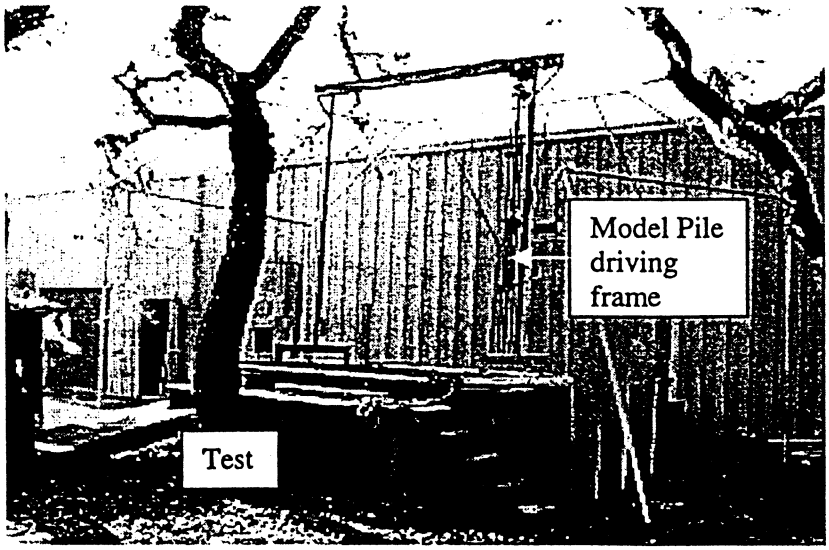

Figure 2.3 Test pit and hammer frame system

Compacted clay-sand mixture weighing 16.2 kN/m^3 was obtained by first placing a known weight of masonry sand in a 2.44 m (8 ft) square and 2.13 m (7 ft) deep test pit (Fig.2.3) at 152.4 mm (6 inch) lifts. Each lift was mixed with 10% kaolinite clay and 8% water by means of a small gasoline operated roto-tiller. After the soil was thoroughly mixed, a WACKER BS-45-Y vibrator rammer was used to compact each lift. To prevent compaction in excess of the required unit weight, prior to the test, the compactor was calibrated for the vibration time and the soil deformation. The final soil unit weight was verified by measuring the weight and volume for each lift deposited in the test pit. The volume of a particular sand-clay layer was estimated knowing the dimensions of the test pit and the average depth of the soil layer after compaction. This process was continued until the test pit was filled up to 1.82 m (6 ft).

A 1.52 m (5 ft) long aluminum tube of cross-section of 50.8 mm × 50.8 mm (2 inch × 2 inch) and 1.6 mm (1/16 inch) thickness was selected as the model pile. Aluminum was chosen in order to obtain a significant lateral deflection and bending strains for a given load, and to avoid local buckling of the cross section during driving. The flexural stiffness of the pile was computed as 9 kN.m^2. Each model aluminum test pile was instrumented with six pairs of electrical resistance strain gauges (at 0.19 m intervals starting from model pile tip) that were mounted on two opposite outside faces. The wire leads from the strain gauges were passed through access holes drilled 25.4 mm (1 inch) above each strain gauge location to the top of the pile. All of the strain gauges were protected by a hard and flat epoxy coating.

The experimental program consisted of testing aluminum model piles installed using impact driving, as well as jetting/driving using 172.38 kPa (25 psi), 344.75 kPa (50 psi), 517.13 kPa (75 psi) and 689.50 kPa (100 psi) jetting pressure. The piles were installed in the foundation soil once it was compacted to a unit weight of 16.2 kN/m^3. After the first stage of testing, the soil fill was reclaimed and recompacted to a unit weight of 14.8 kN/m^3. Further, for each unit weight, the testing program was repeated under a completely submerged condition. The entire testing program and corresponding test model pile abbreviations are shown in Table. 2.4.

Table 2.4 Nomenclature used for piles in the testing program

Unit Weight (kN/m^3)	Condition	Driven Pile	Jetted Pile Identification			
			172.37 kPa	344.75 kPa	517.13 kPa	689.5 kPa
16.2	Unsaturated	UD_1	UJ_{11}	UJ_{12}	UJ_{13}	UJ_{14}
	Saturated	SD_1	SJ_{11}	SJ_{12}	SJ_{12}	SJ_{12}
14.8	Unsaturated	UD_2	UJ_{21}	UJ_{22}	UJ_{23}	UJ_{24}
	Saturated	SD_2	SJ_{21}	SJ_{22}	SJ_{23}	SJ_{24}

A hand operated model laboratory impact hammer with a maximum rated energy of 178 Joules/blow, operating at 3.77 Joules/blow was used to drive the piles. The hammer consisted of steel leads attached to the upper I-beam of the frame via a trolley and pulley system. The frame was supported by four rollers which rested on two parallel steel angles serving as guides on opposite sides of the pit. The rollers and the trolley provided two degrees of freedom such that the hammer and the guide could be taken to any desired location in the pit.

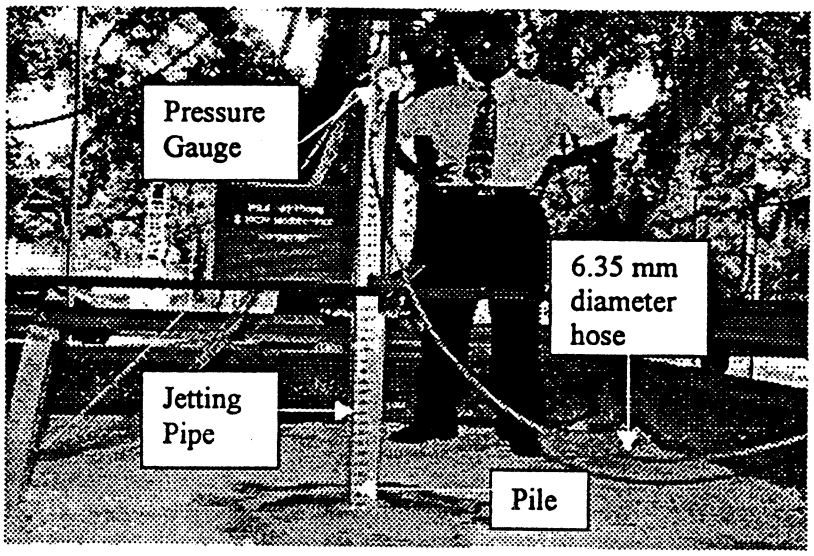

Figure 2.4 Water jet system

The water jet was fabricated out of two stainless steel pipes with an outside and inside diameters of 6.35 mm and 4 mm respectively. Each pipe extended down the length of the pile on opposite sides and was attached to a guide as shown in Fig. 2.4. The entire water jet pipe system was secured to the pile at the top. Water was fed through a 19.05

mm reinforced hose, reduced down to a 6.35 mm hose coupled to stainless steel pipe, passed through a pressure gauge and finally diverted into the jets at the bottom of the pipe. A pressure booster pump was used to pressurize the water from the water reservoir up to the desired jetting pressure. All of the piles were jetted up to a depth of 0.75 m (29.5 inch) and then impact driven another 0.254 m (10 inch) up to the tip elevation.

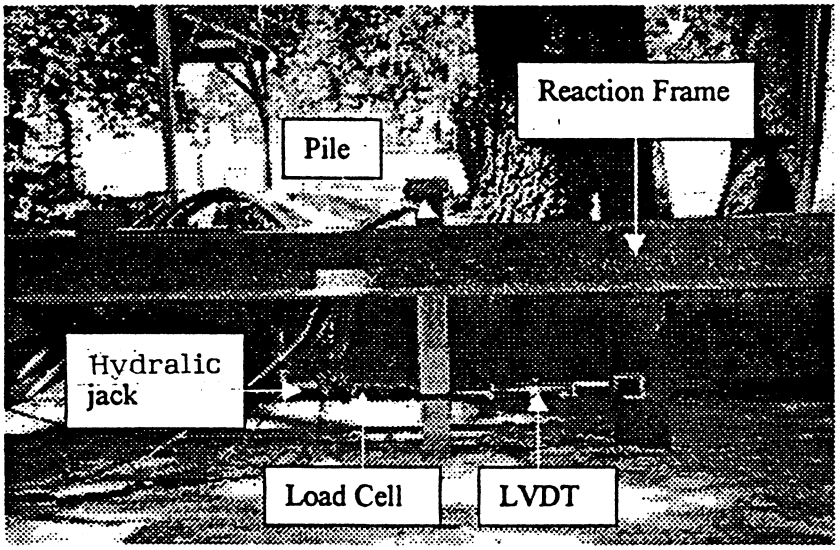

Figure 2.5 Lateral load test setup

Each lateral load tests was conducted within 3 to 4 hours after installation, to allow excess pore water pressure dissipation around the pile. The lateral load was monotonically increased using a hydraulic jack having a stroke of 127 mm (5 inch). The jack was connected to a hand-operated pump equipped with a calibrated pressure gauge. The applied force was monitored by a load transducer, while the lateral displacement at 127 mm (5 inch) above the soil surface was measured with a Linearly Varying

Displacement Transducer (LVDT) as shown in Fig. 2.5. A central data acquisition system monitored all displacement, strain and load data. During each test, the lateral loading was terminated when yielding of the model pile was noticed based on strain-softening in the computer displayed load deflection curve.

Table 2.5 Influence of pile installation procedure on lateral capacities

Test	Lateral-load capacity (kN)	Displacement at failure (mm)	Time required for jetting 0.75m (min)
UD_1	3.89	11.56	N/A
UJ_{11}	3.67	17.66	18.00
UJ_{12}	3.46	23.59	8.50
UJ_{13}	3.23	27.19	3.50
UJ_{14}	3.13	35.63	1.88
SD_1	3.40	26.70	N/A
SJ_{11}	3.31	28.07	10.40
SJ_{12}	3.17	29.97	6.63
SJ_{13}	3.13	30.48	4.20
SJ_{14}	3.05	32.00	1.12
UD_2	3.17	25.66	N/A
UJ_{21}	3.12	31.65	6.19
UJ_{22}	3.10	33.53	3.80
UJ_{23}	3.03	37.34	2.90
UJ_{24}	2.82	40.13	1.68
SD_2	3.23	31.06	N/A
SJ_{21}	3.09	44.48	3.23
SJ_{22}	2.90	48.46	2.73
SJ_{23}	2.56	50.29	1.91
SJ_{24}	2.50	53.44	1.06

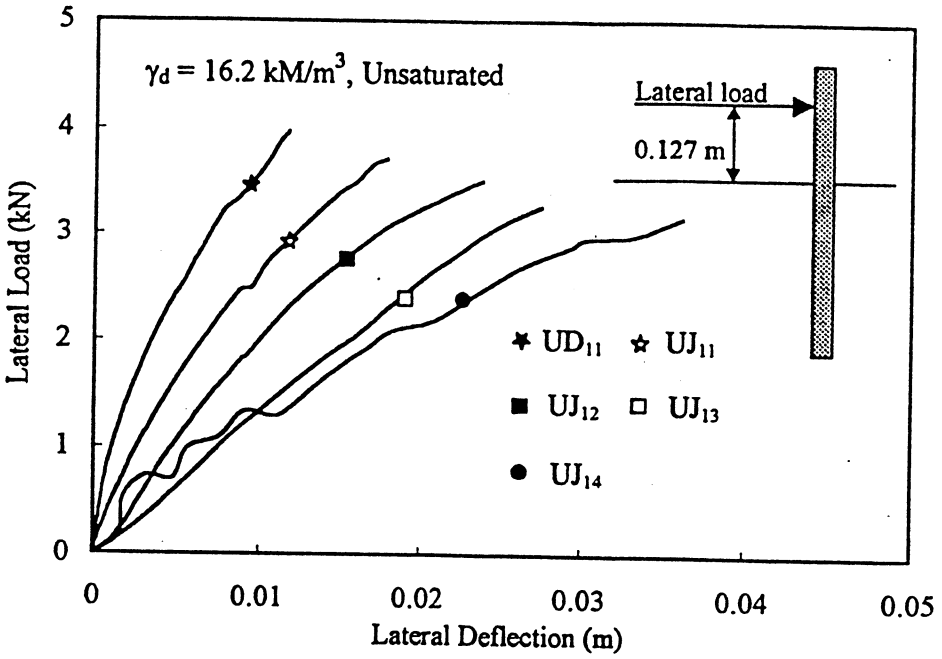

Figure 2.6 Lateral Load vs lateral displacement at 0.127 m (5 inch) from ground surface

Lateral load deformation curves for one of the load tests is given in Fig. 2.6. It can be seen from Fig. 2.6 and Table 2.5 that the response is nonlinear at all load levels. As expected, the driven pile shows stiffer behavior than the other piles. Comparison of the curves for jetted piles shows that an increase in the jetting pressure or the flow rate decreases the lateral load capacity while increasing the lateral displacement at failure. This observed reduction in the lateral load capacity may be due to the larger extent of the influence zone formed by a higher jetting pressure.

2.3.1 Evaluation of results

The condition of a laterally loaded pile can be idealized as that of an infinitely long cylinder laterally deforming in an infinite elastic medium or as a plane strain

problem of a rigid cylinder laterally deforming in an infinite elastic medium (Pyke at al, 1984). Broms (1964) showed that a laterally loaded pile behaves as an infinitely stiff member when the dimensional length factor ηL ($\eta = (K_h/EI)^{1/5}$) is less than 2 where K_h is the coefficient of horizontal subgrade reaction. Further, it was shown to behave as an infinitely long flexible member when $\eta L \geq 4$ as shown in Fig. 2.7.

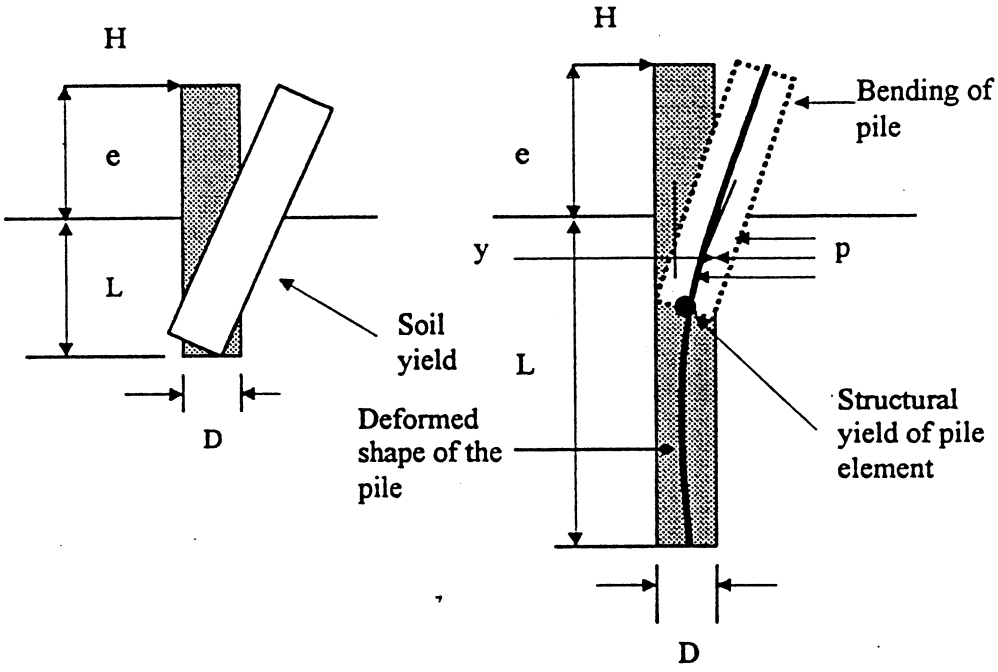

(a) Rigid (short) pile (b) Flexible (long) pile

Figure 2.7 Relative rigid vs flexible pile behavior

In this testing program, for the combination of (1) E_PI (model pile flexural stiffness) = 9 kNm^2, (2) L_P (embedded model pile length) = 1.00 m, and (3) $108 < K_h < 600$ MN/m^3 (assumed average value), ηL ranges from $6 < \eta L < 8$. Hence, the tested model pile can be classified as a flexible infinitely long member. Failure generally occurs when the maximum stresses due to bending exceed the yield resistance of the pile.

Strain gauge readings obtained along the length of the pile are used to develop the lateral load transfer curves (p-y curves) at a finite number of points along the pile. The values of p (horizontal distributed load intensity) and y (deflection) at any pile location at a given lateral loading stage can be determined from the simple beam theory,

$$\frac{d^2y}{dz^2} = \frac{\varepsilon}{h} \tag{2.1}$$

where

ε = bending strain

y = lateral deflection

z = vertical coordinate along the pile

h = the distance from the neutral axis of the pile cross-section to the strain gauge location

Hence the lateral deflection (y) and distributed soil load on the pile (p) are given by

$$y = \frac{1}{h}\iint \varepsilon dz dz \tag{2.2}$$

$$p = E_p I \frac{d^4y}{dz^4} = \frac{E_p I}{h}\frac{d^2\varepsilon}{dz^2} \tag{2.3}$$

Thus, it can be seen that both p and y values can be found from a mathematically defined ε curve based on measured flexural strains. This is usually achieved either by fitting a cubic spline function between successive strain data points (Finn et al, 1983, Scott, 1980, Abendroth et al, 1990, Georgiadis et al, 1991, Li Yan at al, 1992) or fitting a higher order polynomial to all of the strain data points (Ting 1986, 1987). In this study, the latter procedure was used.

The fitting procedure is illustrated as follows with the distance z measured from the pile tip which is located 1.00 m (39.5 inch) below the soil surface. In order to closely trace all of the strain data, the following polynomial with five coefficients was considered

$$y = a_1 z^6 + a_2 z^7 + a_3 z^8 + a_4 z^9 + a_5 z^{10} \tag{2.4}$$

where a_i, i = 1 to 5, are constants.

It can be seen that the terms up to z^5 have been discarded from Eqn. (2.4) since the pile deflection and all of its derivatives up to the fifth derivative were considered as zero at the pile tip (z = 0) (Ting,1986, 1987). This is because the deflection, slope, moment, shear and pressure distribution due to the applied lateral load are negligible at the pile tip. From Eqn. (2.1) the strain at any location z within the embedded part of the pile can be expressed by

$$\varepsilon = h\frac{d^2y}{dz^2} = h(30a_1 z^4 + 42a_2 z^5 + 56a_3 z^6 + 72a_4 z^7 + 90a_5 z^8) \tag{2.5}$$

Then four pairs of strain gauge readings and the known soil pressure (p = 0) at the soil surface (z = 1.00m) were used to determine the a_i.

Furthermore, a third degree polynomial function was employed for approximating the deflection (y) of the free portion of the pile (above the ground level). This is because the fourth derivative of this polynomial (p in Eqn. 2.3) automatically vanishes, thus satisfying the p = 0 condition all over the free portion. Consequently, the deflection above the soil surface can be given by

$$y = b_0 + b_1(z - z_0) + b_2(z - z_0)^2 + b_3(z - z_0)^3 \tag{2.6}$$

where z_0 = 1.00 m. Three of the above constants (b_i, i = 0 to 3) were determined by matching the deflection, slope and moment of the free pile portion with the corresponding

values of the embedded portion determined by Eqn. (2.4), at the soil surface ($z = z_0$). The fourth b_i constant was determined by setting the moment at the lateral loading level equal to zero.

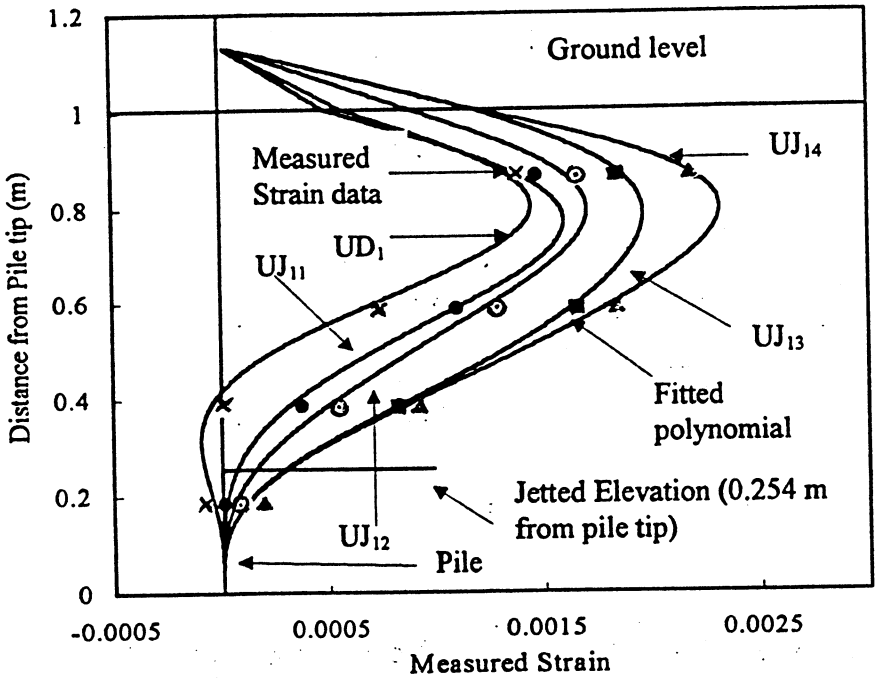

Figure 2.8 Polynomial fitted measured strain data

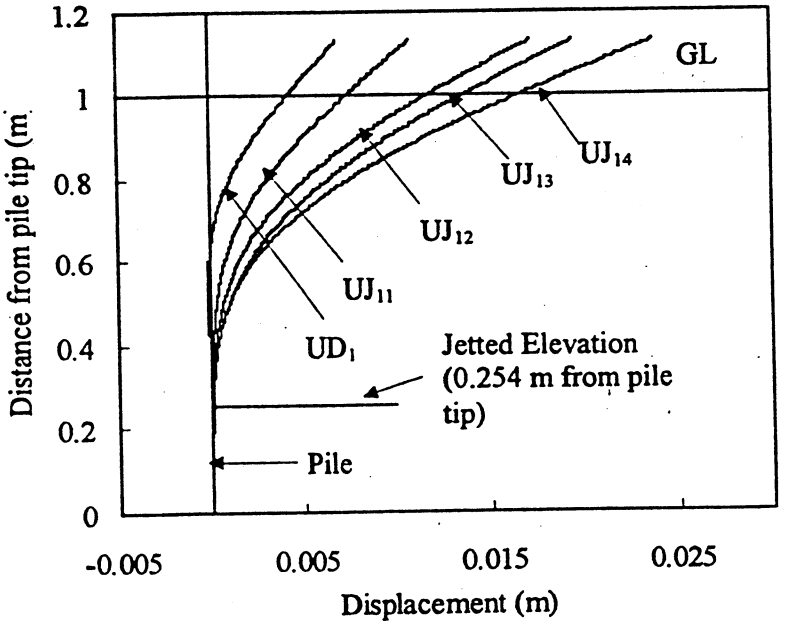

Figure 2.9 Calculated pile displacement

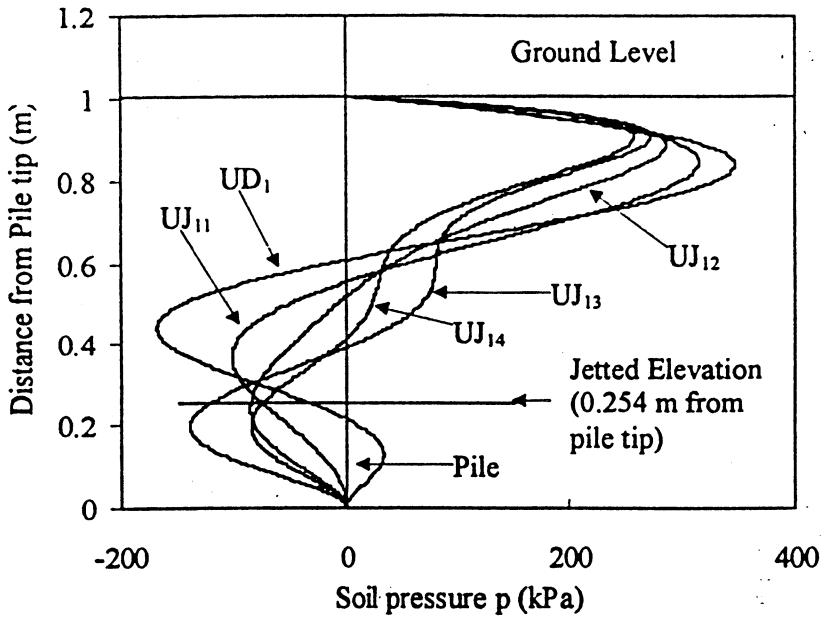

Figure 2.10 Calculated soil pressure

The distributions of strains, deflections and soil pressure computed using the above methodology are illustrated in Figs. 2.8, 2.9 and 2.10 respectively, at an arbitrarily selected load of 2.5 kN during the jetted tests on the unsaturated soil bed of unit weight 16.2 kN/m^3. It is seen that close agreement exists between the fitted curve and the actual measurement of strain (Fig. 2.8). Further, it can be seen that the pile jetted with 689.50 kPa pressure shows the largest strain, deflection and smallest soil pressure. These excessive deformations and the low lateral pressure appear to be associated with the degradation of soil around the pile due to the increased jetting effect, suggesting (1) a reduction in shear modulus of soil, and (2) permanent plastic deformation of the soil. Moreover, even though all of the piles were impact driven for the last 0.25 m (10 in) regardless of their method of installation, their behavior below this level was different,

suggesting the possibility of the effects of the method of installation persisting in the impact driven last portion.

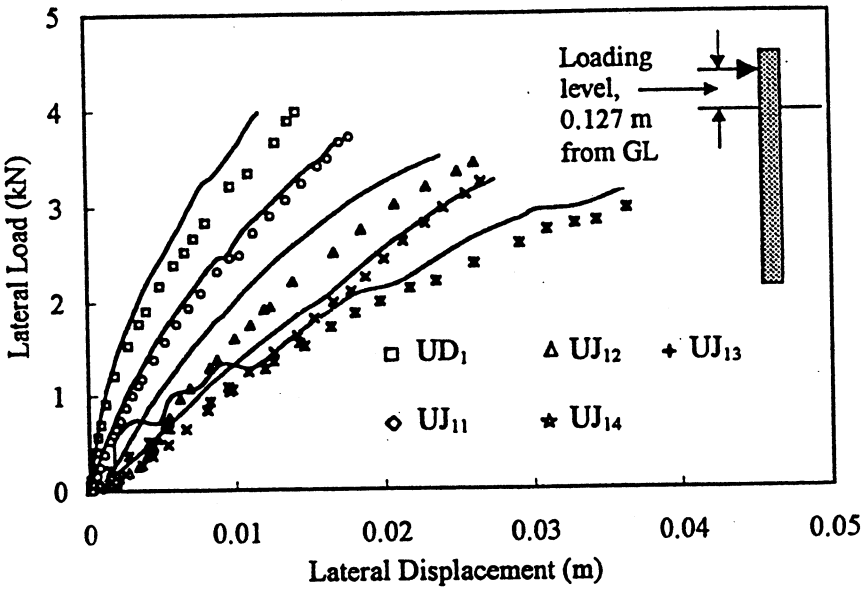

Figure 2.11 Measured and calculated lateral load displacement

Fig. 2.11 shows the analytical predictions of lateral load behavior of the piles at the loading level plotted along with the measured lateral load and displacement at this level, throughout each test. The agreement seen in Fig. 2.11 also indicates that the selected analytical model satisfactorily predicts the pile behavior under lateral loading. Similar results were obtained for all four testing conditions illustrated in Table.2.4.

Typical soil-pile load transfer characteristics at different relative depths are illustrated in Figs.2.12(a) to 2.12(d) for each pile in terms of p-y curves. The complete lateral resistance and displacement behavior were established up to a relative depth of 4D, since below 4D, only an insignificant initial portion of the p-y response was developed at the pile failure stage.

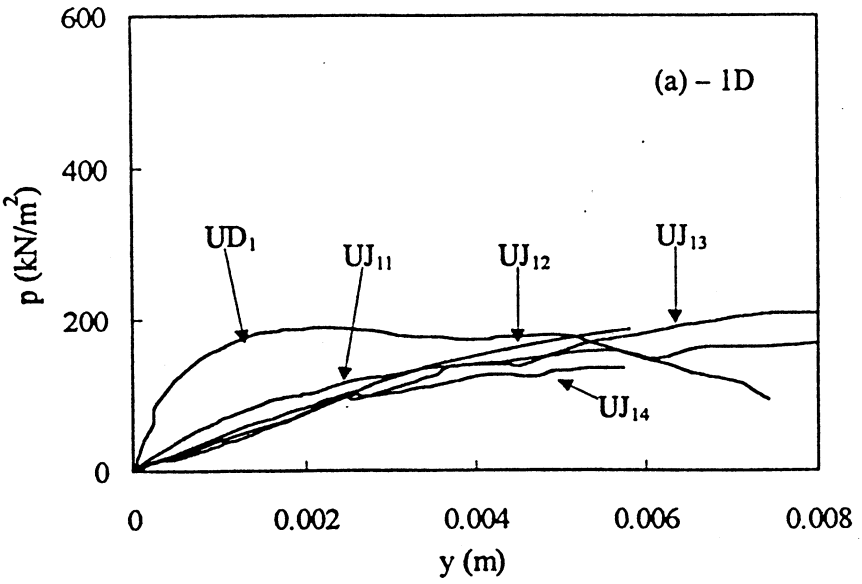

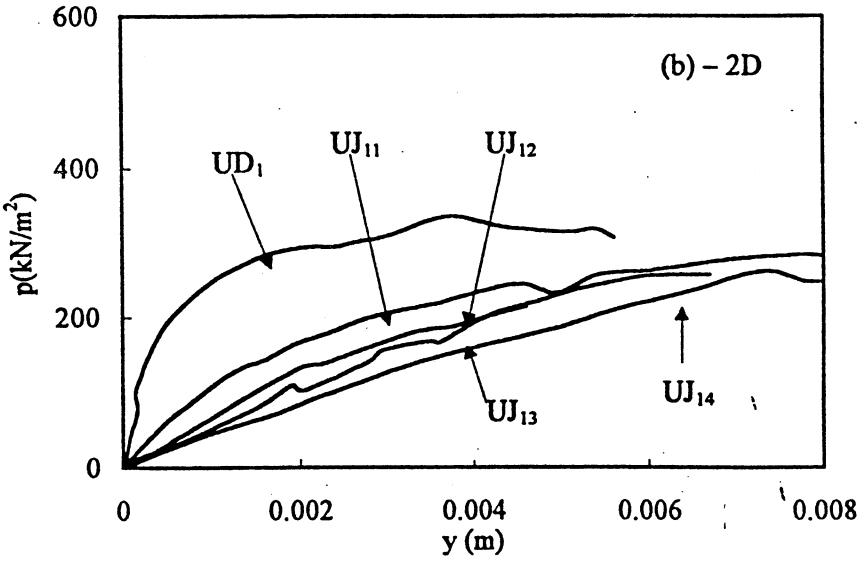

Figure 2.12 p – y curves

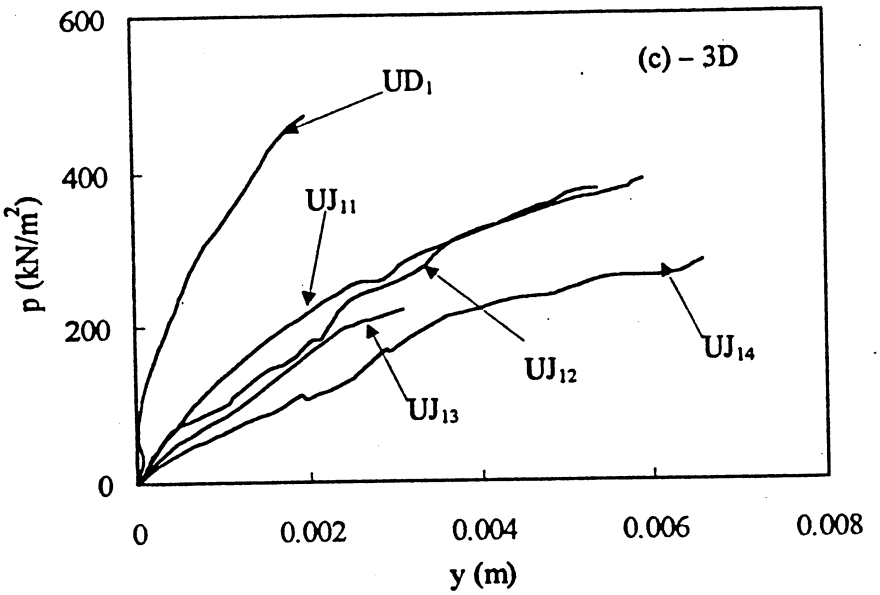

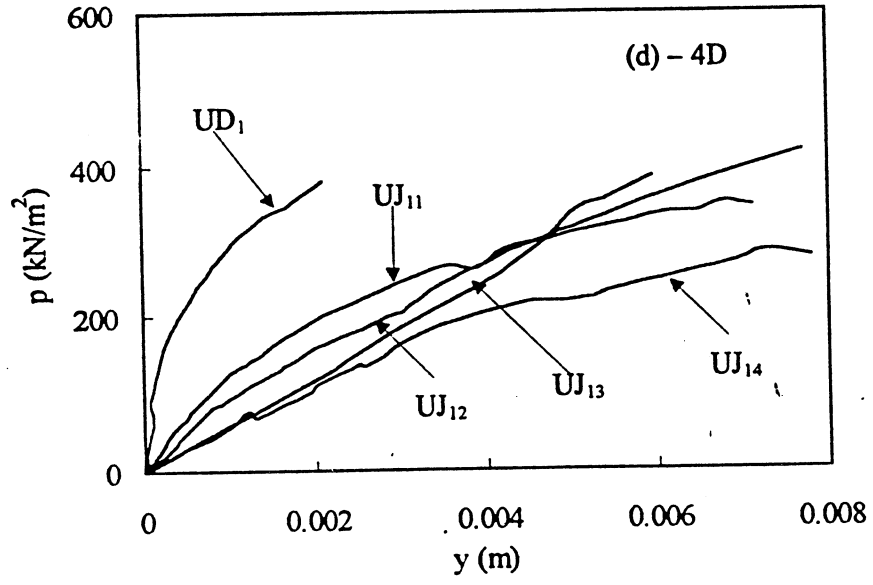

Figure 2.12 (Continued)

It can be seen that p-y curves also exhibit highly nonlinear and relatively softer behavior at shallower depths (1D and 2D) and relatively stiffer behavior at 3D and 4D depths. As expected, at all of the depths, the driven pile shows stronger behavior than jetted piles. This may justify the commonplace assumption that the disturbance caused by jetting *does* effect the pile behavior and therefore the soil strength-deformation characteristics. This deviation is probably due to the following reasons; (1) jetting produces an uneven disturbance throughout the depth resulting from the excessive washing out of material surrounding the pile in leading to highly distorted, remolded cavity walls around the pile, (2) uneven changes in water content (and thus strength) of the soil around the pile resulting from the excess pore water pressure generated during jetting, (3) jetting leads to the destructuring and loss of frontal resistance of soil around the pile through lateral stress and pore pressure build up.

The p-y curves can be normalized using a soil parameter which depicts the stress level. A suitable normalized parameter for this purpose is $\pi_5 = p/E_sD$ (Table 2.2) since E_{max} (elastic modulus at very low strains) used to compute π_5 (Li Yan at al, 1992) shows a strong mean normal stress dependence. In this research, E_{max} was determined from the measured coefficient of horizontal subgrade reaction, K_{max}, using the following expressions (Glick, 1948, Bowles 1996):

$$K'_s = DK_{max} \tag{2.7}$$

$$K'_s = \frac{22.4E_S(1-\nu)}{(1+\nu)(3-4\nu)\left[2\ln(2L_p/D)-0.433\right]} \tag{2.8}$$

where K'_s and E_s has same units (kPa) and

K'_s = horizontal subgrade modulus

L_p = pile length (1.00 m)

D = pile width (0.051 m)

ν = Poisson's ratio

A typical ν value of 0.3 was used for the sand/clay mixture. K_{max} at each depth was obtained from the initial stiffness of the experimentally determined p-y curves (Figs. 2.12(a) – 2.12(d)) for the driven pile assuming that the soil around the driven pile had the minimum disturbance.

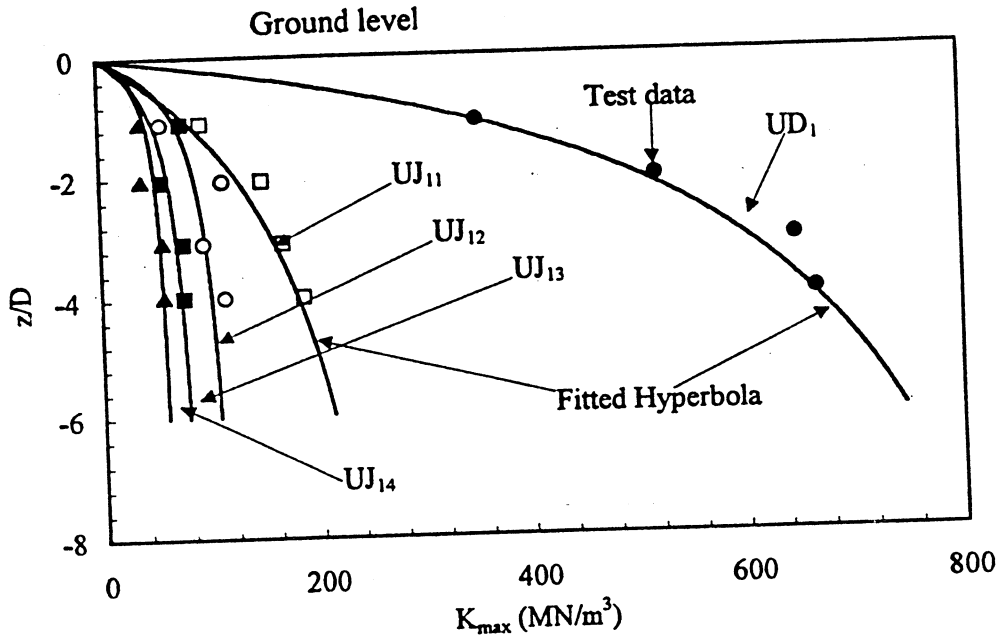

Figure 2.13 Variation of K_{max} vs z/D

Fig. 2.13 compares the K_{max} for different piles, and the positive effect of the confining stress on K_{max} can be clearly seen as the latter increases with increasing overburden. From Fig. 2.13 the effect of increasing the jetting pressure on K_{max} also is clearly evident. Similarly, ultimate soil pressures (p_u) are obtained from p-y curves at

each depth by fitting the experimentally obtained data points with a hyperbolic function of the form p = y/(a+by) (Kondner, 1963, Georgiadis et al, 1991). Then, p_u value for each fitted curve is obtained by the curve parameter, 1/b, since p_u = 1/b when $y \rightarrow \infty$.

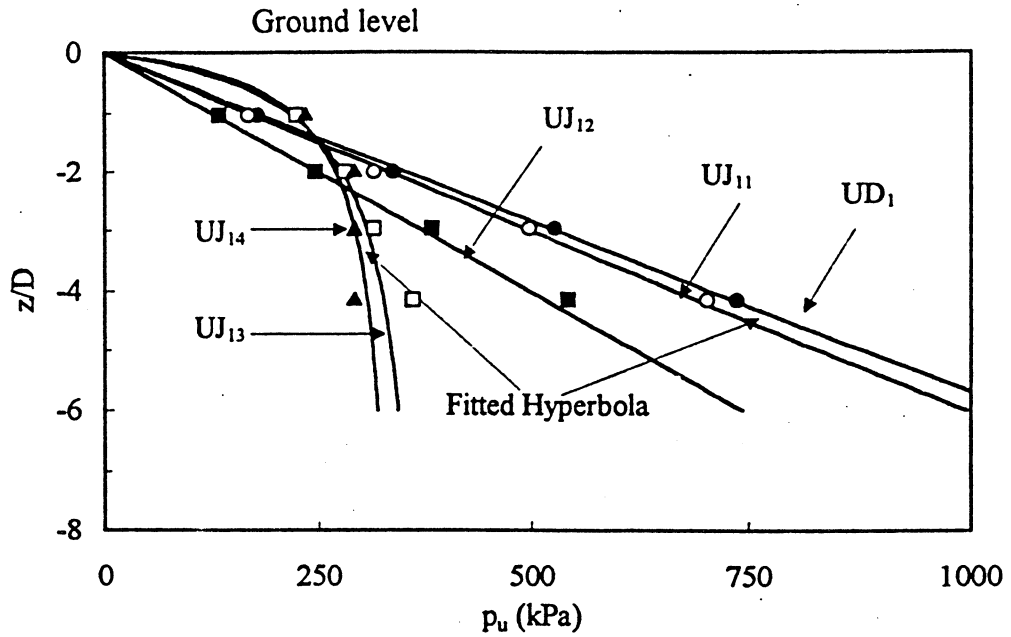

Figure 2.14 Variation of p_u vs z/D

p_u value at each depth are shown in Fig. 2.14. Table 2.6(a)-(d) shows the K-ratio and p_u-ratio (K_{jet}/K_{driven} and $p_{u,jet}/p_{u,driven}$ respectively) at each depth for all of the experimental conditions.

Table 2.6 (a). Comparison of curve fitted K_{max} and p_u values (16.2 kN/m^3 Unsaturated)

Depth	UD_1 K_{max} (kN/m^3)	p_u (kPa)	UJ_{11}/UD_1		UJ_{12}/UD_1		UJ_{13}/UD_1		UJ_{14}/UD_1	
1D	329815	176	0.23	0.94	0.21	0.71	0.14	1.22	0.13	1.25
2D	496032	352	0.25	0.94	0.18	0.71	0.13	0.79	0.11	0.77
3D	596484	528	0.26	0.94	0.17	0.71	0.12	0.58	0.10	0.56
4D	663130	704	0.27	0.94	0.15	0.71	0.11	0.47	0.09	0.44
5D	711035	880	0.28	0.94	0.15	0.71	0.11	0.39	0.09	0.36

Table 2.6 (b). Comparison of curve fitted K_{max} and p_u values (16.2 kN/m^3 Saturated)

Depth	SD_1 K_{max} (kN/m^3)	p_u (kPa)	SJ_{11}/SD_1		SJ_{12}/SD_1		SJ_{13}/SD_1		SJ_{14}/SD_1	
1D	55463	280	0.75	0.93	0.72	2.04	0.67	2.07	0.56	1.86
2D	76746	435	0.84	0.94	0.81	1.46	0.78	1.43	0.57	1.40
3D	88002	531	0.90	0.95	0.87	1.24	0.81	1.35	0.57	1.24
4D	94967	600	0.94	0.96	0.91	1.12	0.83	1.23	0.57	1.13
5D	99701	647	0.97	0.96	0.94	1.05	0.85	1.16	0.57	1.07

Table 2.6 (c). Comparison of curve fitted K_{max} and p_u values (14.8 kN/m^3 Unsaturated)

Depth	UD_2 K_{max} (kN/m^3)	p_u (kPa)	UJ_{21}/UD_2		UJ_{22}/UD_2		UJ_{23}/UD_2		UJ_{24}/UD_2	
1D	58153	144	0.37	0.61	0.27	0.86	0.39	1.35	0.37	0.91
2D	113884	292	0.37	0.61	0.27	0.58	0.28	0.86	0.26	0.72
3D	167339	440	0.37	0.60	0.27	0.43	0.22	0.64	0.21	0.60
4D	218656	628	0.37	0.56	0.27	0.34	0.19	0.47	0.17	0.48
5D	267960	740	0.37	0.59	0.27	0.30	0.16	0.42	0.15	0.44

Table 2.6 (d). Comparison of curve fitted K_{max} and p_u values (14.8 kN/m^3 Saturated)

Depth	SD_2 K_{max} (kN/m^3)	p_u (kPa)	SJ_{21}/SD_2		SJ_{22}/SD_2		SJ_{23}/SD_2		SJ_{24}/SD_2	
1D	21218	195	0.83	0.60	0.82	0.54	0.75	0.52	0.47	0.43
2D	38366	304	0.69	0.64	0.67	0.53	0.62	0.51	0.46	0.35
3D	52512	380	0.61	0.66	0.59	0.51	0.55	0.48	0.46	0.31
4D	64381	421	0.55	0.69	0.53	0.51	0.50	0.48	0.45	0.29
5D	74482	456	0.51	0.71	0.49	0.51	0.46	0.47	0.44	0.28

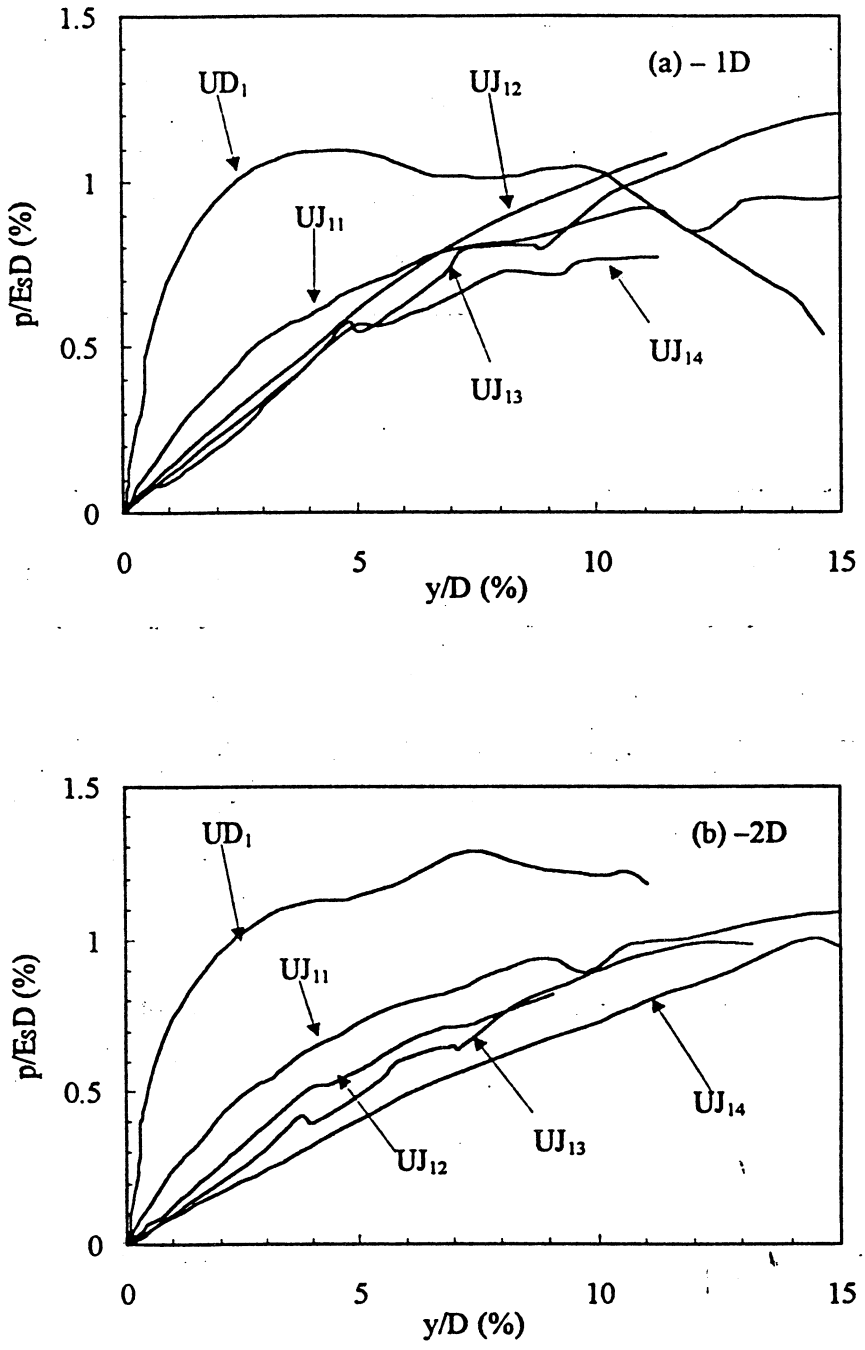

Figure 2.15 Normalized p – y curves

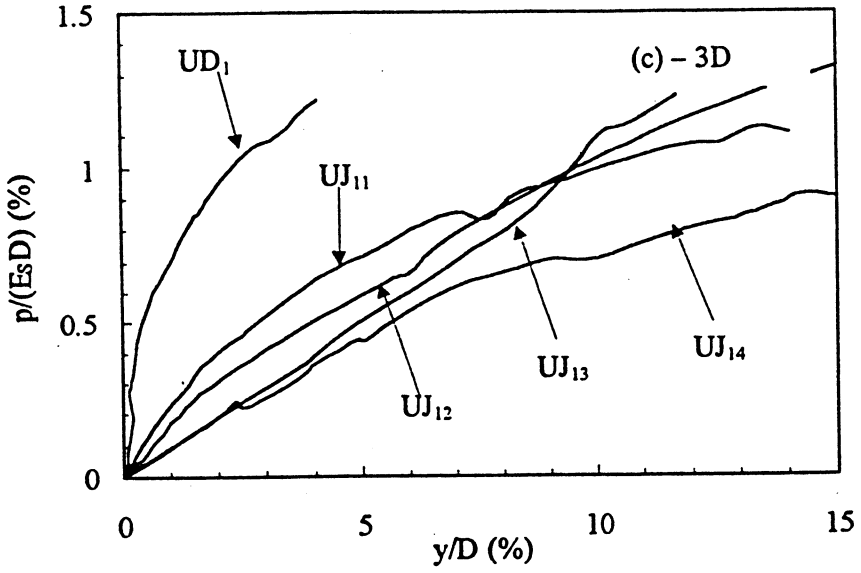

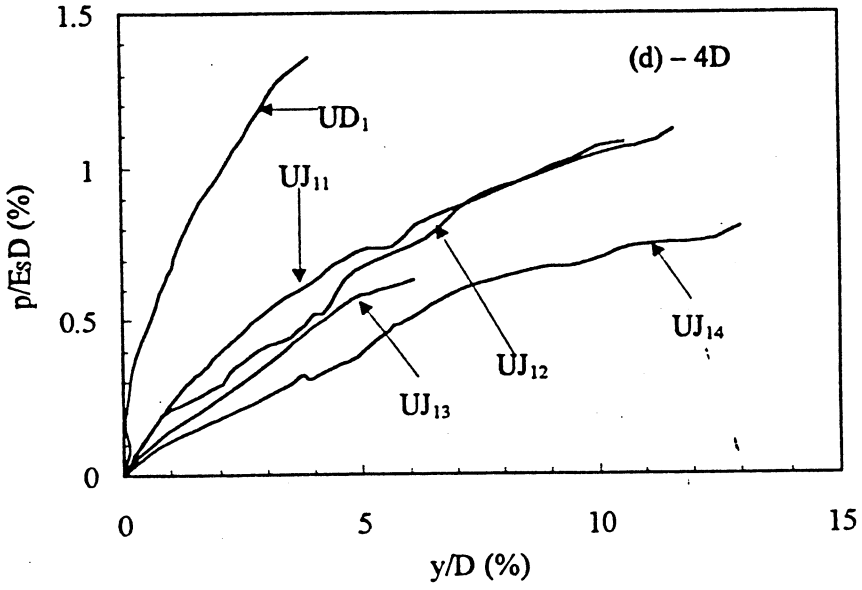

Figure 2.15 (Continued)

Figs. 2.15 (a) – (d) illustrate the normalized p-y curves. Hence one can use these normalized curves to generate the lateral load characteristics (p-y curves) for any other desirable condition knowing the soil parameters and the pile size. Finally, K-ratios (K_{jet}/K_{driven}) and p_U-rato ($p_{U,jet}/p_{U,driven}$) obtained from the entire testing program are plotted against the non-dimensional jetting pressure ($\pi_3 = P_0/k^2\rho$) and shown in Figs. 2.16 and 2.17.

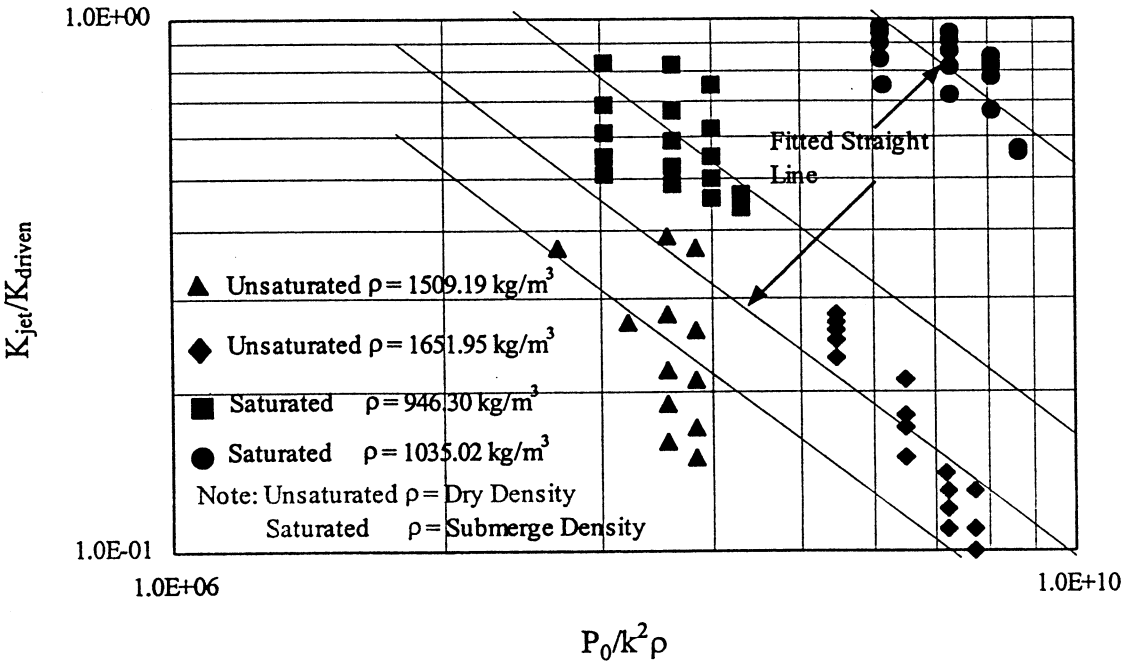

Figure 2.16 Non dimensional K-ratio vs jetting pressure

The K-ratio and p_U-ratio can be related to non-dimensional jetting pressure by following equation

$$\frac{K_{jet}}{K_{driven}} = \alpha_1 \left(\frac{P_0}{k^2 \rho} \right)^{\beta_1} \tag{2.9}$$

$$\frac{p_{U,jet}}{p_{U,driven}} = \alpha_2 \left(\frac{P_0}{k^2 \rho} \right)^{\beta_2} \tag{2.10}$$

where, α_1, α_2, β_1 and β_2 are soil type dependent constants which be determined by the respective intercepts and slopes Eqns. (2.9) and (2.10) produce on a log-log scale.

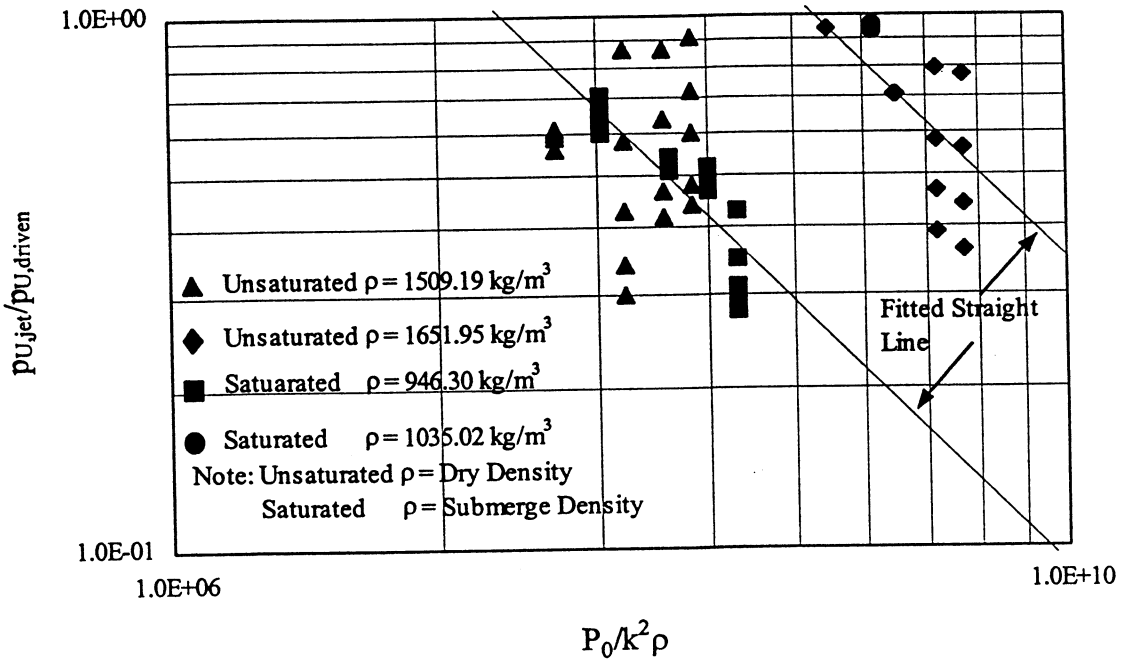

Figure 2.17 Non dimensional p_U vs jetting pressure

The fitted values are shown in Tables 2.7(a) – (b).

Table 2.7 (a) Constant for Eqn. (2.9)

Constants	ρ (kg/m³)		ρ (kg/m³)	
	1651.95	1035.02	1509.19	946.30
α_1	165.44	904.65	111.90	280.38
β_1	-0.323	-0.323	-0.323	-0.323

Table 2.7 (b) Constants for Eqn. (2.10)

Constants	ρ (kg/m^3)		ρ (kg/m^3)	
	1651.95	1035.02	1509.19	946.30
α_2	4699.85	4699.85	1246.39	1246.39
β_2	-0.413	-0.413	-0.413	-0.413

The values for β_1 and β_2 seem to be independent of the foundation medium density and the groundwater table level. On the other hand the values of α_1 and α_2 seems to increase with the foundation medium density. Hence one can assume the variation of α_1 and α_2 to be linear proportional to the foundation medium density.

2.3.2 Numerical Example

If a field p-y curve of a *driven pile* in a soil type similar to the tested soil (clayey sand) based on either (1) experimental data, (2) Reese et. Al. (1974) method (Fig. 2.18(a)), or (3) Murchison and O'Niell's (1984) method (Fig. 2.18(b)) is available, and, if one neglects the possible errors due to scale then one can generate p-y characteristics for a pile to be *jetted-driven* in the same soil type.

In order to illustrate this, assume that a p-y curve based on method by Murchison and O'Niell's (1984) is available for a *driven* pile at a clayey sand site (with $k_{20} = 1.592\times10^{-3}$ cm/s and $\rho = 1607.08$ kg/m^3 or $\gamma = 15.76$ kN/m^3 above the groundwater table) and that relevant parameters at 3D depths are $A_d = 1$, $p_{U,d} = 900.00$ kPa and $K_{max,d} = 30000.00$ kN/m^3 (Fig. 2.18 (b)). The subscript "d" indicates a driven pile. Using these values, the corresponding p-y curve can be plotted in Fig. 2.19.

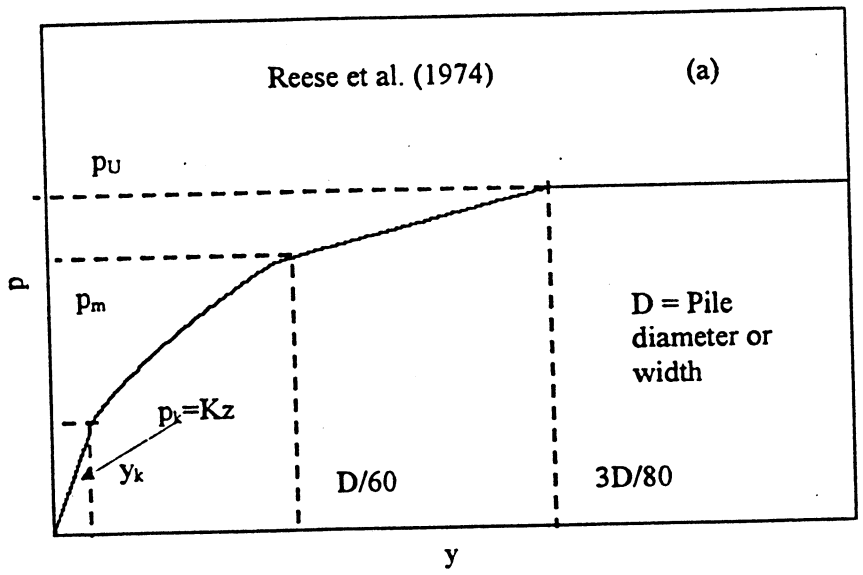

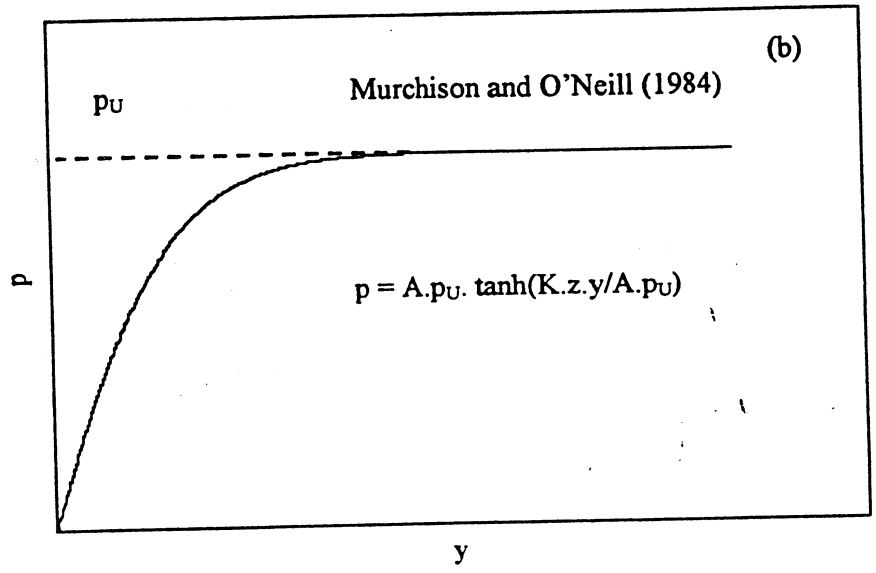

Figure 2.18 Schematic presentation of load transfer relationship

Also assume that one is interested in synthesizing a p-y curve at 3D for a field jetting pressure of 861.88 kPa (125 psi). The equivalent non-dimensional jetting pressure corresponding to the above soil properties must be determined by the π parameter, $\pi_3 = (P_0/k^2\rho)$ (Table 2.2). the constants α_1, α_2, β_1 and β_2 can be obtained by linear interpolation based on the values given in Tables 2.7(a) and (b). Table 2.8 shows the interpolated values at a 1607.08 kg/m^3 density. It has been assumed that the range of values shown in Table 2.7 are generally valid for any combination of density and permeability for soils similar to the tested one.

Table 2.8 Interpolated constants for use in Eqns. (2.9) and (2.10)

ρ (kg/m^3)	$P_0/k^2\rho$	α_1	α_2	β_1	β_2
1607.08	2.12×10^9	146.36	3093.64	-0.323	-0.413

Using Eqns. (2.9), (2.10) and Table 2.8, the K-ratio and p_U-ratio can be determined as 0.14 and 0.44 respectively. Thus, the corresponding p-y parameter at 3D depth, for the pile to be jetted at 861.88 kPa are, $A_j = 1.0$, $K_{max,j} = 4200.00$ kN/m^3 and $p_{U,j} = 396.00$ kPa. The corresponding p-y curve is also plotted in Fig. 2.19.

This example shows how one can use Eqns. (2.9) and (2.10) to easily generate the p-y curve for a pile to be jetted at any desired pressure in the field. It must be noted that the same procedure can be extended to obtain p-y curves for any desired *jetting pressure,* based on p-y curves for *driven* piles available also in terms of Reese et. Al. (1974) method or experimental data, by employing comparisons found in Table 2.7 and Eqns. (2.9) and (2.10).

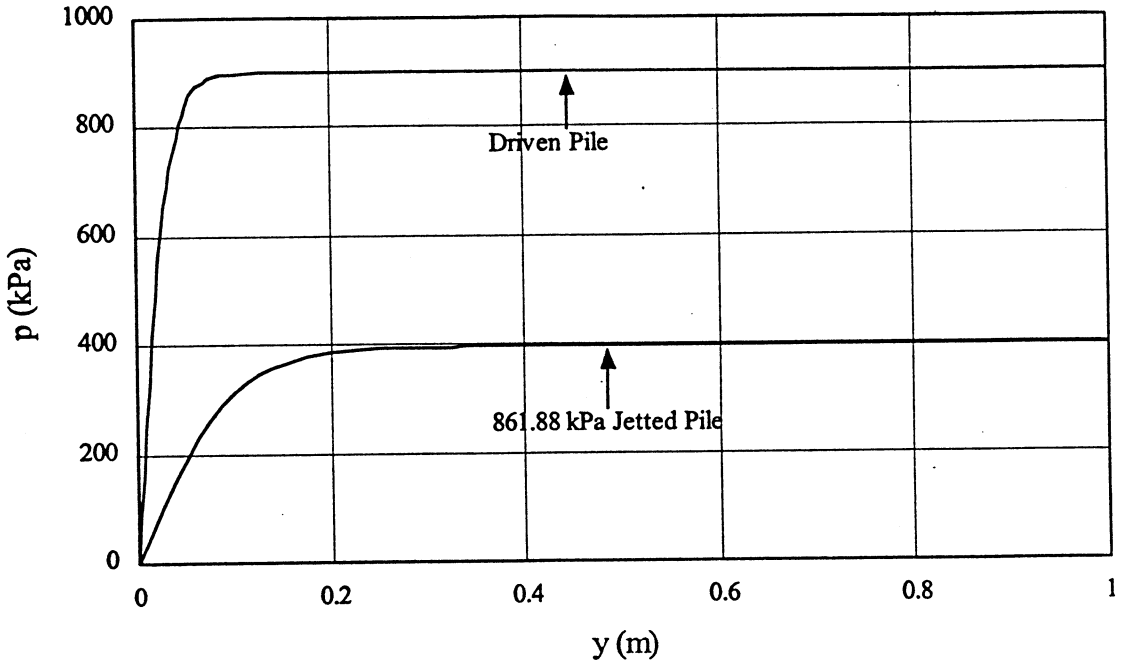

Figure 2.19 Predicted p-y curve

2.4 Conclusions

The lateral monotonically increasing loading behavior of vertical, free-headed piles installed by jetting was presented, based on a model study. The study was specifically focused on the soil-pile load transfer behavior in terms p-y curves under different installation procedures (driving, jetting). Based on this study, the following conclusions can be drawn;

(1) Piles driven in a clayey sand clearly exhibited a higher lateral load capacity than the jetted ones. In addition, jetting significantly increase the lateral deflection at failure.

(2) An increase in the jetting pressure or the quantity of flow increase the lateral deflection at failure noticeably reduce the maximum lateral load. This is due to the

extensive wetting or ground disturbance which causes softening and remolding leading to a reduction in soil resistance.

(3) The experimental p-y relationships are nonlinear, being softer at shallow depths and stiffer at higher depths. The stiffness of p-y curves of jetted piles were considerably lower than those of the corresponding driven piles. This can be expected as a result of the increase in the moisture content and the accompanied increase in pore water pressure and soil disturbance surrounding the jetted pile.

(4) The experimental comparisons in Tables 2.7 as well as Eqns. (2.9) and (2.10) can be used as approximate guidelines to develop potential p-y curves for *jetted* piles when the p-y curves for a *driven* pile are available for the same soil in terms of experimental data or commonplace empirical methods.

CHAPTER 3

LATERAL LOAD BEHAVIOR OF PREFORMED PILES

3.1 Introduction

Preforming, in conjunction with pile driving, can be used to install piles through upper layers of hard soil and penetrate through subsurface obstructions. It can be also employed to eliminate or reduce the possibility of ground heave or to reduce ground pressures resulting from soil displacement during driving. In addition, preforming can be used to reduce the amount of driving required to seat the pile properly in the bearing material and possible vibration and noise which may be associated with pile driving. However, once the required pile tip elevations are approached, the preformed piles are driven until the required bearing capacities are obtained.

Preforming is a much more controllable driving aid than jetting. It is also less detrimental to adjacent piles or structures or on the frictional capacity of the pile. Hence preforming can be more effective than jetting in most types of soils. However, due to removal of the in-situ confinement during preforming, it is suspected that the lateral support of preformed/driven piles is reduced compared to completely driven piles. The knowledge of the extent of this lateral support reduction is of importance to the pile design engineers.

In order to achieve this objective, a comprehensive research program was initiated and the goal of the first phase of the project was to experimentally investigate lateral load behavior of preformed piles using a model study. This goal was achieved by (1) determining the normalized experimental load transfer curves (p-y curves) along the pile depth and comparing the p-y curves of driven piles to those of preformed piles, (2) exploring the effect of preformed hole diameter, soil unit weight and saturated conditions on the p-y characteristics. During the second phase of the investigation, a computational procedure based on the finite element method was developed to analytically model the lateral load behavior of preformed piles. Finally, the model test results were compared to the analytical predictions in order to calibrate the analytical model for more comprehensive predictions.

3.2 Experimental Details of Model Preformed Pile Testing

As mentioned in Chapter 2, twelve preformed pile driving and static load tests were preformed in order to assess the lateral load behavior. The entire preformed pile testing program and corresponding test model pile abbreviations are shown in Table 3.1. As in the case of jetting, foundation soil was prepared under two different unit weights (16.2 kN/m^3 and 14.8 kN/m^3) under both unsaturated and saturated conditions.

The experimental setup and testing procedure are similar to that described in detail in Chapter 2. However, for completeness, a brief description of the preformed pile installation procedure is provided below.

Table. 3.1 Nomenclature used for preformed piles in the testing program

Unit Weight (kN/m^3)	Condition	Driven Pile	Diameter of Preformed Pile (mm)		
			38.1 ■	50.8 ■	63.5 ■
16.2	Unsaturated	UD_1	UP_{11}	UP_{12}	UP_{13}
	Saturated	SD_1	SP_{11}	SP_{12}	SP_{12}
14.8	Unsaturated	UD_2	UP_{21}	UP_{22}	UP_{23}
	Saturated	SD_2	SP_{21}	SP_{22}	SP_{23}

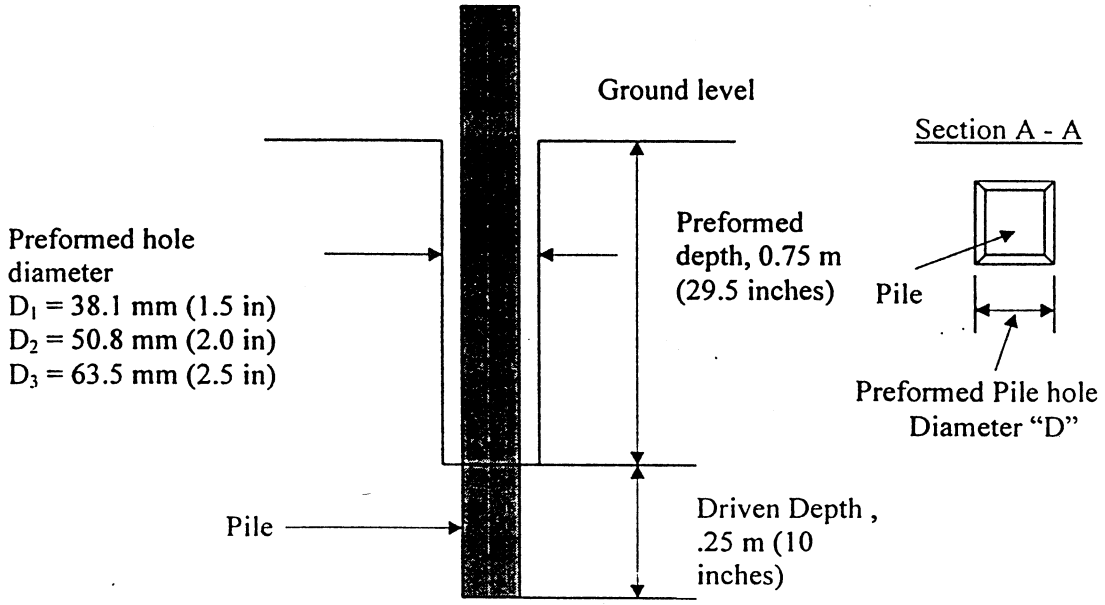

Figure 3.1 Schematic diagram of preformed pile

In practice, the preformed hole is augered, and the sides of the hole are supported either with a slurry or a casing. In the case of cohesive soils, the holes are self supported. In this study, the casing was eliminated since there were no sign of caving or collapse observed during augering within a depth of 0.75 m. Preformed piles were installed by augering

38.1 mm (1.5 inches), 50.8 mm (2.0 inches) and 63.5 mm (2.5 inches) square and 0.75 m (29.5 inches) deep as shown in Fig. 3.1. A specially designed auger was used for preforming as shown in Fig. 3.2. Figs. 3.3 (a) and (b) show the completed auger hole and pile placement in the preformed hole.

Figure 3.2 Auger used in this study

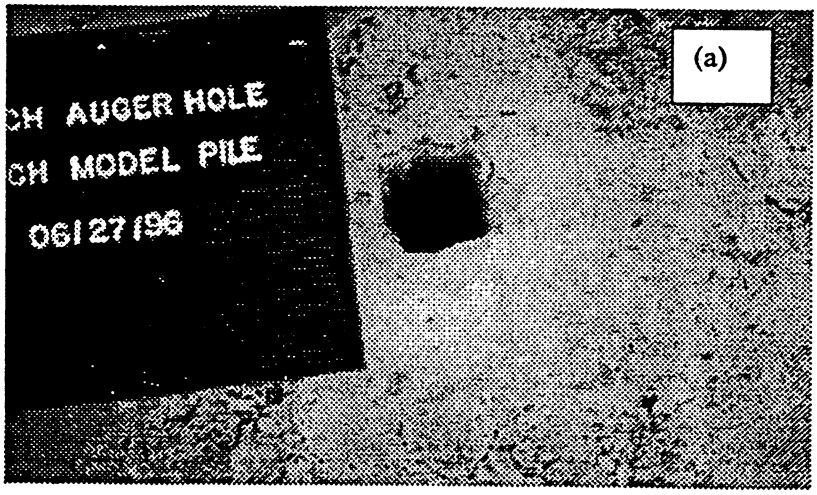

Figure 3.3 (a) Preformed 50.8 mm (2 inch) hole

Figure 3.3 (b) Preformed 50.8 mm (2.0 inch) hole and pile.

Table. 3.2 Influence of pile installation procedure on lateral capacities

Test	Lateral load capacity (kN)	Displacement at failure (mm)
UD_1	3.89	11.56
UP_{11}	3.14	21.84
UP_{12}	2.76	22.10
UP_{13}	2.21	28.71
SD_1	3.40	26.70
SP_{11}	3.10	27.07
SP_{12}	2.60	30.16
SP_{13}	2.16	31.88
UD_2	3.17	25.66
UP_{21}	3.02	28.91
UP_{22}	2.56	34.22
UP_{23}	2.10	40.01
SD_2	3.23	31.06
SP_{21}	2.98	38.59
SP_{22}	2.54	41.25
SP_{23}	2.08	43.25

After insertion, the piles were driven to the required embedment depth. The piles consisted of instrumented hollow aluminum 50.8 mm square pipes with a 1.6 mm wall thickness and 1.52 m length. Then each pile was laterally loaded monotonically. The entire testing procedure is as described in Section 2.3. Table 3.2 shows measured lateral load capacities and displacements at failure for the entire testing program.

Comparison of the preformed piles shows that increasing the preformed hole diameter decreases the lateral load capacity while increasing the lateral displacement at failure. This reduction in the lateral load capacity may be due to the significant reduction in the side shear (frictional resistance, τ_{xy} effect on Fig. 3.4) (Trevor 1987) mobilized to resist the translating preformed pile.

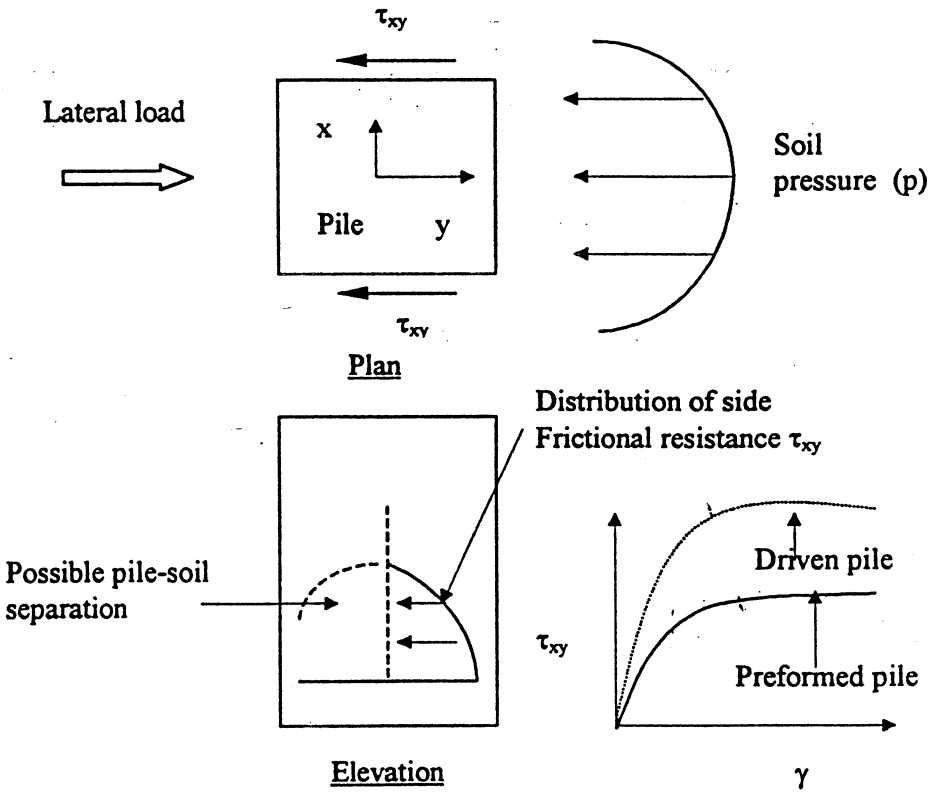

Figure 3.4 Component of soil resistance

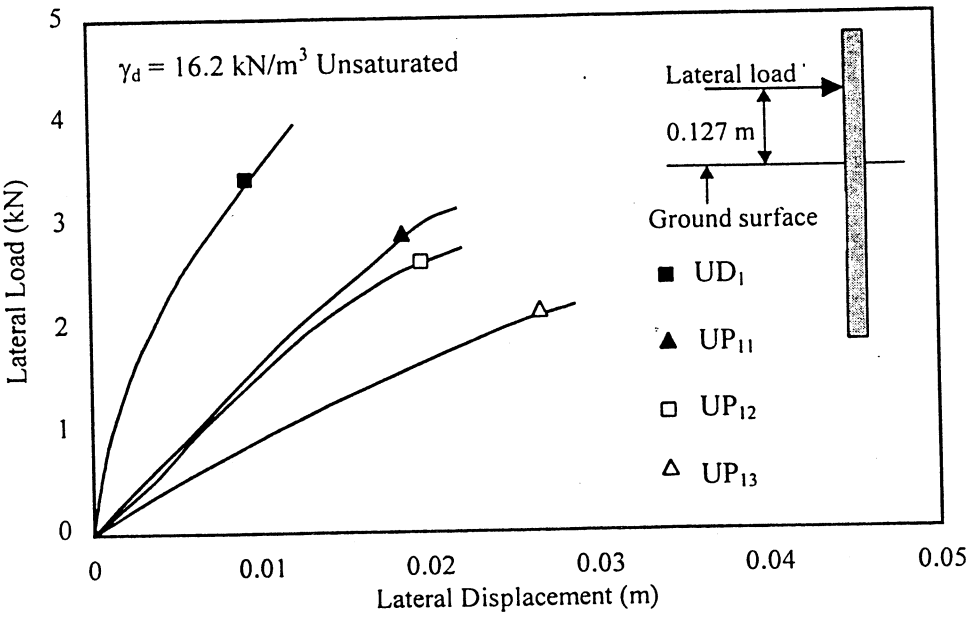

Figure 3.5 Lateral load vs lateral displacement of Preformed piles

Fig. 3.5 shows the lateral load versus lateral displacement for the driven and preformed piles. It is seen that the driven pile and piles preformed in a smaller hole show stiffer behavior than the other piles. This is due to; (1) the vibration and cavity expansion during driving densifies the surrounding soil to different degrees (UD_{I1} and UP_{I1}), and (2) the soil disturbance associated with different degrees of preforming contributes to different levels of lateral confinement relief (UP_{I2} and UP_{I3}). As explained in Fig 3.4, on preforming, the adhesion between pile and soil reduces due to the softening of the surrounding soil. This effect may result in the increased lateral displacement, especially for the 63.5 mm (2.5 inch) preformed pile.

3.2.1 Evaluation of Test Results

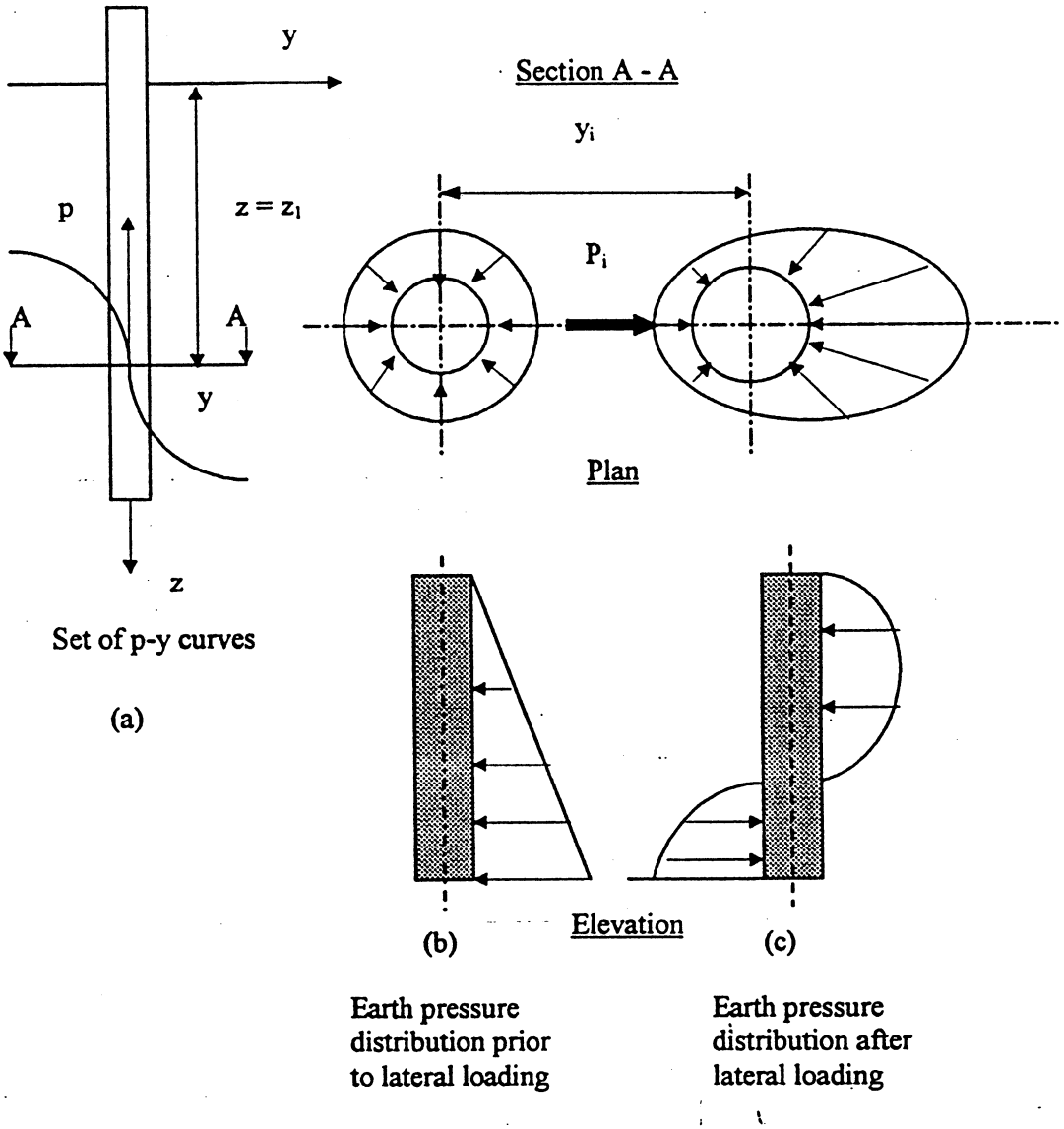

Figure 3.6 Principle of p-y curves

The lateral load behavior of the pile-soil interface along the pile depth is typically represented by p-y curves. The concept of p-y curve can be explained by Figs. 3.6 (b) and

(c). In Fig. 3.6(a) a section (A-A) at a depth z_i is shown through a pile. The earth pressure distribution at A-A prior to lateral loading is shown in Fig. 3.6(b). If the pile is deflected a distance y_i, as shown in Fig. 3.6(c), an asymmetric soil pressure would be developed as shown in the Fig. 3.6(c). Integration of the soil pressure around the pile at A-A would yield an unbalanced force of p per unit length of the pile.

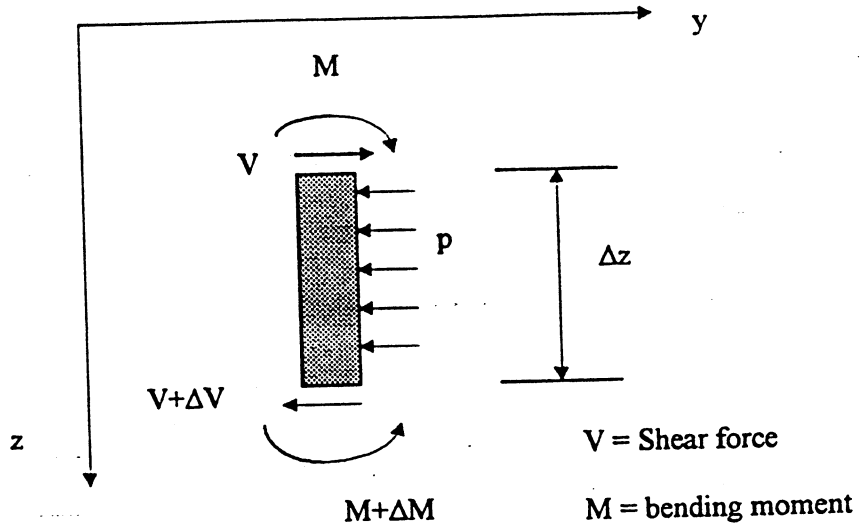

Figure 3.7 Stress on the pile segment

Figure 3. 7 shows that the moment (M) in a pile segment of length (Δz) can be related to the force per unit depth (p) causing this moment by:

$$\frac{d^2M}{dz^2} = p \tag{3.1}$$

Then, by making the usual assumptions of the bending theory, the following can be developed:

$$p = E_p I_p \left(\frac{d^4y}{dz^4}\right) \tag{3.2}$$

where

E_pI_p = flexural stiffness of the pile

Hence the relationship between p and y is highly nonlinear. The method employed for developing p-y curves is explained in Section 2.3.2.

In order to obtaine y, integration of the fitted polynomial suffices, as any slight errors in the strain data become smoothed in the integration process. However for the p, any slight errors or deviations in the strain become greatly magnified during double differentiation. To alleviate this problem, some researchers (Scott 1980; Finn, et al. 1983) fitted local cubic splines between successive stain data points and then derived the pressure (p) and deflection (y) based on them.

However, Scott (1980) found that this did not reduce the magnification of error during double differentiation. Instead, he fitted a fifth degree polynomial to the strain data at each time instant, subject to the constraints that the V is equal to the applied load at the pile top, and y, dy/dz, M, V, and p are all zero at some arbitrary point below the bottom strain gauge. Besides the advantage that small errors in the strain data do not result in large errors in the computed p, the use of a continuous polynomial also eliminates the need for additional numerical differentiation or integration of the moment for the shear, pressure, slope or deflection.

The distribution of strain, deflection and soil pressure computed using the above methodology are illustrated in Figs. 3.8, 3.9 and 3.10 respectively, at an arbitrarily selected load of 1.53 kN during the preformed pile test on the unsaturated soil bed of unit weight 16.2 kN/m^3. The quality of the fitting operation can be seen in Fig. 3.8. where the closeness with which polynomial fits the original data is noted.

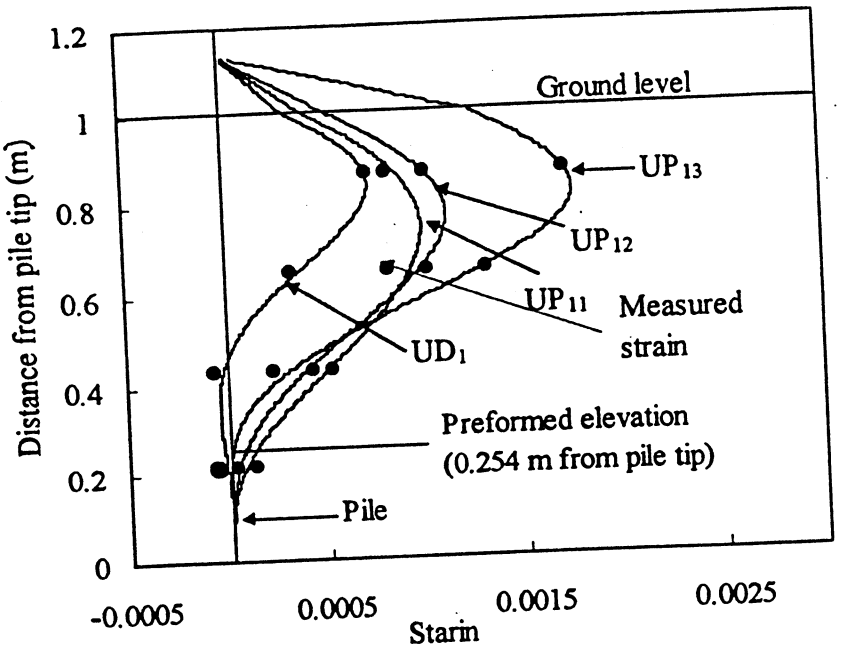

Figure 3.8 Polynomial fit pile strain data vs depth (γ_d = 16.2 kN/m^3 – Unsaturated)

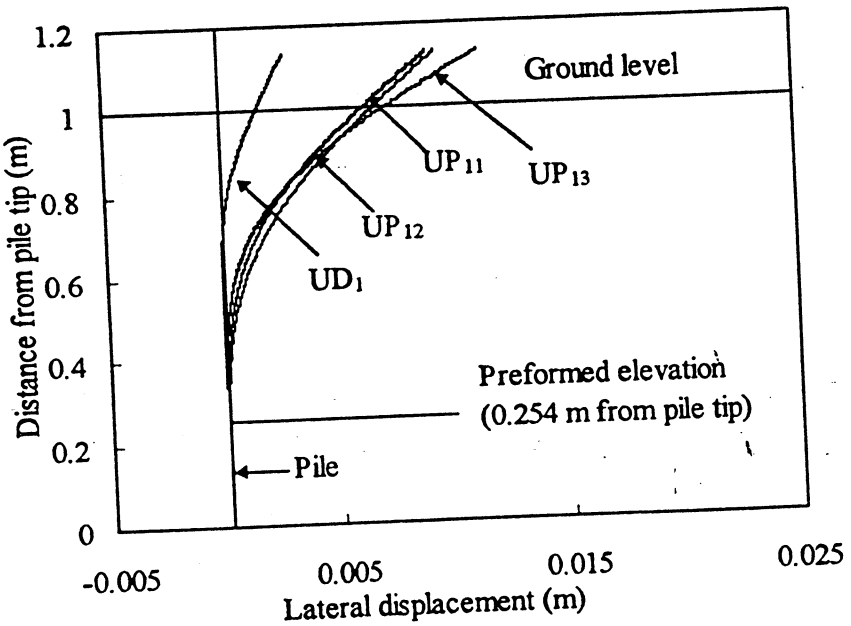

Figure 3.9 Calculated pile displacement vs depth (γ_d = 16.2 kN/m^3 – Unsaturated)

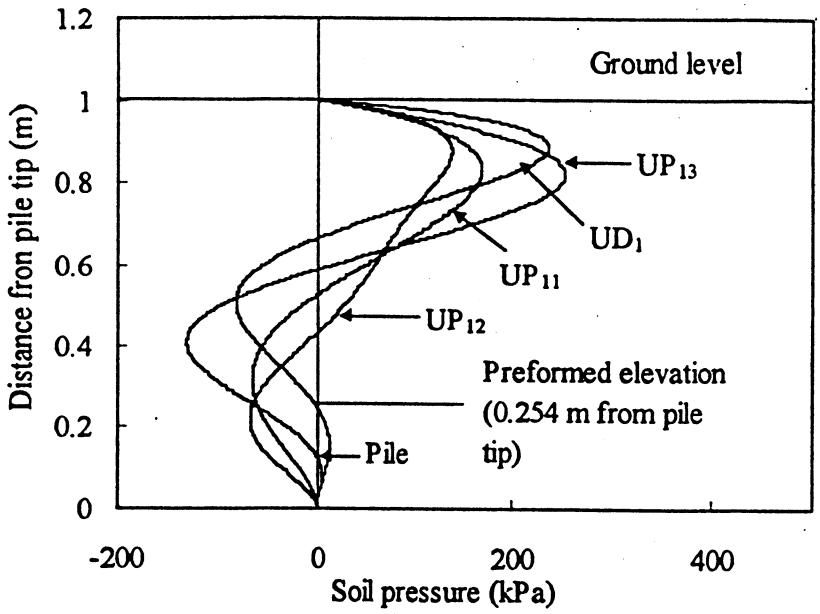

Figure 3.10 Calculated soil Pressure vs depth (γ_d = 16.2 kN/m^3 – Unsaturated)

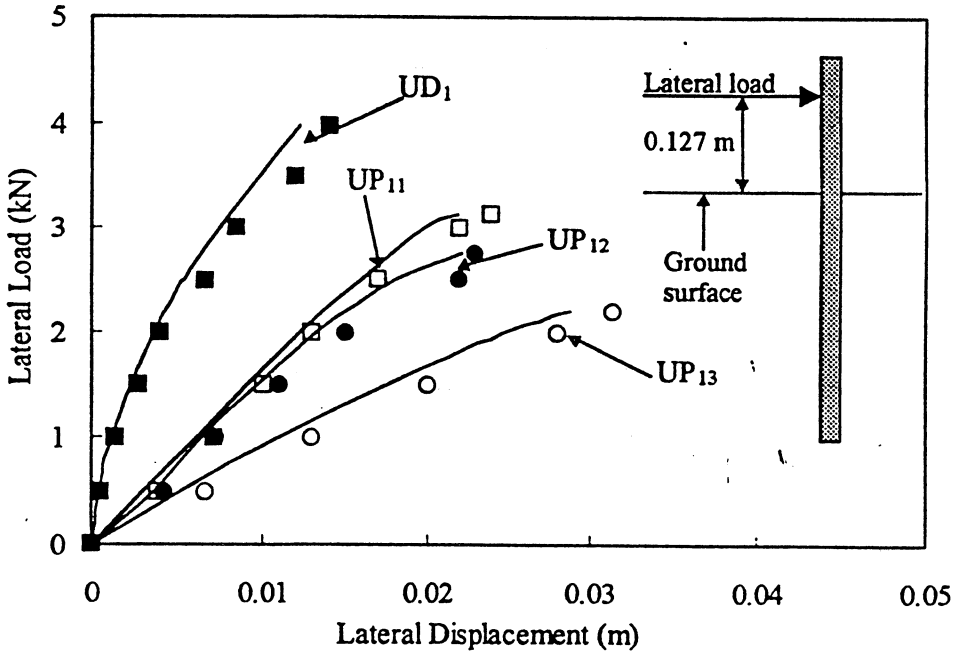

Figure 3.11 Comparison of measured and analytical load-displacement behavior

Fig. 3.11 shows the analytical predictions of lateral load behavior of the driven and preformed piles plotted along with the measured lateral load and displacement, throughout each test.

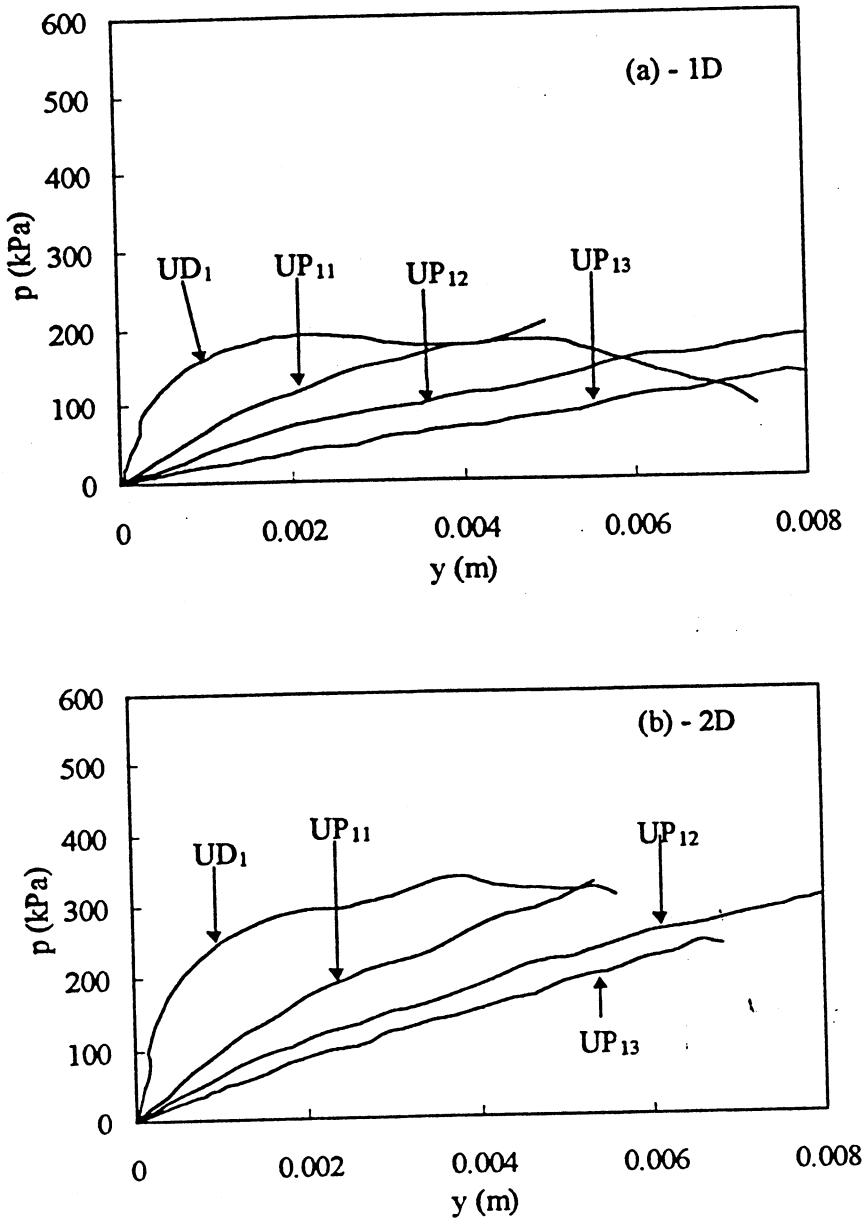

Figure 3.12 p – y curves

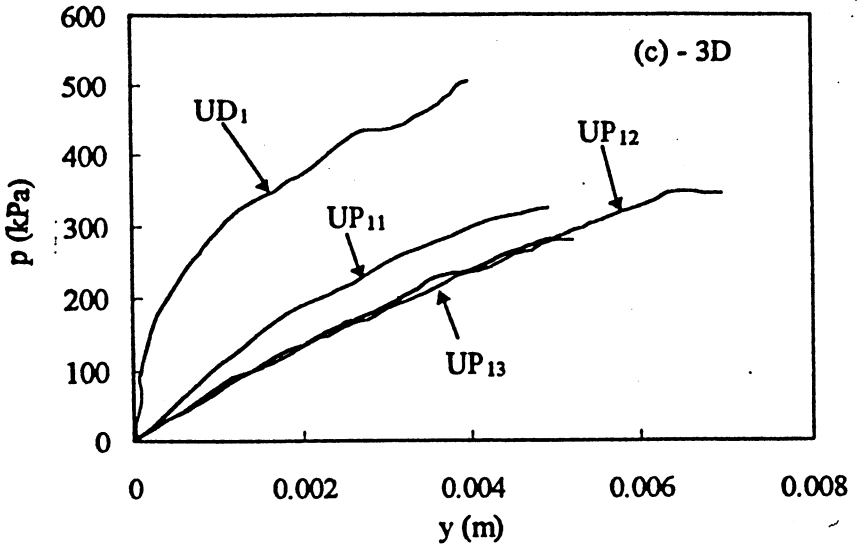

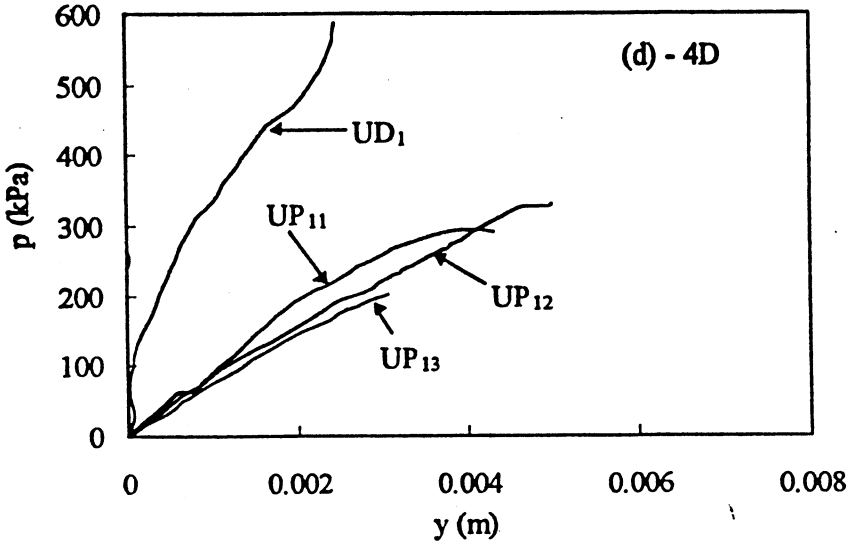

Figure 3.12 (Continued)

As described in section 2.3.1, the pressure and deflection can be computed for any specified depth. Figs. 3.12(a)–(d) illustrate the p-y curves for preformed piles for depths

of 1 – 4 (pile width) below ground level. From these plots, the strain softening at shallower depths and the nearly linear behavior at deeper depths are noted.

All of the preformed piles show very large pile displacements at each depth compared to the driven pile. This is because the different degrees of stress release (or loosening) associated with augering of different size holes enables the surrounding soil to undergo a relatively large displacement before the maximum soil strength is mobilized.

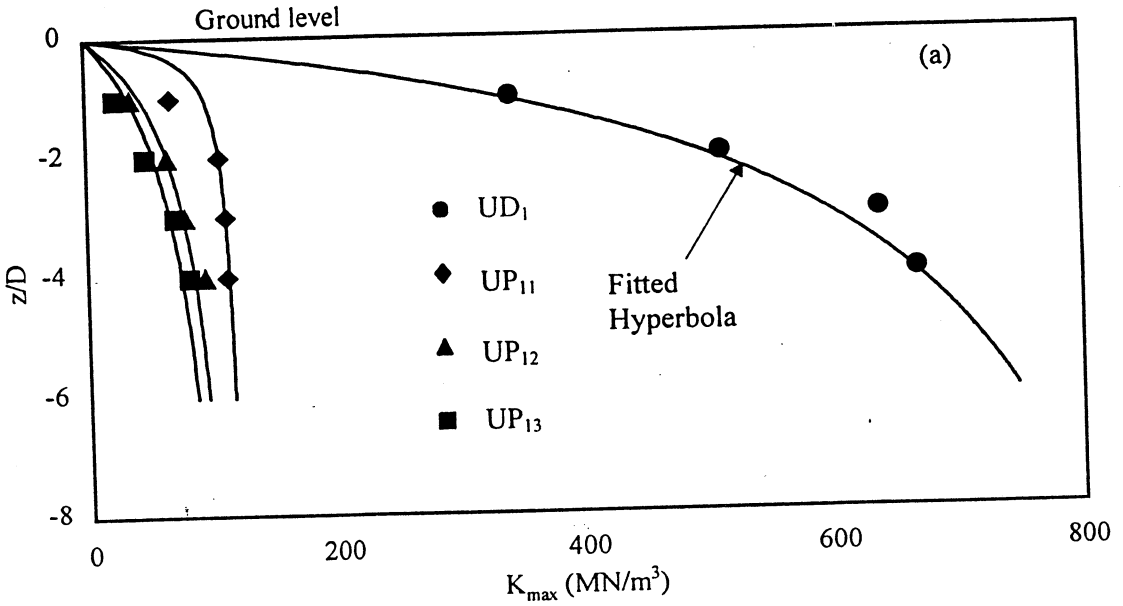

Figure 3.13 (a) Variation of K_{max} with depth

It can be seen from Fig. 3.12 that the general soil-pile interaction behavior at different depths is effected by the confining stress level. Thus, the p-y curves can be normalized by a soil parameter that is also a function of the confining stress level. As explained in Section 2.3.1 this normalization can be carried out using the maximum soil elastic modulus E_{max}, calculated from measured K_{max}. Fig. 3.13(a) compares the K_{max} for

different preformed piles, and the variation of K_{max} with depth represents the confining-stress effect. Many studies have also shown that K_{max} varies as a function of the depth. In this study, the variation of K_{max} with z/D was fitted by a hyperbolic function (K_{max} = (z/D)/(a+b(z/D))). Similarly, the ultimate soil resistance (p_u) is obtained using the method explained in Section 2.3.1 and shown in Fig. 3.13(b).

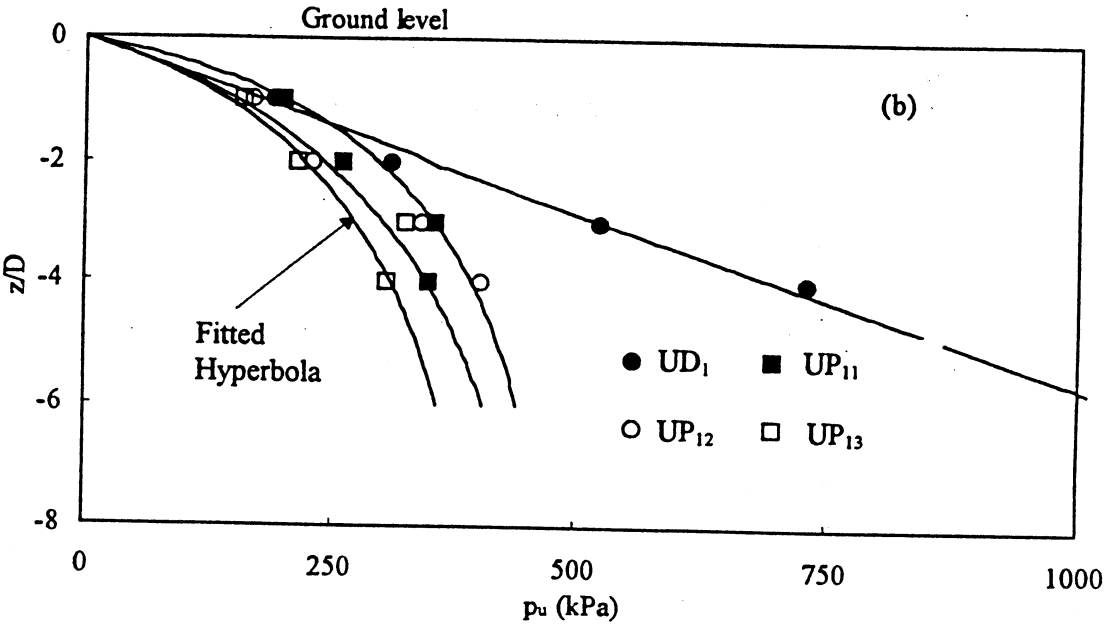

Figure 3.13 (b) Variation of p_u with depth

Table 3.3(a)–(d) show the K-ratio and p_u ratio (K_{pre}/K_{driven} and $p_{u,pre}/p_{u,driven}$ respectively) at each depth for all of the experimental conditions.

Table 3.3 (a). Comparison of curve fitted K_{max} and p_u values (γ_d = 16.2 kN/m^3 Unsaturated)

Depth	UD_1		UP_{11}/UD_1		UP_{12}/UD_1		UP_{13}/UD_1	
	K_{max} (kN/m^3)	p_u (kPa)						
1D	329815	176	0.29	1.14	0.13	0.85	0.10	0.80
2D	496032	352	0.21	0.84	0.13	0.68	0.11	0.63
3D	596484	528	0.18	0.64	0.13	0.57	0.11	0.52
4D	663130	704	0.17	0.54	0.13	0.49	0.11	0.44
5D	711035	880	0.18	0.44	0.13	0.43	0.11	0.38

Table 3.3 (b). Comparison of curve fitted K_{max} and p_u values (γ_d = 16.2 kN/m^3 Saturated)

Depth	SD_1		SP_{11}/SD_1		SP_{12}/SD_1		SP_{13}/SD_1	
	K_{max} (kN/m^3)	p_u (kPa)						
1D	55463	280	0.89	0.92	0.79	0.79	0.68	0.63
2D	76746	435	0.85	0.83	0.78	0.72	0.67	0.55
3D	88002	531	0.83	0.78	0.78	0.69	0.67	0.50
4D	94967	600	0.82	0.75	0.77	0.67	0.67	0.48
5D	99701	647	0.82	0.73	0.77	0.65	0.67	0.46

Table 3.3 (c). Comparison of curve fitted K_{max} and p_u values (γ_d = 14.8 kN/m^3 Unsaturated)

Depth	UD_2		UP_{21}/UD_2		UP_{22}/UD_2		UP_{23}/UD_2	
	K_{max} (kN/m^3)	p_u (kPa)						
1D	58153	144	0.95	0.56	0.64	0.50	0.54	0.45
2D	113884	292	0.65	0.61	0.43	0.58	0.34	0.50
3D	167339	440	0.50	0.69	0.33	0.62	0.25	0.56
4D	218656	628	0.41	0.51	0.27	0.46	0.20	0.42
5D	267960	740	0.35	0.45	0.23	0.41	0.17	0.37

Table 3.3 (d). Comparison of curve fitted K_{max} and p_u values (γ_d = 14.8 kN/m^3 Saturated)

Depth	SD_2		SP_{21}/SD_2		SP_{22}/SD_2		SP_{23}/SD_2	
	K_{max} (kN/m^3)	p_u (kPa)						
1D	21218	195	0.89	0.45	0.94	0.30	0.52	0.27
2D	38366	304	0.86	0.44	0.73	0.31	0.44	0.27
3D	52512	380	0.83	0.43	0.62	0.31	0.39	0.26
4D	64381	421	0.81	0.43	0.55	0.32	0.35	0.27
5D	74482	456	0.80	0.43	0.50	0.33	0.33	0.27

Finally, K-ratios (K_{pre}/K_{driven}) and p_u-ratios ($p_{u,pre}/p_{u,driven}$) obtained from the entire testing program are plotted against the non-dimensional preformed hole diameter and shown in Figs. 3.14(a)-(b).

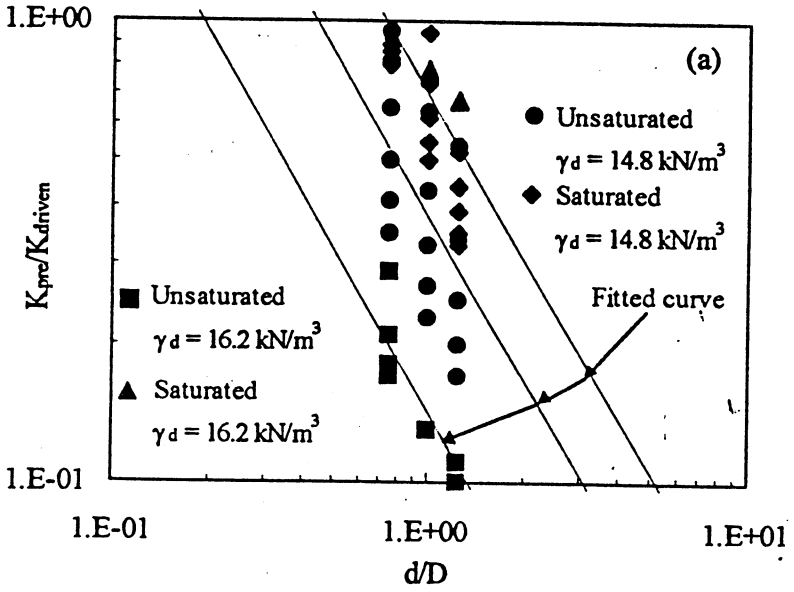

Figure 3.14 (a) K - ration vs d/D

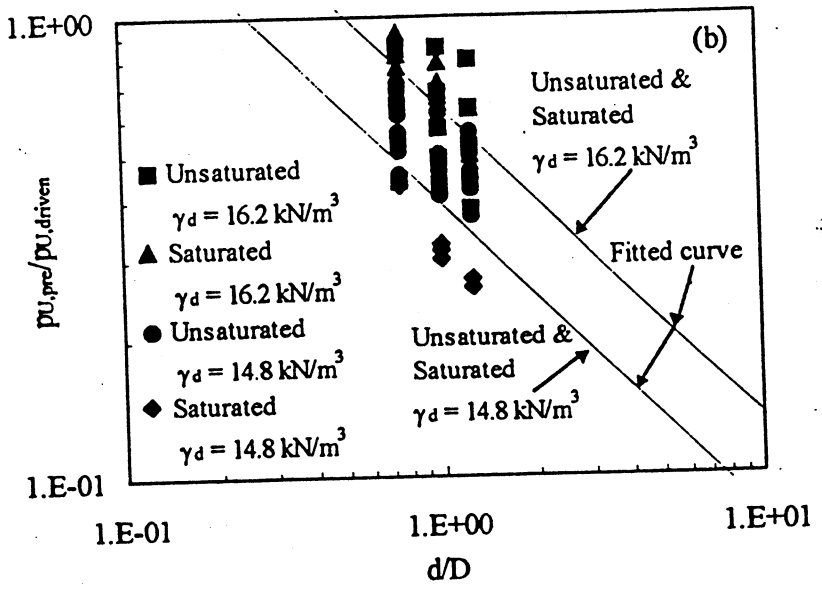

Figure 3.14 (b) p_U – ratio vs d/D

Based on Fig. 3.14, the K-ratio and p_u-ratio can be related to the non-dimensional preformed hole diameter by following equations.

$$\frac{K_{pre}}{K_{driven}} = \alpha_3 \left(\frac{d}{D}\right)^{\beta 3} \tag{3.3}$$

$$\frac{Pu,pre}{Pu,driven} = \alpha_4 \left(\frac{d}{D}\right)^{\beta 4} \tag{3.4}$$

Where, α_3, α_4, β_3 and β_4 are soil type parameters which can be determined by the respective intercepts and slopes that Eqn. (3.3) and (3.4) produce on a log-log scale. The fitted values are shown in Table 3.4(a) and (b).

Table. 3.4 (a) Parameters for Eqn. (3.3)

Parameters	16.2 kN/m^3		14.8 kN/m^3	
	Unsaturated	Saturated	Unsaturated	Saturated
α_3	0.14	0.69	0.38	0.69
β_3	-1.17	-1.17	-1.17	-1.17

Table 3.4 (b) Parameters for Eqn. (3.4)

Parameters	16.2 kN/m^3	14.8 kN/m^3
α_4	0.64	0.39
β_4	-0.68	-0.68

The values for β_3 and β_4 seem to be independent of the foundation medium unit weight and the groundwater table level. On the other hand, the values of α_3 and α_4 seems to be dependent on foundation medium unit weight and groundwater table. Hence one can assume the variation of α_3 and α_4 to be linearly proportional to the foundation medium unit weight.

3.2.2 Numerical Example

If a field p-y curve of a *driven pile* in a soil type similar to the tested soil (clayey sand) is available, based on either (1) experimental data, (2) Reese et. al.(1974) method (Fig. 2.18 (a)), or (3) Murchison and O'Niell's (1984) method (Fig. 2.18 (b)), and, if one neglects the possible errors due to scale effects, then one can generate p-y characteristics for a pile to be *preformed-driven* in the same soil type. The impact of any scale effect can be identified only by comparing these p-y curves with those obtained from field tests.

In order to illustrate this, assume that a p-y curve based on Murchison and O'Niell's (1984) method is available for a *driven pile* (with D=0.61 m (24 inches) square)

at a clayey site (γ_d = 15.76 kN/m^3) above the groundwater table. Further, assume that the relevant parameters at a 3D depth are A_d = 1, $p_{u,d}$ = 900.00 kPa and $K_{max,d}$ = 30000.00 kN/m^3. The subscript "d" indicates a driven pile. Using these values, the corresponding p-y curve can be plotted as shown in Fig. 3.15.

Then, assume that one is interested in synthesizing a p-y curve at 3D for a pile to be inserted in a preformed hole of d=0.46m (18 inches). Accordingly, the corresponding equivalent non-dimensional preformed hole diameter (d/D) is 0.75. Hence the constants α_3, α_4, β_3 and β_4 can be obtained by linear interpolation based on the values given in Tables. 3.4(a) and (b). Table 3.5 shows the interpolated values at a 15.76 kN/m^3 unit weight. It has been *assumed* that the *range of values* shown in Table 3.4 are generally valid for any other soil similar to the tested one.

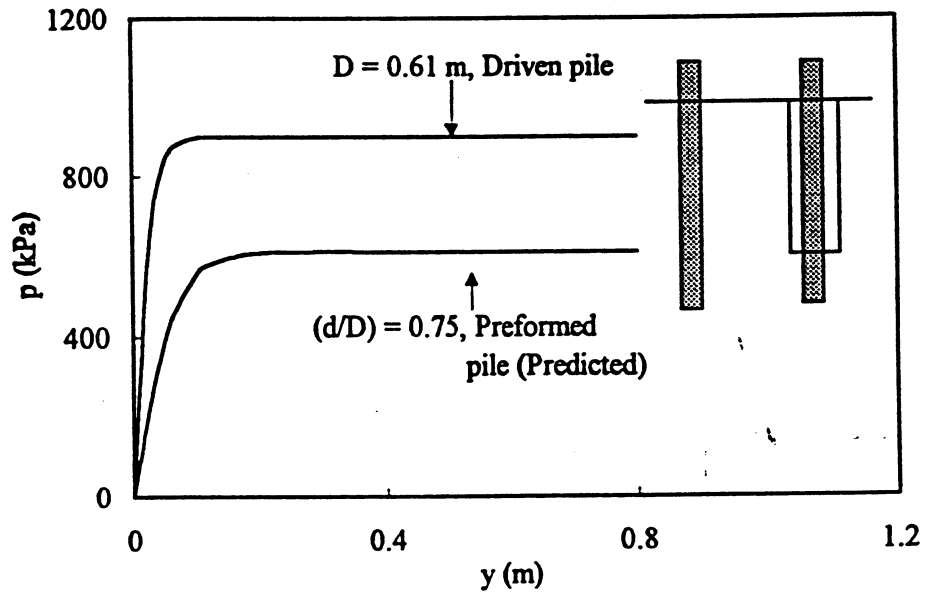

Figure 3.15 Predicted p-y curve

Table 3.5 Interpolated constants for use in Eqns. (3.3) and (3.4)

Unit weight (kN/m^3)	$\frac{d}{D}$	α_3	α_4	β_3	β_4
15.76	0.75	0.22	0.56	-1.17	-0.68

Using Eqns. (3.3), (3.4) and Table 3.5, the K - ratio and p_u - ratio can be determined as 0.31 and 0.68 respectively. Thus, the corresponding p-y parameters at a 3D depth, for the pile to be inserted in a 0.46 m hole are, A_j = 1.0, $K_{max,j}$ = 9300.00 kN/m^3 and $p_{u,j}$ = 612 kPa. The correspondingly deduced p-y curve is also plotted in Fig. 3.15.

This example shows how one can use Eqns. (3.3) and (3.4) to easily generate the p-y curve for a pile to be inserted in any desired preformed hole in the field. It must be noted that the same procedure can be extended to obtain p-y curves for any desired *preformed hole diameter* based on p-y curves for *driven* piles also available in terms of Reese et. al. (1974) method or experimental data.

3.3 Numerical Modeling of the Lateral Load Behavior of Preformed Piles

3.3.1 Introduction

The lateral load behavior of preformed piles was numerically modeled using the finite element program ABAQUS developed by Hibbit, Karlsson & Sorensen, Inc (1995). This is a finite element code that enables the solution of transient elasto-plastic or large displacement problems using step by step integration. It can be applied to plane stress, plane strain, axisymmetric and three dimensional domains. In this work, the nonlinear

response of preformed pile foundations to monotonic lateral loading is investigated in order to gain a better understanding of the effects of preforming.

3.3.2 Estimation of Existing Confining Stress

An estimation of the existing confining stress needs to be done in order to determine the parameters required for the constitutive modeling of the soil skeleton. Expanding cavity theory (Vesic 1972) provides a procedure to carry out such an estimation. According to expanding cavity theory, the process of pile penetration into the soil can be simulated by the expansion of a cylindrical or spherical cavity in the soil. In this regard, the stress along the pile shaft generated by the penetration of the pile can be simulated by an expanding cylindrical cavity and the stress around the pile tip induced by the penetration of a solid pile can be simulated by an expanding spherical cavity.

The cylindrical cavity expansion problem is simplified to one of plane strain; the soil is modeled as an elasto-plastic material obeying the Mohr-Coulomb criterion and the effects of volume change in the plastic region are included. Based on these assumptions, the stresses σ'_r and σ'_θ at the peripheral pile-soil contact due to the penetration of the pile can be determined as functions of the angle of internal friction (ϕ), elastic modulus, Poisson's ratio, pile diameter, the existing radial stress (σ_0) and the shear volume change characteristics of the soil. The application of this theory to the present problem is described next.

According to expanding spherical cavity theory, the effective radial stress in a cohesive soil mass due to pile tip penetration can be expressed as:

$$\sigma_r = cFc + qFq \tag{3.5}$$

where

Fc and Fq = dimensionless spherical cavity expansion factors

c = cohesion

q = in-situ effective isotropic stress prior to driving

The spherical cavity expansion factors, Fc and Fq, can be written as

$$F_q = \frac{3(1+\sin\Phi)}{3-\sin\Phi}\left[I_{rr}\right]^{4\sin\Phi/\left[3(1+\sin\Phi)\right]} \tag{3.6}$$

$$F_c = \left(F_q - 1\right)\cot\Phi \tag{3.7}$$

where

I_{rr} = reduced rigidity index

ϕ = drained angle of internal friction

The reduced rigidity index, I_{rr}, can in turn be expressed in the following form

$$I_{rr} = \frac{I_r}{1+I_r\Delta} \tag{3.8}$$

where

I_r = rigidity index

Δ = average volumetric strain in the plastic zone

Finally, for a cohesive soil, I_r can be written as

$$I_r = \frac{E}{2(1+\nu)(c+q\tan\Phi)} \tag{3.9}$$

where

E = soil modulus of elasticity

ν = soil Poisson's ratio

First, the value of I_r was evaluated at q = 8.97 kPa (average confining pressure between pile top and bottom) based on soil parameters.

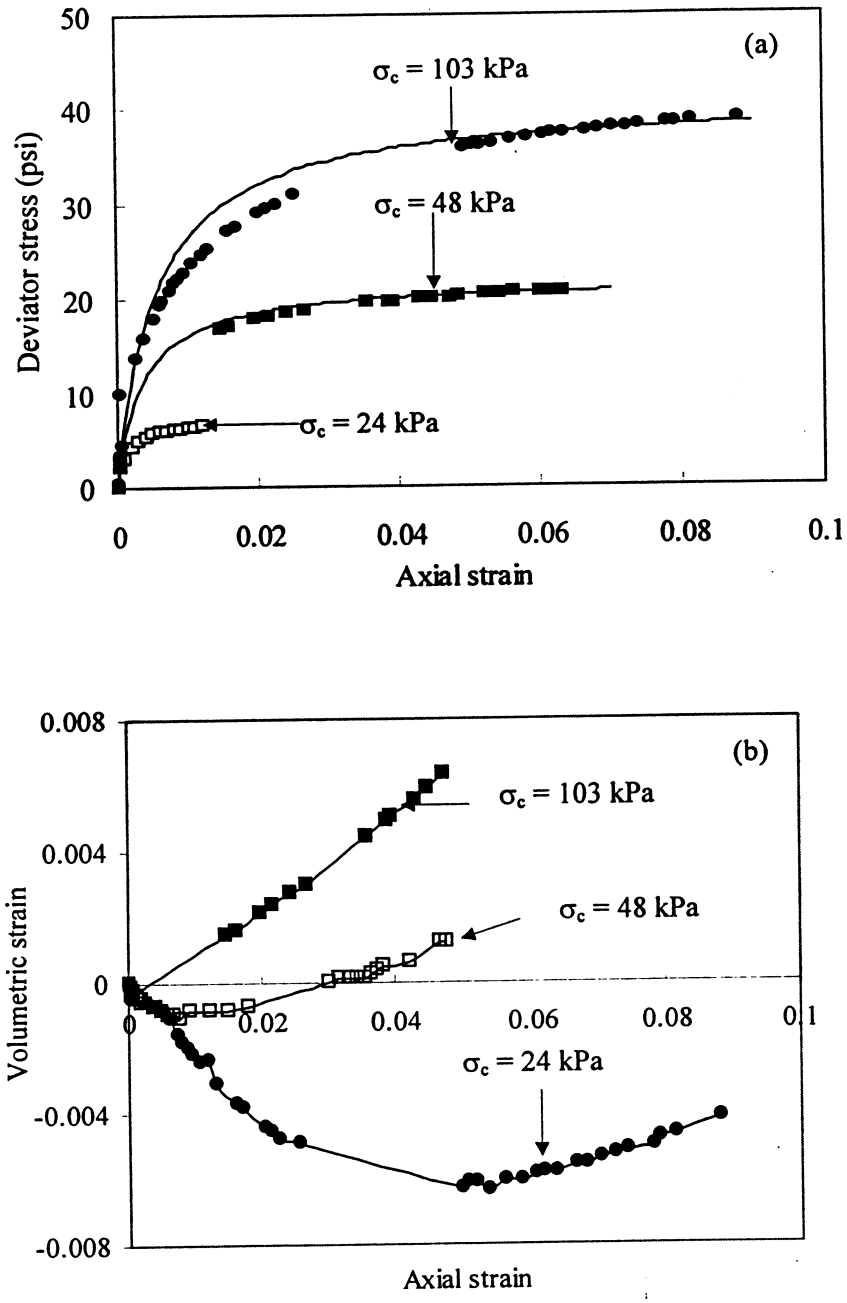

Figure 3.16 Drained test results on test pit soil at different confining pressures

To determine the soil properties E, c and ϕ, drained triaxial tests were carried out at different confining pressures and the results are illustrated in Fig. 3.16(a)-(b). Table 3.6 shows the initial modulus of elasticity E_i and the ultimate stress at failure $(\sigma_1-\sigma_2)_f$ for different confining pressures. The values of E_i and $(\sigma_1-\sigma_2)_f$ are determined by fitting a hyperbola to the curve in Fig. 3.16(a) (Kondner, 1963).

Table 3.6 E_i and $(\sigma_1-\sigma_2)_f$

Confining pressure (kPa)	E_i (MPa)	$(\sigma_1-\sigma_2)_f$ (kPa)
24	35.5	103
48	42.0	151
103	51.4	230

Using the data in Table 3.6, C and ϕ are determined as 10.3 kPa and 32.73°. Further, the initial elastic modulus corresponding to 9 kPa confining pressure is determined based on the following relationship (Duncan and Chang 1970) while the fitted curve is shown in Fig. 3.17.

$$E_i = a.P_a\left(\frac{\sigma_c}{P_a}\right)^b \tag{3.10}$$

where

a = a constant

b = the exponent determining the rate of variation of E_i and σ_c

P_a = atmospheric pressure expressed in the same pressure unit as E_i (101 kPa)

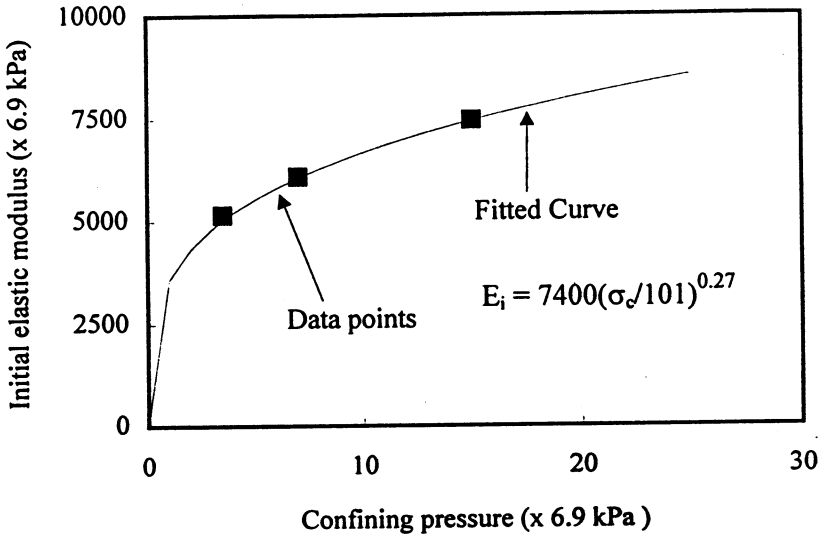

Figure 3.17 Variation of E_i vs σ_c

From extrapolation, E_i = 26.5 kPa is found for q = 9 kPa. By substituting these values in Eq. (3.9) together with the values of c = 10.3 kPa, $\phi = 32.73°$, $\nu = 0.3$ and q = 9 kPa, one can determined I_r to be 633.

In order to determine I_{rr}, the average volumetric strain in plastic zone, Δ, must determined first. According to Vesic (1972), Δ can be written as

$$\Delta = C_0(f_x - 1)\left(\frac{q}{\sigma}\right)^x + C_3 + C_4 f_x\left(\frac{q}{\sigma}\right)^x \tag{3.11}$$

where

$$f_x = \frac{(3)^{1+x}(1+\sin\phi)(1-\sin\phi)^x}{\left[3+(3-4x)\sin\phi\right](3-\sin\phi)^x} \tag{3.12}$$

and

σ = unit effective stress for non-dimensionalizing q, (usually taken as 6.9 kPa)

x = is a parameter between 0 and 1

The first term in Eq. (3.11) represents the contribution of the isotropic stress to the volumetric strain and the last two terms represent the contribution of deviatoric stress to the volumetric strain.

The value C_0 can be obtained from the results of an isotropic triaxial compression test together with the following expression

$$\Delta' = C_0\left(\frac{\sigma_0}{\sigma}\right)^m \tag{3.13}$$

where

m = an exponent which can vary between 0 and 1

σ_0 = the applied mean normal stress

The isotropic triaxial compression test data and the fitted curve are shown in Fig. 3.18 from which C_0 can be determined as 0.003173.

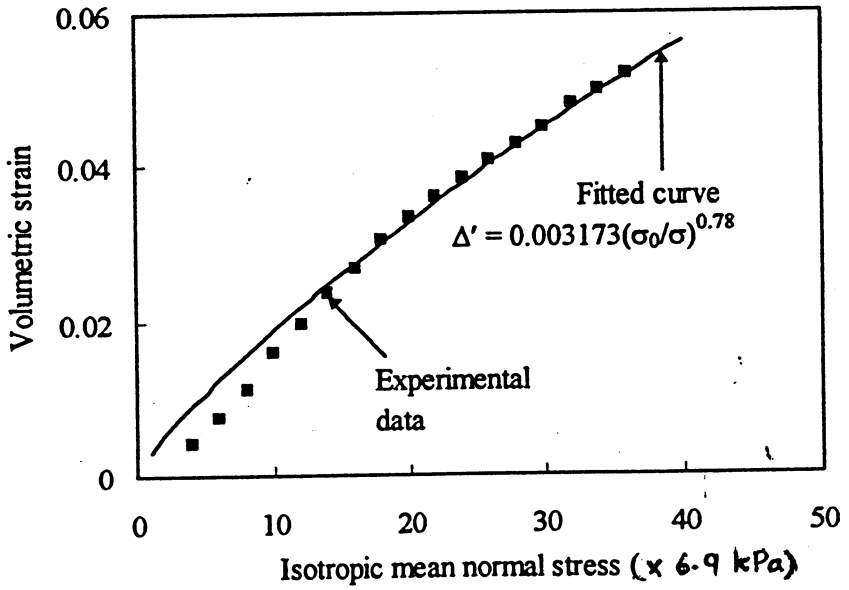

Figure 3. 18 Isotropic triaxial compression test results

On the other hand, the coefficients C_3 and C_4 are found by fitting a curve relating volumetric strain from the triaxial tests, at failure, Δ'', to the effective confining stress in the triaxial test, σ_c

$$\Delta'' = C_3 + C_4\left(\frac{\sigma_c}{\sigma}\right)^n \tag{3.14}$$

where

n = an exponent varying between 0 and 1

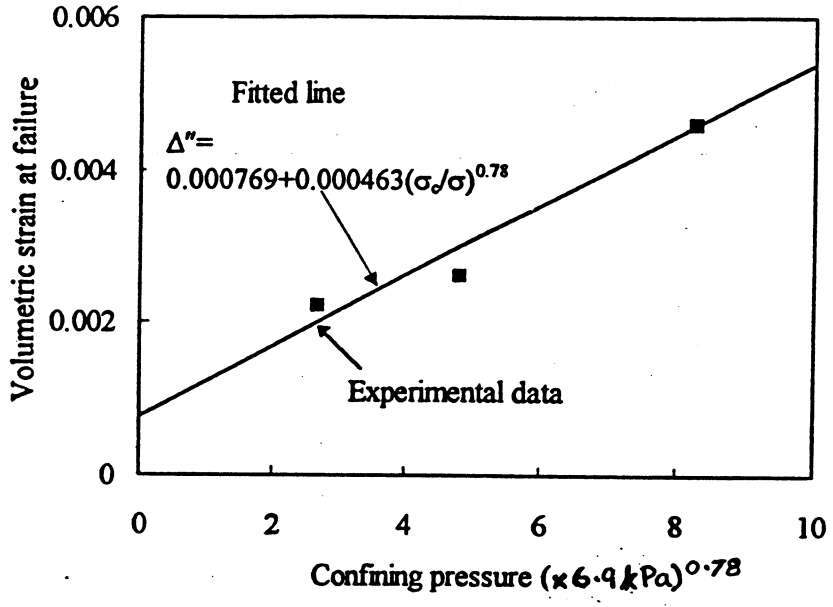

Figure 3.19 $(\varepsilon_v)_{failure}$ versus $(\sigma_c)^{0.78}$

A good fit between Δ'' and σ_c is found if the parameter n is set equal to 0.78. Then from Fig. 3.19, C_3 and C_4 are found to be 0.000769 and 0.000463 respectively. Finally, using Eq. (3.11) and (3.12), the value Δ is found to be 0.00135 for a spherical cavity. Similarly, using the corresponding equations (Vesic 1970) for a cylindrical cavity, Δ is found to be 0.000226.

By substituting this Δ value together with the value I_r in Eq. (3.9), the values of I_{rr} for spherical and cylindrical are determined to be 341.4 and 541.1 respectively. Eventually, using Eqs. (3.6) and (3.7), Fc and Fq for a spherical cavity are 43.8 and 29.2 respectively. Similarly, use of the corresponding equations for cylindrical cavity (Vesic, 1972) yields F'q = 14.9 and F'c = 21.63.

Having determined the above parameters, the magnitude of σ_r at the pile tip and the ground level are found to be 973 kPa and 222 kPa respectively. Then, the values of σ_θ can be found from the following expression given by Vesic (1972) as 267 kPa and 55.9 kPa at the pile tip and the ground level respectively.

$$\sigma_\theta = \left(\frac{1-\sin\phi}{1+\sin\phi}\right)\left(\sigma_r + c \times \cot\phi\right) - c \times \cot\phi \qquad (3.15)$$

For an existing vertical stress, σ_z, equal to the existing in-situ stress of 2.58 psi, the mean confining stress p of (973+267+17.8)/3 = 419 kPa is computed at the pile tip. The same calculation is repeated at the ground level as p = (222+55.9+0)/3 = 92.6 kPa.

Hence the initial mean confining stresses to be input into the finite element model are 92.6 kPa at the pile top and 419.2 kPa at the pile tip with a linear variation in-between. On the other hand, the lateral effective normal stress along the edge of the test pit are 0 and 25.2 kPa at the ground level and the pit bottom respectively with a linear variation in-between. Further, the variation of confining stress in the radial direction will also be linear between the pile and the edge of the test pit in accordance with results of expanding cavity theory, for the case of dense soil (Vesic, 1972).

As explained earlier, the confining stress in the row of finite elements immediately below the pile tip are assumed to be the same as those at the tip level. This assumption is not expected to introduce significant errors since the magnitude of the elastic soil modulus is proportional to the 0.27 power of confining stress (Fig. 3.17). Finally, the confining stress in the bottom row of finite elements is considered to be the same as the in-situ stress since they are located outside the perceived influence zone (distance of larger than two pile diameters from the pile).

The coefficient of earth pressure at-rest, K_0, is an important consideration in the analysis of piles. It has been reported by Hagerty (1975) that the value of K_0 near the pile wall immediately after driving may have values as high as 1.28 and that this value decreases linearly in the radial direction to a value of $\nu/(1-\nu)$ at a distance of four pile diameters. However, it is also reported that a simplified analysis which considers a constant value of K_0, equal to that close to the pile wall, throughout the finite element region provides results which are in agreement with those obtained using a variable K_0. Hence, in the present study, since the minimum value of K_0 ($\nu/(1-\nu)$) is about 0.5, a constant K_0 value equal to 1.0 was chosen. Therefore, the initial mean confining stresses determined above are introduced into the analysis as isotropic stresses (i.e $\sigma_r = \sigma_\theta = \sigma_z$).

The confining pressure used to determine the constitutive properties of the soil skeleton adjacent to the pile is considered for simplicity as the average of the confining pressures at the ground level and pile tip ((92.6+419.2)/2 = 255.9 kPa). The confining pressure used to determine the constitutive properties of the soil skeleton for all the remaining soil elements is an average of the initial confining pressures determined in the previous paragraph. The average confining pressure along the test pit edge is 14.5 kPa.

Thus the average confining pressure of the soil not in contact with the pile is approximately 114.7 kPa. For the preformed piles, the average confining pressures of the soil skeleton for soil adjacent to the pile and the remaining soil is calculated as follows. For 50 mm and 63 mm preformed piles, the nodes at the peripheral of the preformed hole was loaded with a uniform linearly distributed lateral stress (tensile stress, average lateral stress due to overburden from ground surface to 0.74m depth), 6.7 kPa, assuming the mesh consisting of homogeneous soil elements. The procedure was followed in order to simulate the stress release due to excavation. The resulting state of stress and the strain (ε_x) at each element was obtained. Then average confining stress (σ_c) and ε_x from ground level to 0.74m was computed. For the 38 mm preformed pile, in the first step stress was released as explained above. In the second step the computed stress from first step was applied to the soil elements then nodes at the peripheral were laterally displaced (6.35mm) to simulate the 50 mm pile driving. The σ_c and ε_x are given in Table 3.7.

Table 3.7 σ_c and ε_x

Pile	Average σ_c (kPa)	Average ε_x
UD_1	115	-
UP_{11}	99	0.022
UP_{12}	35	0.011
UP_{13}	22	0.007

The elastic modulus used for the finite elements were obtained using following procedure. For the driven pile, Eqn. (3.10) was used. For preformed piles, first triaxial

stress-strain curves given in Fig. 3.16 (a) were normalized with respect to their confining pressure. Fig. 3.20 shows the normalized stress-strain curve.

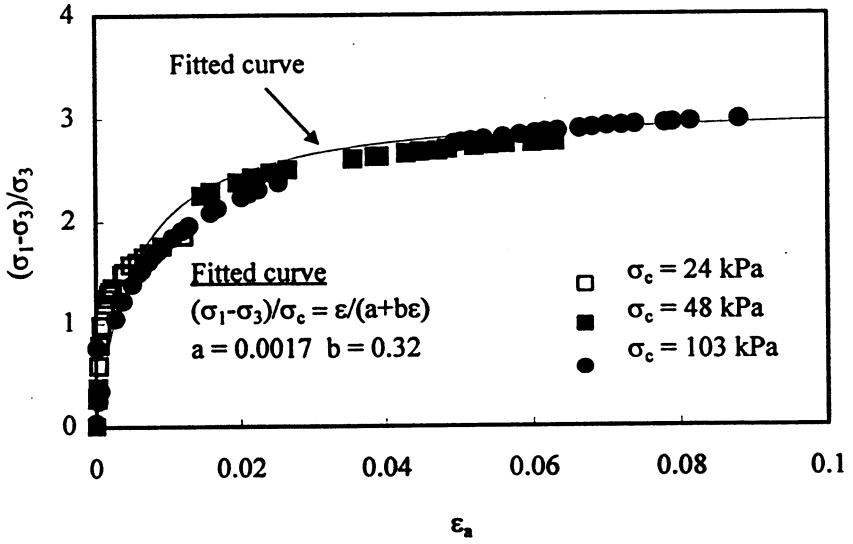

Figure 3.20 Normalized stress-strain curve

Then using ε_x (Table 3.7) and the Fig. 3.20, corresponding normalized deviator stresses were obtained. Knowing confining stress (Table 3.7) the secant elastic modulus (E_{sec} = $(\sigma_1-\sigma_3)/\varepsilon_x$) were obtained. The elastic modulus used for the finite elements are given in Table 3.8.

Table 3.8 Elastic moduli used in modeling

Pile	E (MPa)
UD_1	50.5
UP_{11}	11.4
UP_{12}	6.7
UP_{13}	5.4

3.3.3 Material Constitutive Laws

3.3.3.1 Pile Model

The aluminum model pile material is modeled as a Von Mises elastic, perfectly plastic material. The Von Mises yield criterion is selected because of its ability to simulate shearing without plastic volumetric strains. The basic properties for the *6063-T5* aluminum used in the model is given in Table 3.9, obtained from *Welding Kaiser Aluminum Co.*

Table 3.9 Basic properties of aluminum model pile

Properties	Values
E_p	16215 MPa
ν	0.33
σ_Y	110 MPa
ρ_p	2,670 kg/m^3

As mentioned in Section 2.3, tested piles were of 50mm square and 1.6 mm thick hollow cross-section. However, in the finite element analysis, the pile cross-section was considered to be solid. Hence the equivalent elastic modulus shown in Table 3.9 was obtained by equating the flexural stiffness of the actual hollow pile to that of the modeled solid pile.

3.3.3.2 Soil Model

The deformation of the soil is assumed to be linear elastic, modeled by the classical theory of elasticity, and plastic. The plastic model used for the soil is an extension of the Drucker-Prager Cap plasicity model. This model was selected from the soil models available in the library of ABAQUS because of its ease of implementation and the ability to model the hardening behavior of clayey sand. The Drucker-Prager Cap model assumes two yield surfaces in the p-t plane: a shear failure surface, providing dominantly shear flow, and a "hardening cap" which intersects the equivalent pressure stress axis as shown in Fig. 3.21. There is a transition region between these segments, introduced to provide a smooth surface.

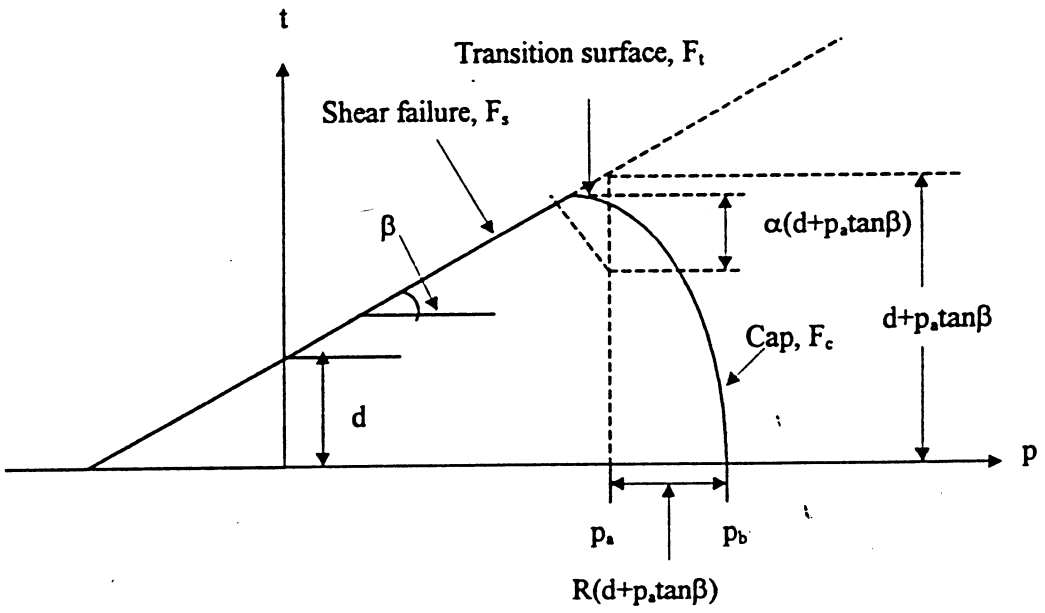

Figure 3.21 Modified Drucker-Prager Cap model: yield surface in the p-t plane.

The stress space is defined with p, the first stress invariant, and t, the square root of the second deviatoric stress invariant. Fig. 3.22 shows the shape of the same failure surface in the deviatoric plane, as a circle. S_1, S_2 and S_3 are the deviatoric stress components. In ABAQUS t is given by:

$$t = \frac{1}{2}q\left[1 + \frac{1}{K} - \left(1 - \frac{1}{K}\right)\left(\frac{r}{q}\right)^3\right] \tag{3.16}$$

Depending on the value of K the failure surface in the deviatoric plane will take different shape.

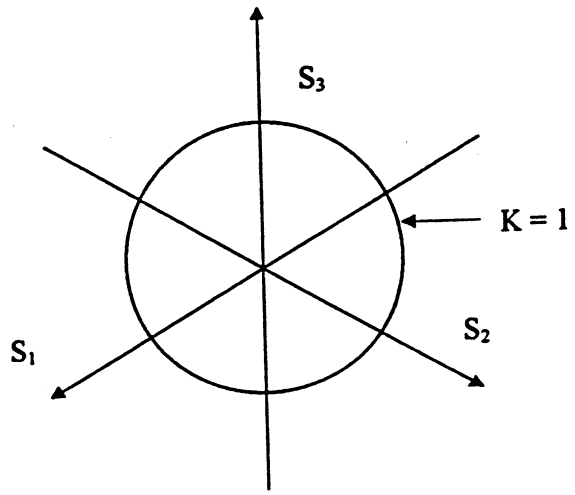

Figure 3.22 Typical yield/flow surface in the deviatoric plane.

The cap model serves two main purposes; (1) it bounds the yield surface in hydrostatic compression, thus providing an inelastic hardening mechanism to represent plastic compaction, and (2) it helps to control the volume dilatancy when the material

yields in shear by inducing softening as a function of the inelastic volume increase resulting from the yielding on the Drucker-Prager failure surface and the transition yield surface.

The model uses an associated flow rule in the cap region and a non-associated flow rule in the shear failure and transition region. Further details of these models can be found in the ABAQUS theory manual (1995).

In order to determine the required model parameters, two CU triaxial tests were performed using the tested soil at confining pressures of 41.9 kPa and 138 kPa as shown in Fig. 3.23. The derived model parameters are shown in Fig. 3.23.

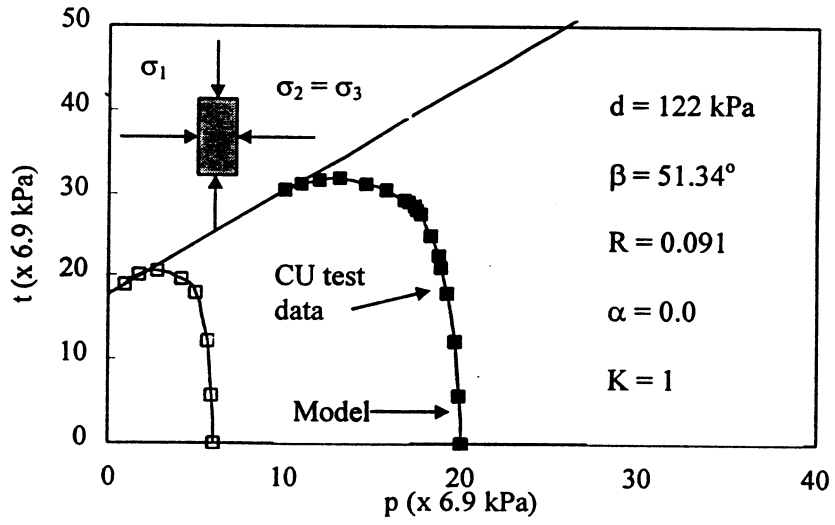

Figure 3.23 Undrained Triaxial test paths for the tested clayey sand in the p-t plane

Solid three-dimensional "brick" elements were used to model the pile as well as the soil, thus making pile elements compatible with the soil elements. With respect to the type of displacement function used, they were 8-node quadratic isoparametric elements.

3.3.3.3 Interface Model

The pile-soil interface is modeled as perfectly elastic, since the pile and the adjacent soil were assumed to behave elastically and perfectly bonded. This assumption allows soils to undergo large displacements during lateral loading without causing instability. The constitutive parameters that define the interface element are the elastic modulus, Poisson's ratio.

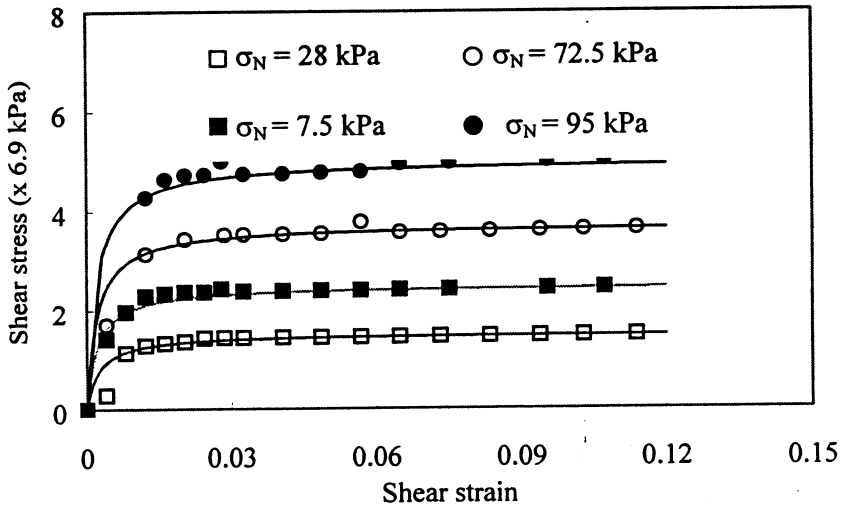

Figure 3.24 CD direct shear test results

The elastic stiffness is found from the results of CD Direct Shear tests performed by placing the tested soil against an aluminum plate made of the model pile material. The results are shown in Fig. 3.24. The initial shear modulus, G, is determined by fitting a hyperbola to the shear stress versus shear strain curve in the form

$$\tau = \frac{\gamma}{a + b\gamma} \tag{3.17}$$

It can be shown that the initial shear modulus is equal to 1/a (Kondner, 1963). Then, the initial elastic modulus is obtained by using following equation:

$$G = \frac{E}{2(1+\nu)} \tag{3.18}$$

Table 3.10 shows the E and τ_f values correspond to normal stresses of 27.6 kPa, 49,7 kPa, 77.5 kPa and 95.2 kPa obtained using Eqs. (3.17) and (3.18).

Table 3.10 E and τ_f values

σ_N (kPa)	E (MPa)	τ_f (MPa)
27.6	11.1	10.4
49.7	20.5	17.3
72.5	31.9	25.5
95.2	44.9	35.2

Once again, from these results the value of the initial elastic modulus for a normal pressure given in Table 3.7 are found using the Duncan and Chang (1970) procedure. Fig. 3.25 shows the fitted curve used for this purpose.

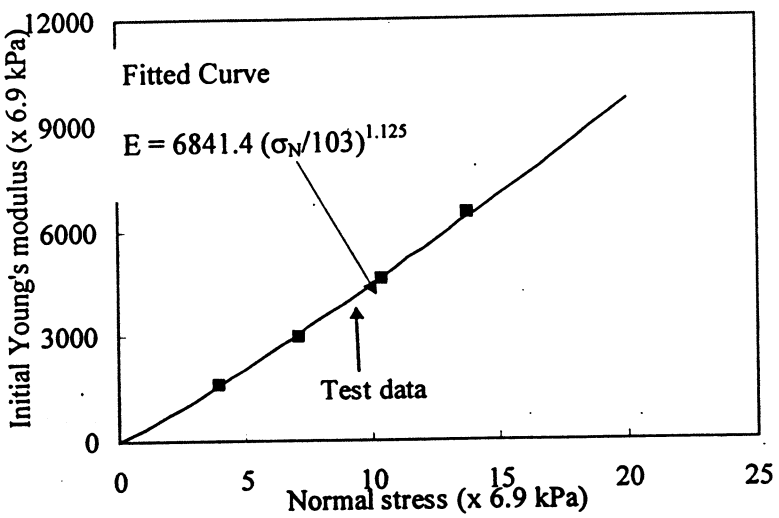

Figure 3.25 E versus σ_N

However, in the analysis, an intermediate modulus between the initial elastic modulus and that at failure was used. For this purpose, the value of E when τ is 50% of τ_f based on the following equation is used (Duncan and Chan 1970).

$$E_{50} = E_i\left(1-\frac{R_f}{FS}\right)^2 \tag{3.19}$$

where

R_f = failure ratio, taken as 1

FS = factor of safety under failure, taken as 2 for 50% of failure stress.

Table 3.11 Interface element stiffness

Pile	E_{50} (MPa)
UD_1	13.6
UP_{11}	11.5
UP_{12}	3.6
UP_{13}	2.2

The interface element stiffness are given on Table 3.11. Even for interface elements, 8-node solid three-dimensional "brick" elements were used. These elements of 0.1″ thickness were placed all around the pile elements along the entire length of the pile to separate the pile perimeter nodes from adjacent soil nodes.

The element stiffness E_{50} is used for interface elements parallel to the direction of lateral slippage. However, the interface elements in front and back of the pile were assumed to behave like elements of a very soft material, in order to facilitate separation in the active state. Hence a very small stiffness was used in the front and back as provided in Table 3.12 (E_C).

Table 3.12 Interface element stiffness (soft material)

Pile	E_C (MPa)
UD_1	1.03
UP_{11}	0.69
UP_{12}	0.52
UP_{13}	0.48

3.3.4 The Finite Element Mesh

Since the region of interest is limited to a few diameters around the pile, an octagonal mesh whose axis coincides with the axis of the model pile was considered as the most efficient modeling approach. In addition, the use of symmetry reduces the size of the model to a half-octagonal mesh, as shown in Fig. 3.26.

It was found from the literature as well as from trials involving different mesh sizes that placing the bottom of the model at a distance of 0.6 to 0.7 times the pile length from the pile tip provides sufficient accuracy. Similarly, the lateral boundary is placed at a distance equal to 0.6 times the pile length from the pile axis. The other boundary conditions imposed on the mesh are (1) the nodes belonging to the periphery of the octagonal mesh are fixed against displacement in both horizontal directions, with freedom to move vertically and (2) the nodes constituting the bottom of the mesh and the pile tip are fixed against displacement in all directions. Further, nodes lying on the axis of symmetry are restrained from displacing normally to that axis.

3.3.5 Stages in the Finite Element Analysis

In the first stage, the computed initial stress from expanding cavity theory are brought into equilibrium. Next, the static test is modeled by applying a lateral load at the pile top; the time period in which this load is applied is long enough so that dynamic effects are minimized. The mesh subdivision is believed to be sufficiently fine to

reproduce effectively the characteristics of the problem. Limitation of available CPU computer time makes it impractical to attempt a finer subdivision.

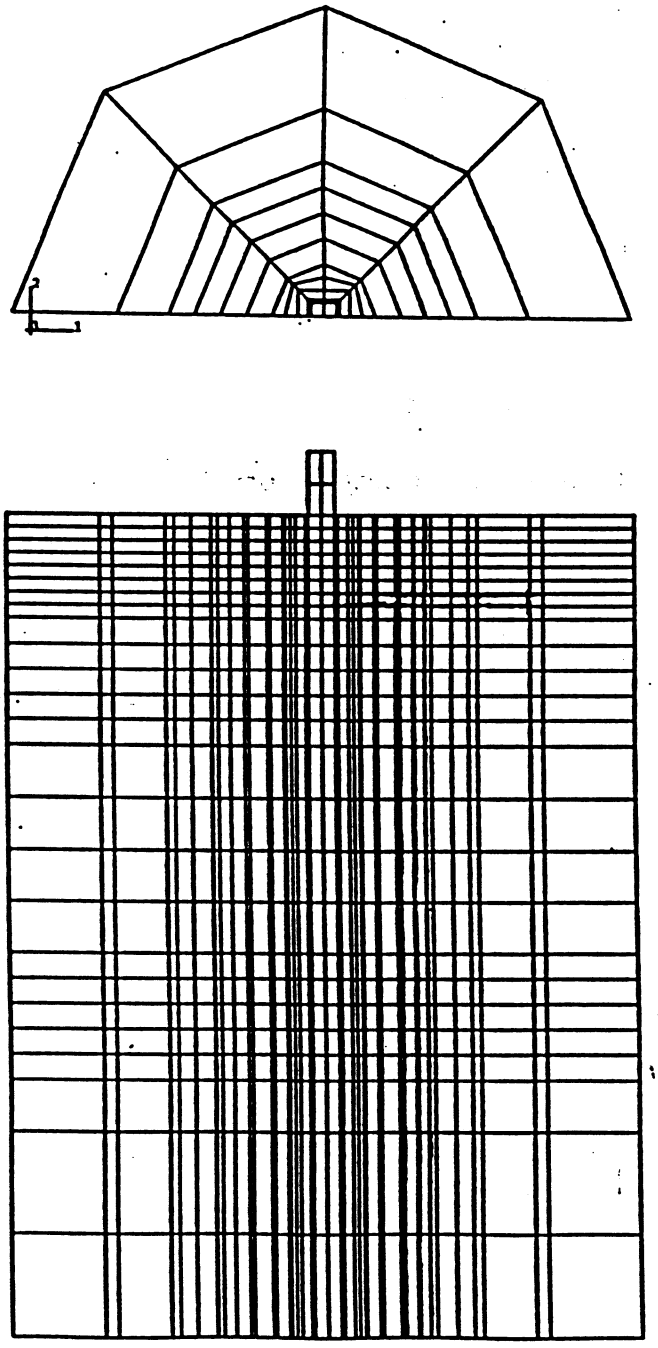

Figure 3.26 Finite element mesh (plan and elevation)

3.3.6 Numerical Results

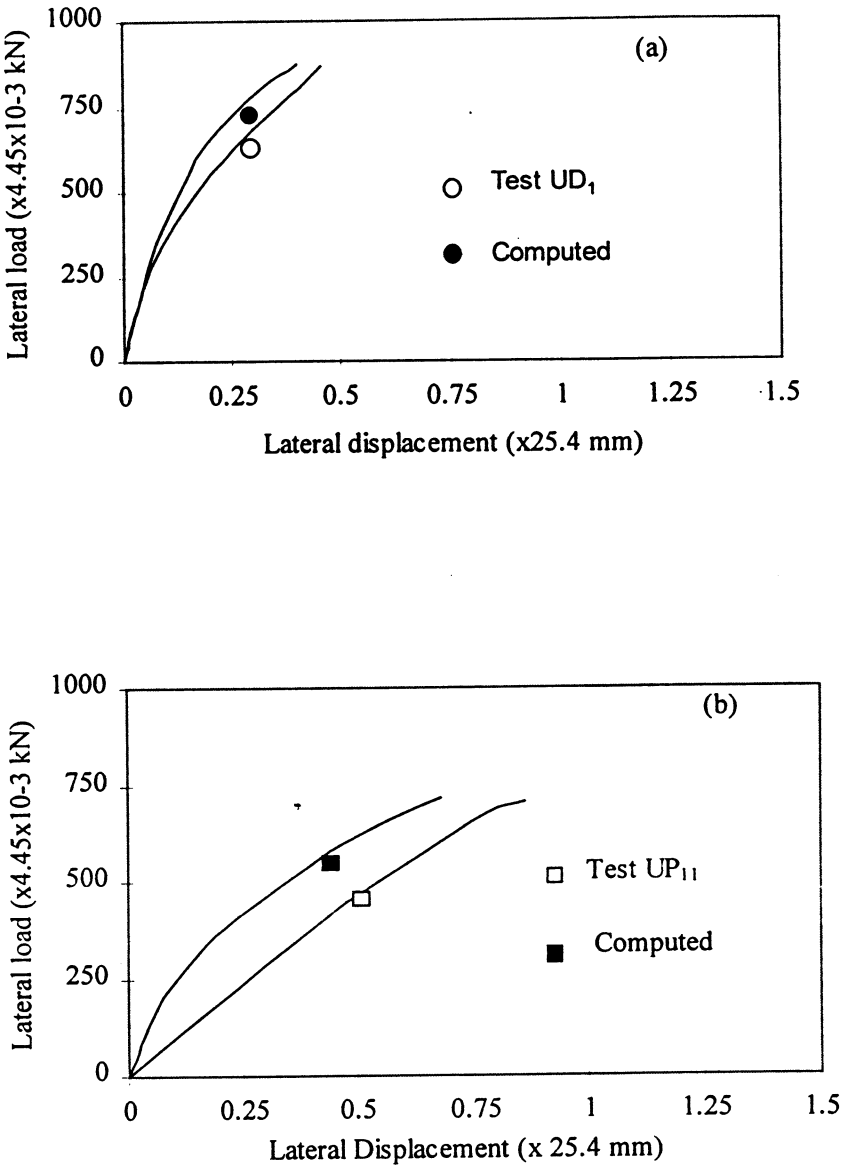

Figure 3.27 Computed lateral load-displacement curve

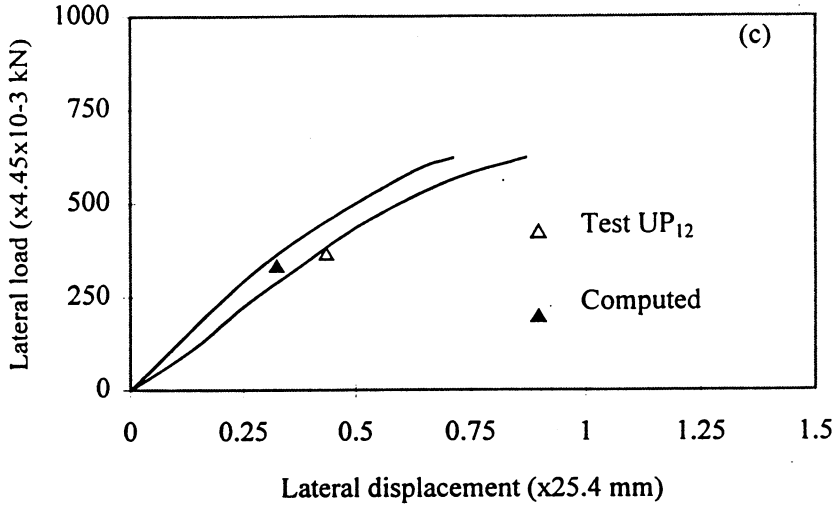

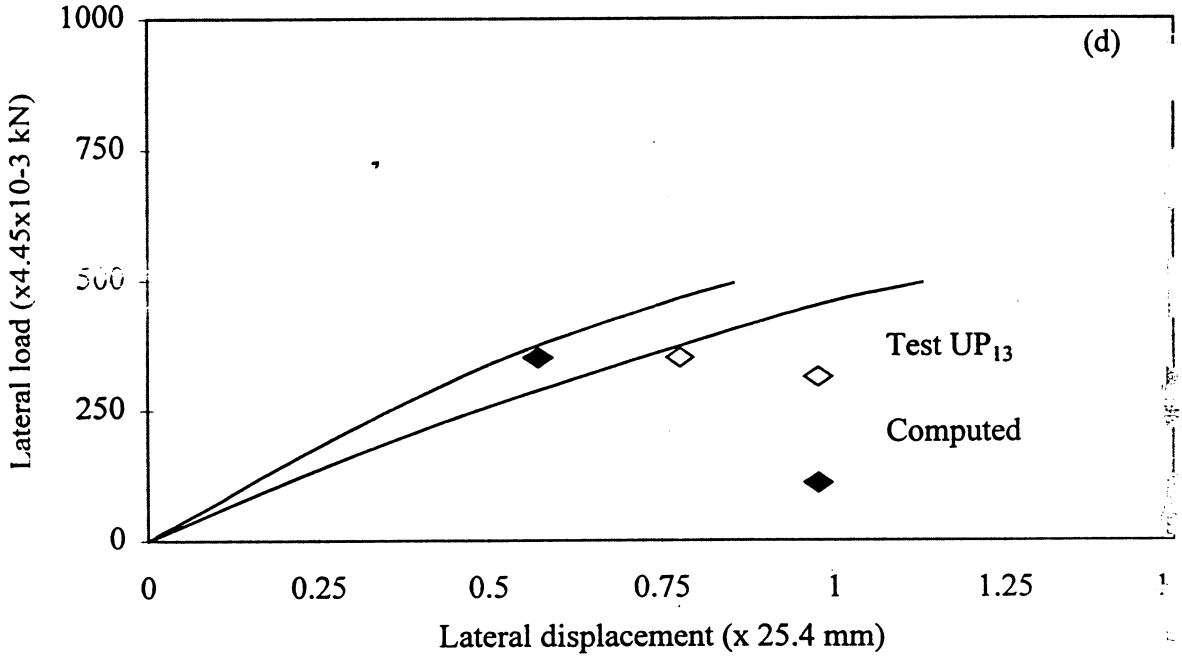

Figure 3.27 (Continued)

Figs. 3.27 (a) – (d) present lateral load-lateral displacement curves for the pile top obtained from the static finite element analysis for UD_1, UP_{11}, UP_{12} and UP_{13}. It can be observed that the experimental and computed curves are in reasonable agreement.

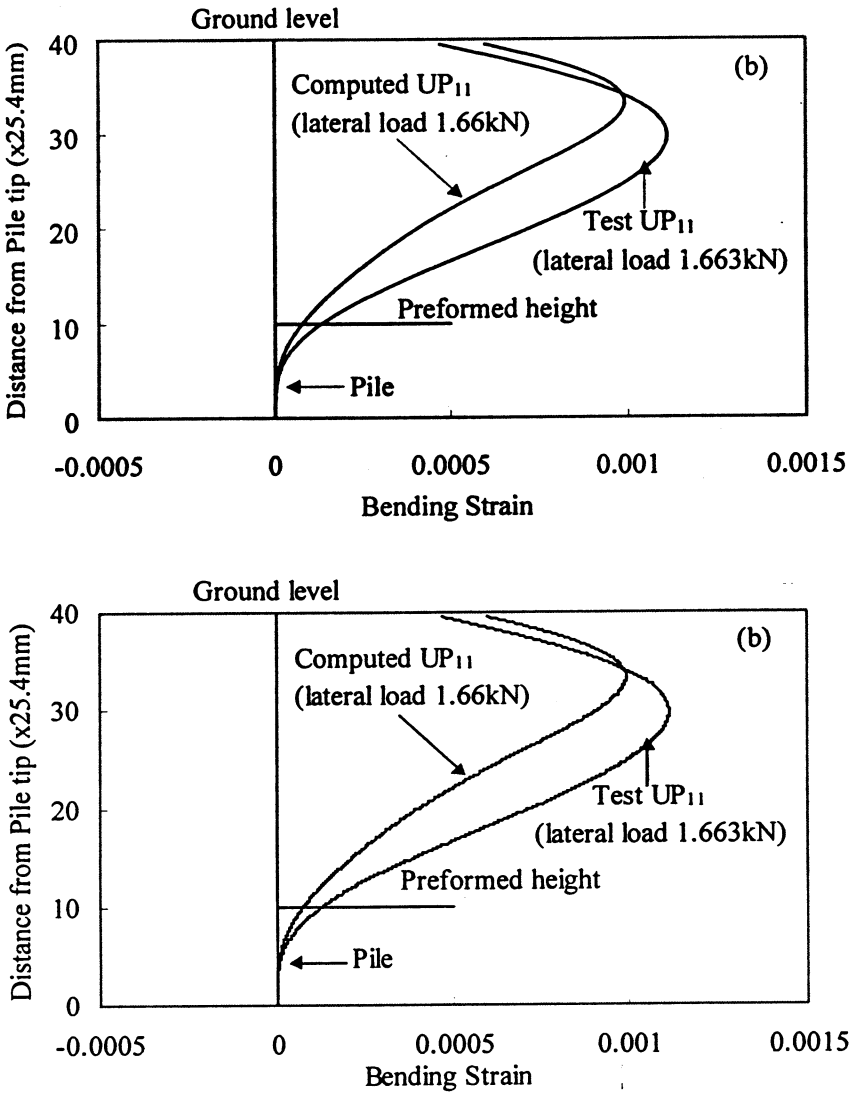

Figure 3.28 Distribution of strain

In addition, Figs. 3.28 (a) and (b) show the measured and computed bending strains for tests UD_1 and UP_{11}. It can be seen that measured and computed general trends

are similar. One reason for the difference between measured and computed results may be the fact that in actual tests the pile is hollow as compared to the solid pile used for the numerical simulation.

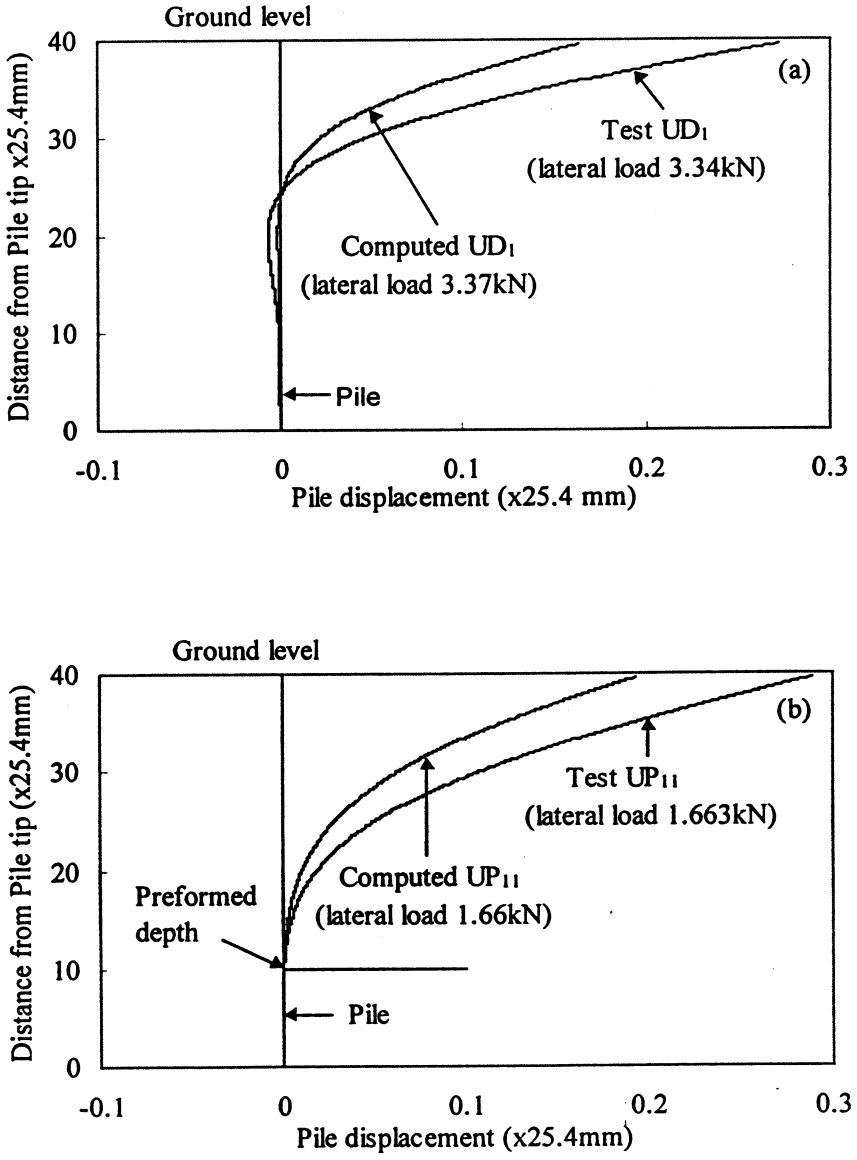

Figure 3.29 Pile lateral displacement

Measured and computed pile displacement is shown in Fig. 3.29. Finally, a vertical cross-section of the deformed three-dimensional finite element mesh associated with a 500 lbf lateral load is shown in Fig. 3.30. It is clearly seen that the use of very soft cushion like interface elements closely models the soil/pile separation. It must be noted that the deflected shape in Fig. 3.30 should be only used for relative comparisons, since a large magnification factor (75) is used to depict displacements.

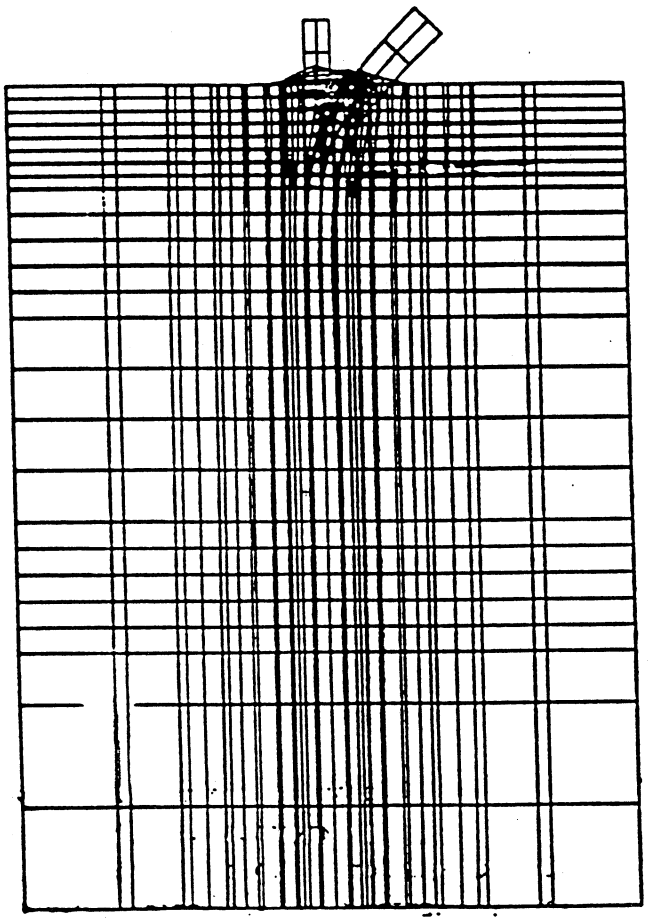

Figure 3.30 Deflected pile shape with pile-soil separation.

3.4 Conclusions

The lateral monotonic loading behavior of vertical, free-headed piles installed by preforming was presented based on model testing and computational studies. These studies were specifically focused on the soil-pile load transfer behavior in terms of p-y curves, under different installation procedures (driving, preforming). Based on this study, the following conclusions can be drawn.

Piles driven in a clayey sand clearly exhibit a higher lateral load capacity than the preformed ones. However, preforming is seen to significantly increase the lateral deflection at failure.

An increase in the preformed hole diameter increases the lateral deflection and noticeably reduces the maximum lateral load. This is due to the extensive ground disturbance associated with preforming which causes softening of the surrounding soil.

The experimental p-y relationships are nonlinear, being softer at shallow depths and stiffer at larger depths. The stiffness of p-y curves of preformed piles were considerably lower than those of the corresponding driven piles. Again this can be attributed to the soil disturbance surrounding the preformed pile.

The experimental comparisons in Table 3.4 as well as Eqns. (3.3) and (3.4) can be used as approximate guidelines to develop potential p-y curves for *preformed* piles when the p-y curves for a *driven* pile are available for the same soil in terms of experimental data or commonplace empirical methods.

An analytical procedure that can approximately model the lateral load behavior of preformed piles was developed based on the finite element method. The relevant

(5) An analytical procedure that can approximately model the lateral load behavior of preformed piles was developed based on the finite element method. The relevant techniques used to model the constitutive behavior of the pile material, foundation medium soil and the soil/pile interface mechanism produced reasonably satisfactory results compared to experimental observations.

CHAPTER 4

INVESTIGATION OF THE JETTING INFLUENCE ZONE

4.1 Introduction

Piles are generally installed in group at a spacing ranging from three to four times the dimension the pile. It is known that the behavior of piles in a group situation is somewhat different than that of a single pile especially if the piles are friction piles. Even the response of a laterally loaded pile group differs from that of a single pile because of the overlapping of the zones of influence of the adjacent piles (Prakash, 1990), as shown in Fig. 4.1

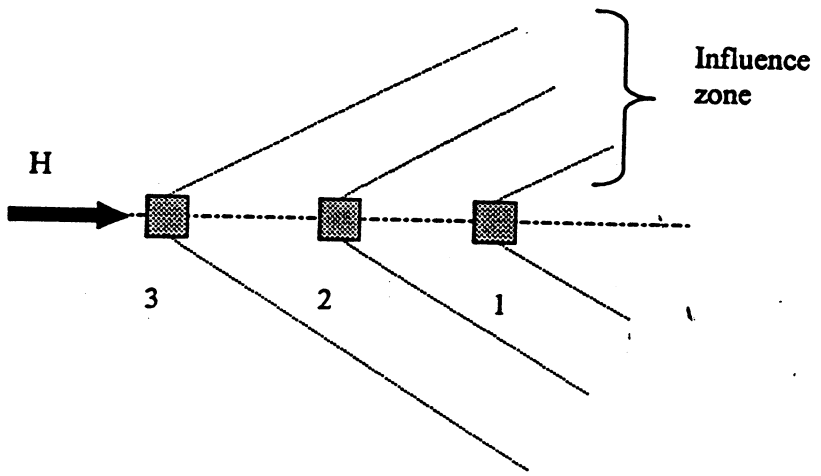

Figure 4.1 Overlapping of influence zones of a pile group

Fig. 4.1 shows a plan of a pile group laterally loaded at the ground level by a load H. The dotted lines in Fig. 4.1 indicates schematically how one pile in a group may affect its neighbors. The leading pile (pile 1) stresses the soil outside of the pile group, while the trailing piles (piles 2 and 3) generally stress the soil immediately in front of the leading piles. Hence if one of the leading piles is jetted, obviously there will be a reduction in the stiffness of the trailing piles.

Structurally intact bridges in the state of Florida are regularly widened to meet the increasing traffic demand. Currently, jetting is utilized to install the additional piles required to support the expanded bridges. During construction, the safe zone of jetting is determined based on subjective judgment. Thus, the primary objective of this final phase of the study is to determined, experimentally, the effect of adjacent pile jetting on existing driven pile behavior.

4.2 Experimental Details

An experimental program was setup to test a 13.4 kN/m^3 unit weight (loose) soil under both unsaturated and saturated conditions. In the first set of experiments, both the existing (driven) and jetted pile tip elevations were setup to be the same. In the second set of tests, the driven pile (short pile) tip elevation is set 0.254 m (10 inches) above the jetted pile tip elevation. The jetting effects on the existing driven piles were investigated under spacings of 3D and 5D (pile center to center spacing). Model piles used in this study were identical to the ones described in Chapters 2 and 3. Fig. 4.2 shows the

elevation of the pile arrangement in this experimental program. The entire testing program and corresponding test model pile abbreviations are shown in Table 4.1.

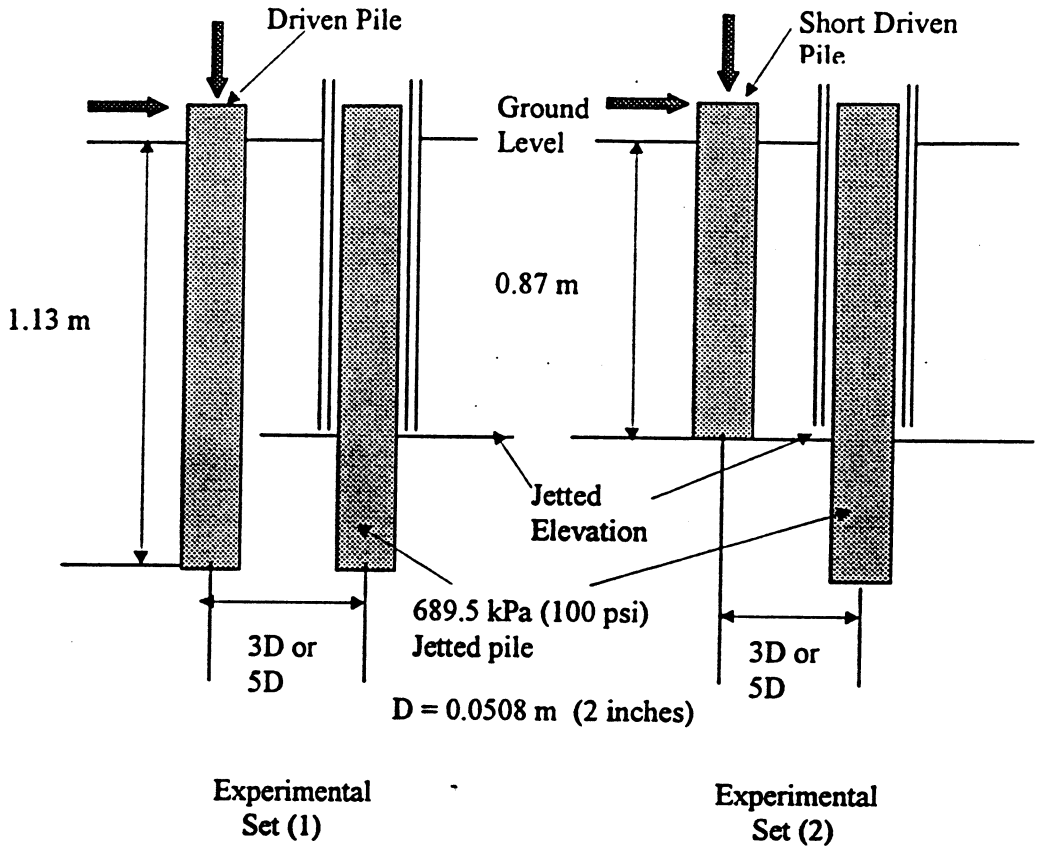

Figure 4.2 Model pile test setup

Table 4.1 Nomenclature used for piles in the testing program

Condition	Isolated Driven Pile	1.13 m Long Pile		0.87 m Long Pile	
		Spacing		Spacing	
		3D	5D	3D	5D
Unsaturated	IUD_1	LUD_{3D}	LUD_{5D}	SUD_{3D}	SUD_{5D}
Saturated	ISD_1	LSD_{3D}	LSD_{5D}	SSD_{3D}	SSD_{5D}

First, a 1.17 m (46 inches) long model pile was driven to a tip elevation of 1.13 m (44.25 inches), and a dead load of 250 lbf was applied while noting the settlement due to the applied load. Then, a second pile was jetted using a 689.5 kPa (100 psi) jetting pressure at a required spacing (3D or 5D). Figs. 4.3 (a) and (b) illustrate this maneuver.

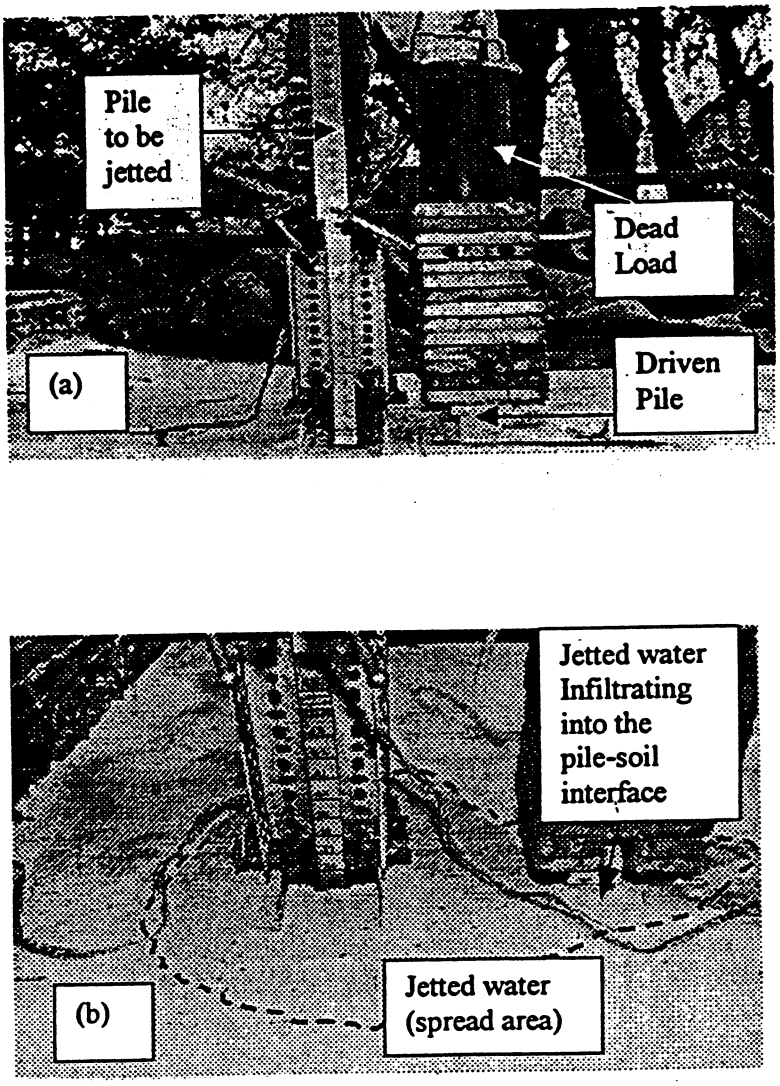

Figure 4.3 Jetting at a pile adjacent to an axially loaded driven pile

After jetting the second pile, the existing (driven) pile's ground level was inspected to ascertain that there was no settlement or tilting due to adjacent pile jetting. In all of the tests (Table 4.1) jetting was carried in the plane of lateral loading. Two isolated piles, a dummy driven pile with a test driven pile (IUD_1, ISD_1) was employed as a control experiment. Fig. 4.4 shows this control test setup (unsaturated condition).

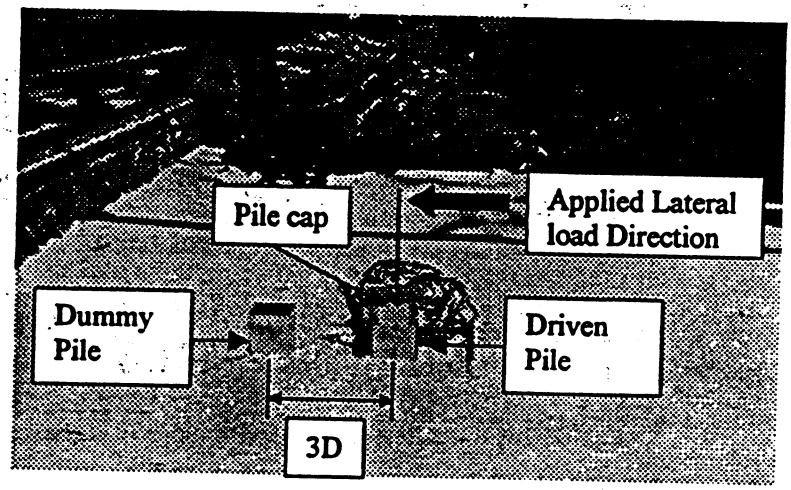

Figure 4.4 Isolated driven pile arrangement

Axial and lateral load tests were conducted within 3 to 4 hours after installation to minimize the effects of installation . Further, the piles were axially tested only upto an axial displacement of 0.013m (0.5 inches) and laterally tested only until a lateral displacement of 0.0254m (1 inch) was measured at the pile cap, thus ensuring that the piles did not fail either in axial loading or lateral loading. The same experimental procedures and mechanisms described in Chapters 2 and 3 were utilized at this stage as well to record and compute the displacements and strains. In all of the tests as identified in Table 4.1, the existing long and short driven piles were laterally loaded towards the

jetted pile. Fig. 4.5 shows the axial load test arrangement with a pile jetted at a 3D spacing.

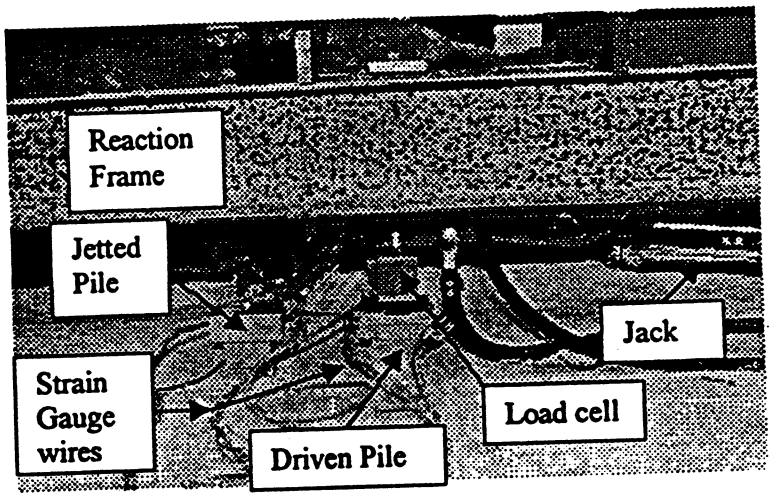

Figure 4.5 Axial load setup

4.2.1 Axial Load Test Results

Table 4.2 shows the axial load, at 0.013 m (0.5 inches) axial displacements, for different testing conditions employed.

Table 4.2 Influence of driven pile spacing on axial capacities

Test (Long Pile)	Axial load (kN)	Test (Short Pile)	Axial load (kN)
IUD_1	4.0		
LUD_{3D}	3.0	SUD_{3D}	3.6
LUD_{5D}	2.32	SUD_{5D}	3.0
ISD_1	1.83		
LSD_{3D}	1.78	SSD_{3D}	1.8
LSD_{5D}	1.80	SSD_{5D}	2.0

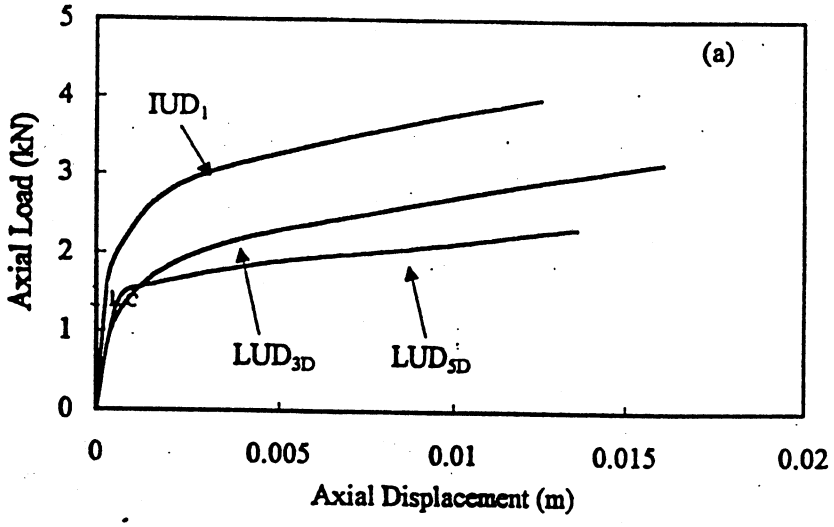

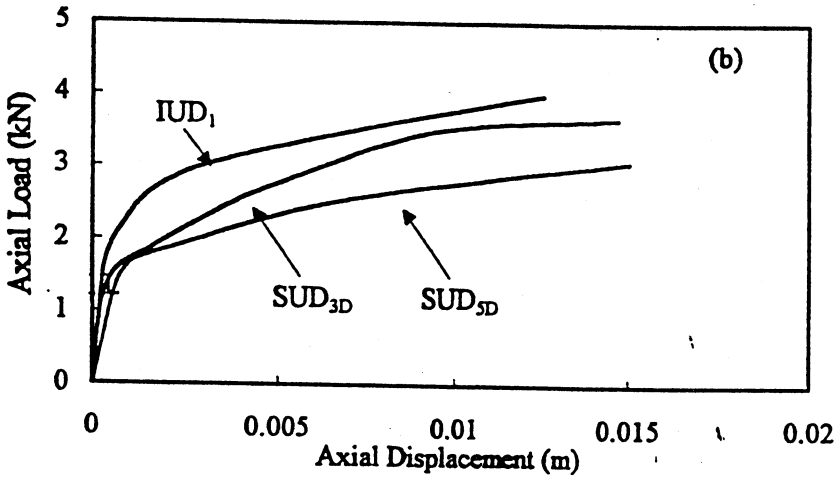

Figure 4.6 Axial load test results (unsaturated)

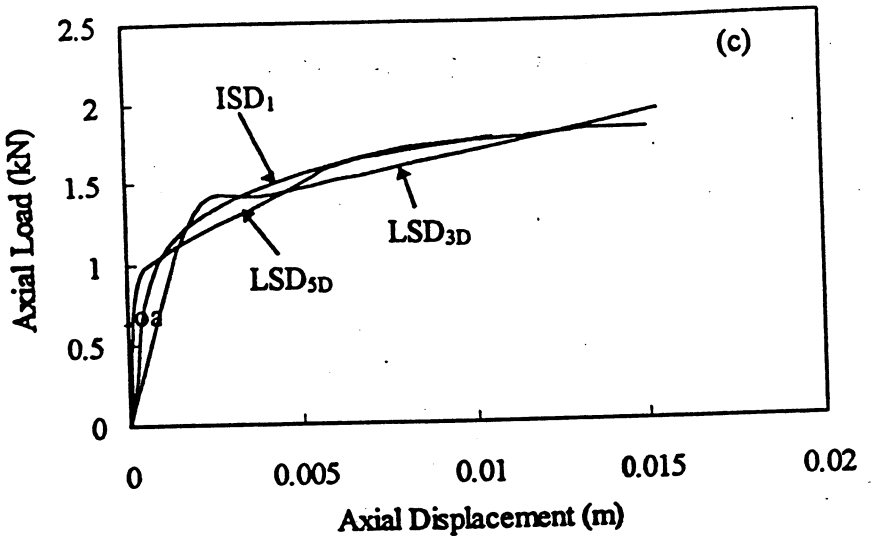

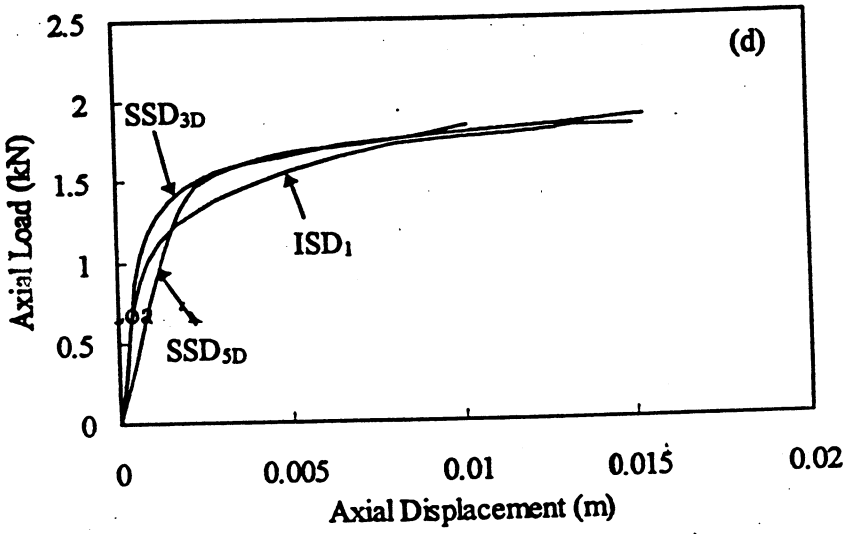

Figure 4.6 Axial load test results (saturated)

Axial load vs displacement curves for the unsaturated and saturated condition are given in Figs. 4.6 (a) - (d). As expected, the isolated pile (IUD_1) shows stiffer behavior than other piles. When the axial loading characteristics of driven piles with jetting in the vicinity (3D and 5D) were compared, the driven piles (both long and short) with jetting at 3D shows stiffer behavior than that under 5D spacing, in the unsaturated condition. This is probably because the effects of densification due to final driving of the jetted piles have overridden the effects of jetting. For saturated conditions, it was observed that jetting does not effect the adjacent driven pile axial load behavior.

4.2.1.1 Unit Load-Transfer Characteristics

Relationships between unit load transfer (unit shaft resistance, f, and unit toe resistance, q) to local pile deflection, w, are useful in visually interpreting the manner in which load transfer develops in both shaft friction and bearing. In order to develop the unit load-transfer relationship, the strain-distributions along the pile, which were determined for every test by using strain gauges along the length of the pile, must be known. Fig. 4.7 shows a representative strain-distribution relationship during the axial loading of isolated driven pile (IUD_1) for selected values of the applied axial load. The strain distribution data were fitted by an analytical expression of the form

$$\varepsilon(z) = C_0 + C_1 z + C_2 z^2 \qquad (4.1)$$

where

$\varepsilon(z)$ = strain distribution on the pile

C_i = constants, obtained from least-square fit i = 0,1,2

z = depth below the ground surface

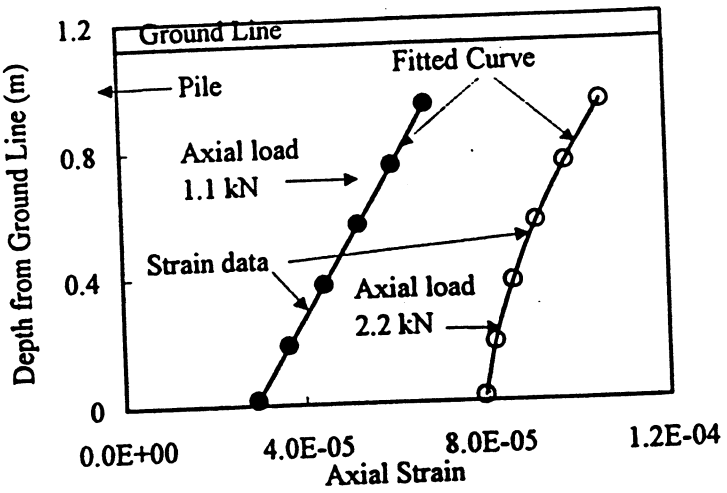

Figure 4.7 Strain distribution along the pile IUD_1

Unit load transfer f and q were then computed using the following elastic expressions:

$$f(z) = \frac{EA}{S}\left(\frac{d\varepsilon(z)}{dz}\right) \tag{4.2}$$

$$q = \frac{\varepsilon(z) \times EA}{A_e} \tag{4.3}$$

where

A = cross sectional area of the pile

A_e = effective bearing area

S = circumferential area of the pile

The corresponding w value is determined by using the following relationship

$$w = w_1 - \int \varepsilon(z)dz \tag{4.4}$$

where

w_1 = measured vertical displacement of the pile at the ground level

For the mid-section of the pile (approximately 0.42m) the above process was repeated for selected load levels to develop a set of points defining the f-w and q-w curves for unsaturated and saturated conditions as shown in Fig. 4.8 (a) - (h).

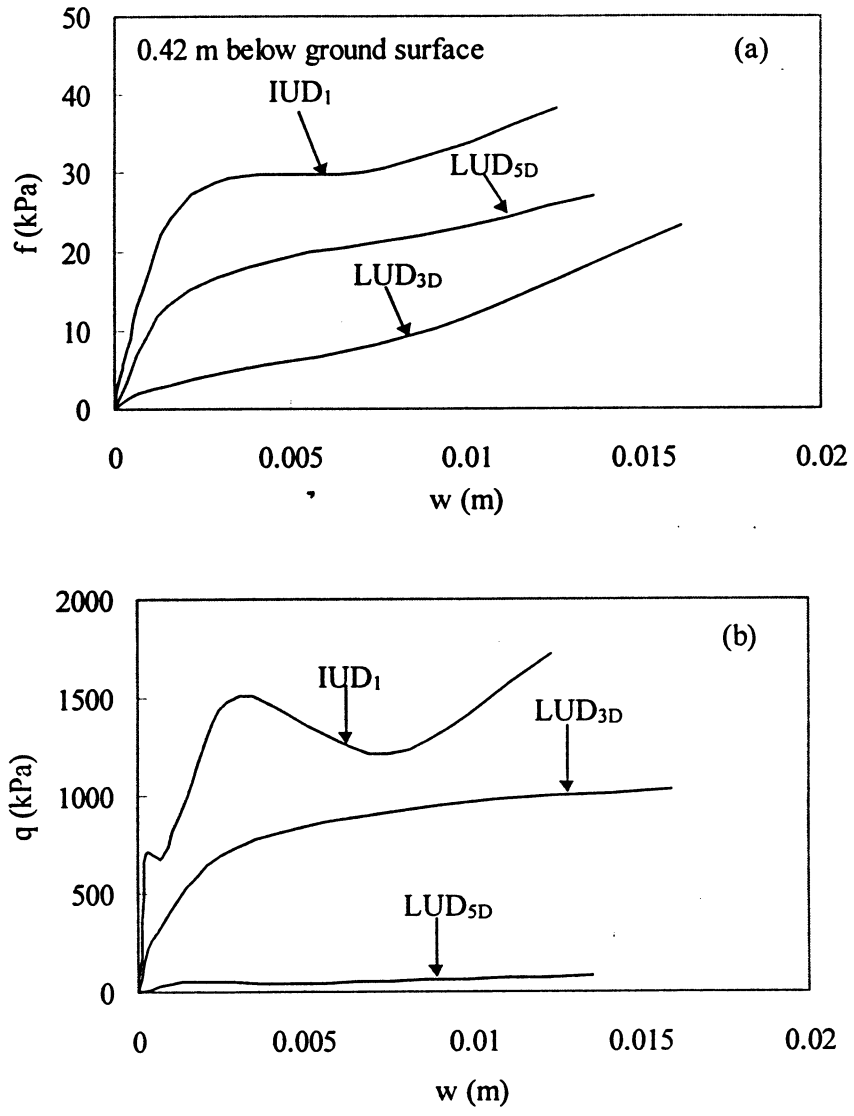

Figure 4.8 f-w and q-w for long pile (unsaturated condition)

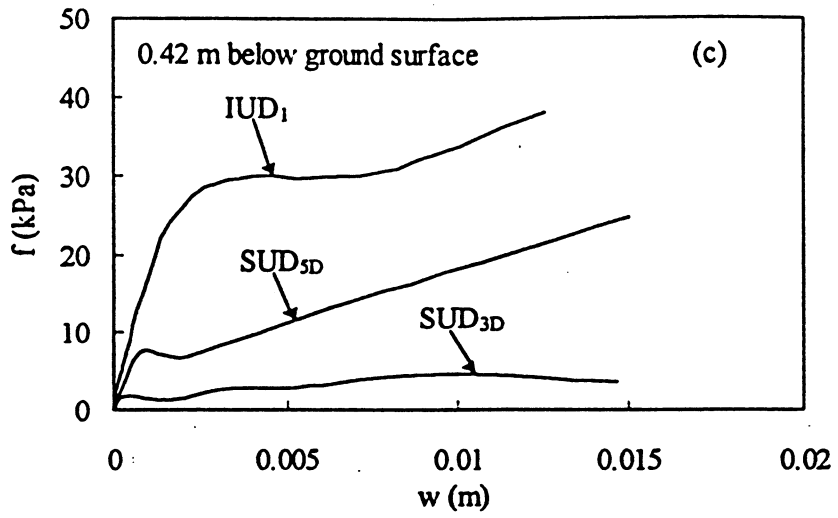

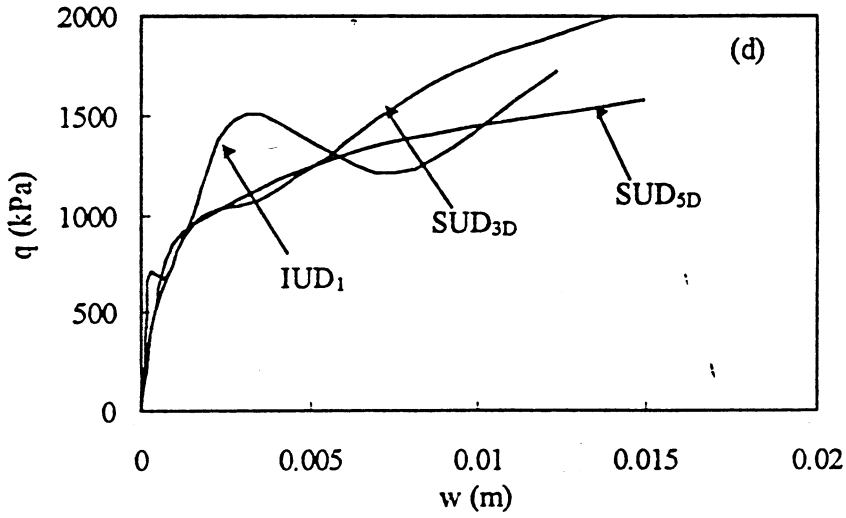

Figure 4.8 f-w and q-w for short pile (unsaturated condition)

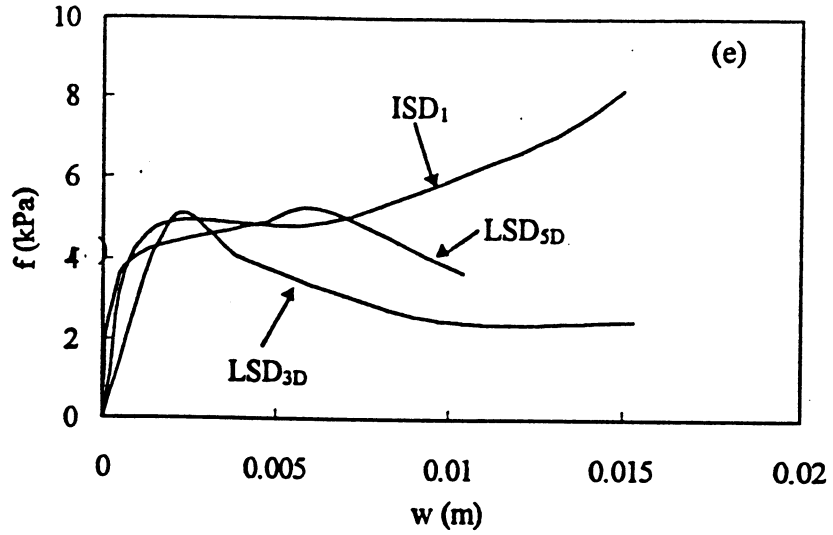

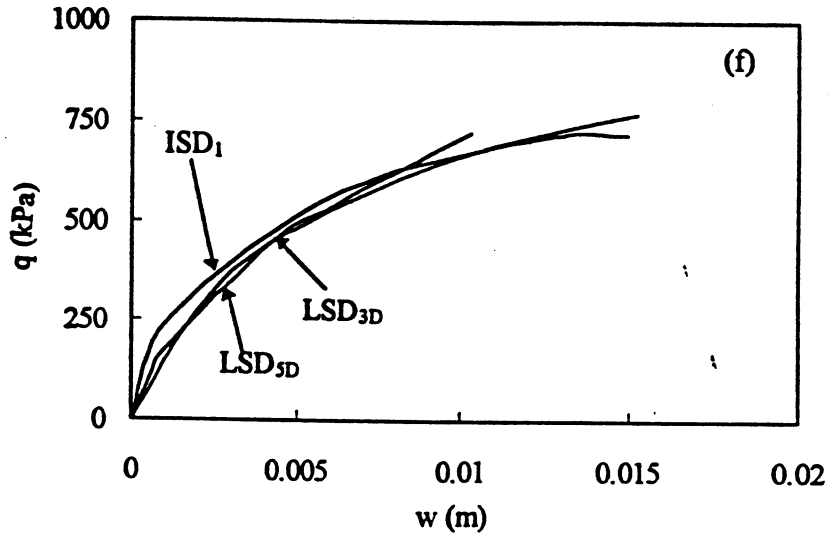

Figure 4.8 f-w and q-w for long pile (saturated condition)

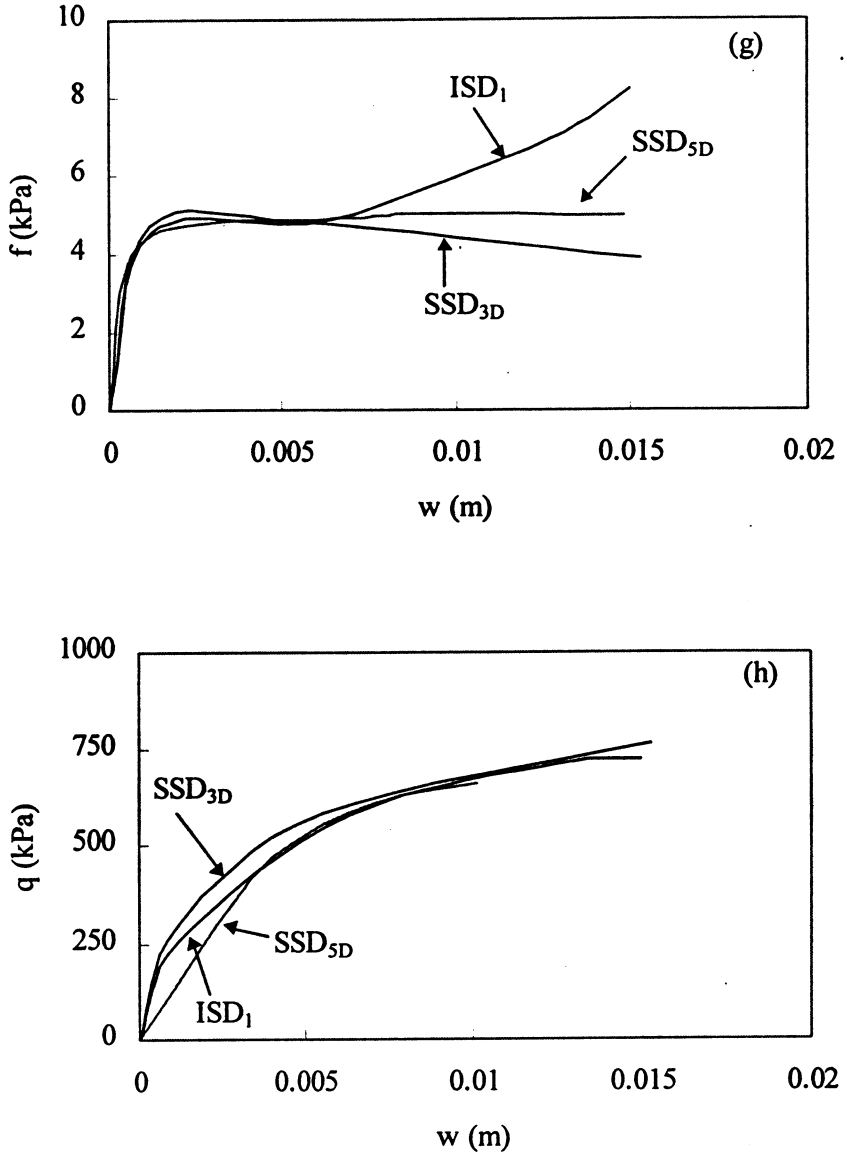

Figure 4.8 f-w and q-w for short pile (saturated condition)

Several observations are made on the axial load transfer relationships: (1) the ultimate unit toe resistance (Fig 4.8 (b) and (c)) is the highest for the driven pile next to a control driven pile compared to ones next to jetted piles; and the driven pile with jetting at a 3D spacing shows a higher toe resistance than that with jetting at 5D spacing, which

may due to the densification of soil near the toe, (2) the developed f value is larger for IUD_1 than for other driven piles since insertion of the control driven pile produces a significant increase in the horizontal effective stress near the model pile-soil interface, (3) driven piles with jetting at 5D spacing shows higher developed f value than that at 3D spacing probably due to the significant jetting effects at 3D.

4.2.2 Lateral Load Test Results

Table 4.3 shows the lateral load test results of the long and short piles at 0.0254 m (1 inches) lateral displacement under unsaturated and saturated conditions.

Table 4.3 Influence of driven pile spacing on lateral capacities

Test (Long Pile)	Lateral Load (kN)	Test (Short Pile)	Lateral Load (kN)
IUD_1	3.45		
LUD_{3D}	2.38	SUD_{3D}	2.0
LUD_{5D}	2.87	SUD_{5D}	2.34
ISD_1	3.1		
LSD_{3D}	2.7	SSD_{3D}	2.1
LSD_{5D}	3.0	SSD_{5D}	2.26

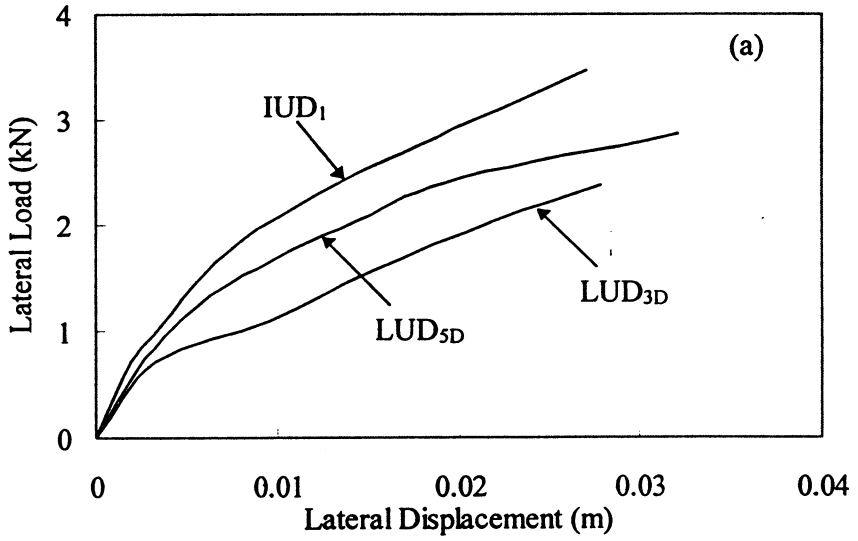

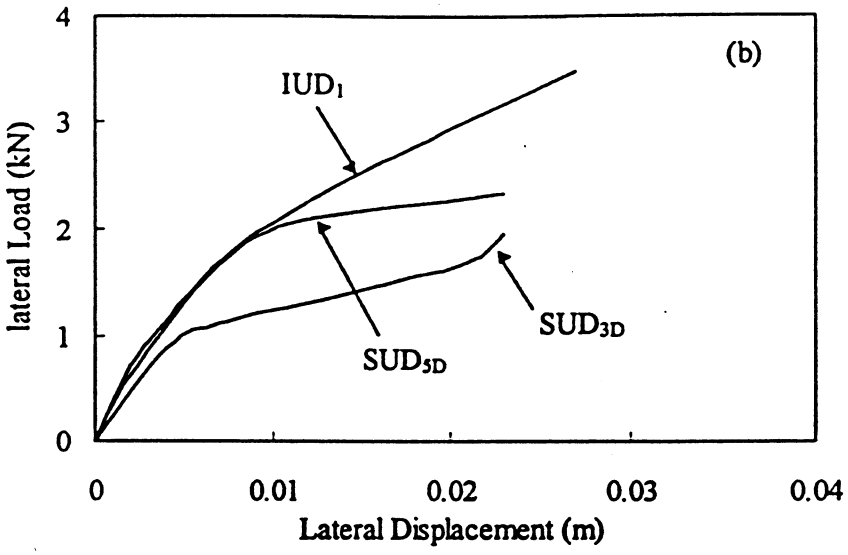

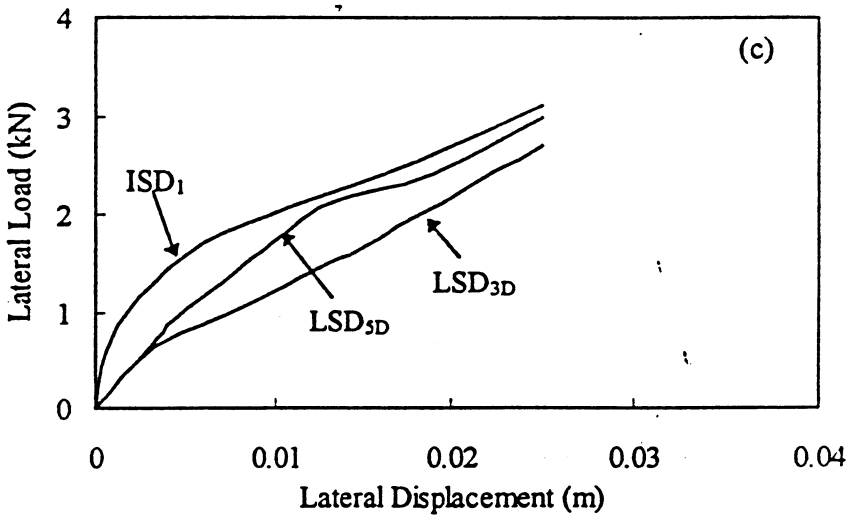

Figure 4.9 Lateral load and lateral displacement

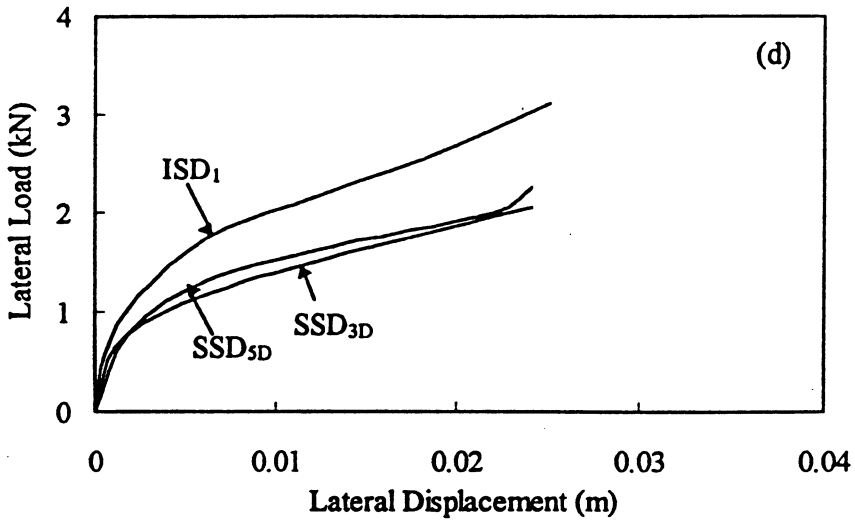

Figure 4.9 (Continued)

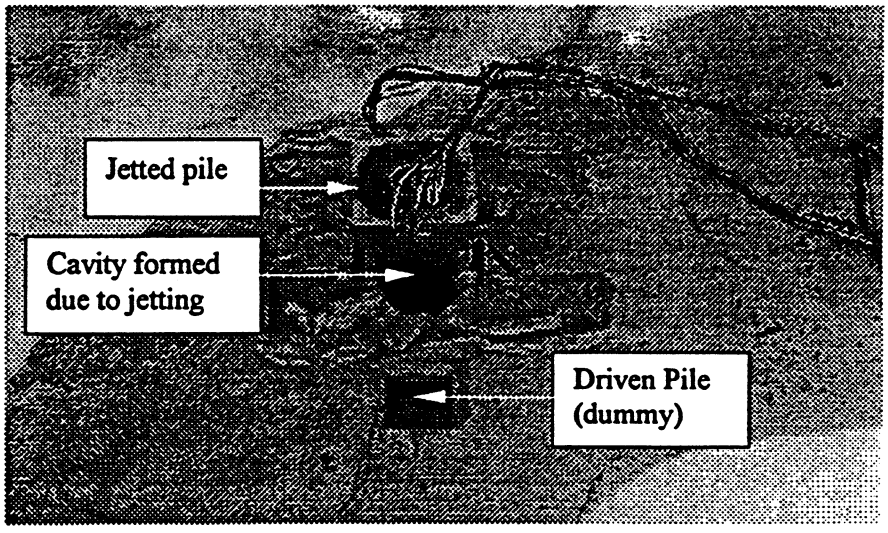

Figure 4.10 Cavity due to jetting

Fig. 4.9 (a) - (d) show the lateral load vs lateral displacement curves upto a 0.0254 m (1 inch) displacement above the ground level for unsaturated and saturated conditions. It can be seen that the lateral load capacity increases with increasing spacing. This is mainly due to reduction in the horizontal confining stress due to the cavity formed by jetting as shown in Fig. 4.10. Accordingly, as far as lateral load capacity is concerned, a spacing of 5D seems to be out of the influence zone.

4.2.2.1 Lateral Load-Transfer Characteristics

The non-linear lateral load transfer characteristics (p-y curves) were obtained for each test by same procedure described in Chapter 2 and 3. Figs. 4.11 (a), (b), (e) and (f) shows the p-y curves for the long pile while Figs. 4.11 (c), (d), (g) and (h) show the p-y curves for short pile under unsaturated and saturated conditions.

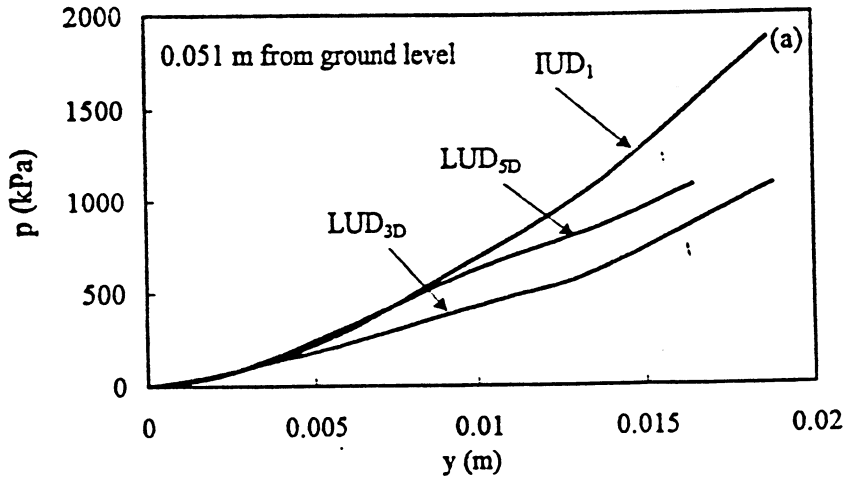

Figure 4.11 (a) p-y curve for long pile (unsaturated condition)

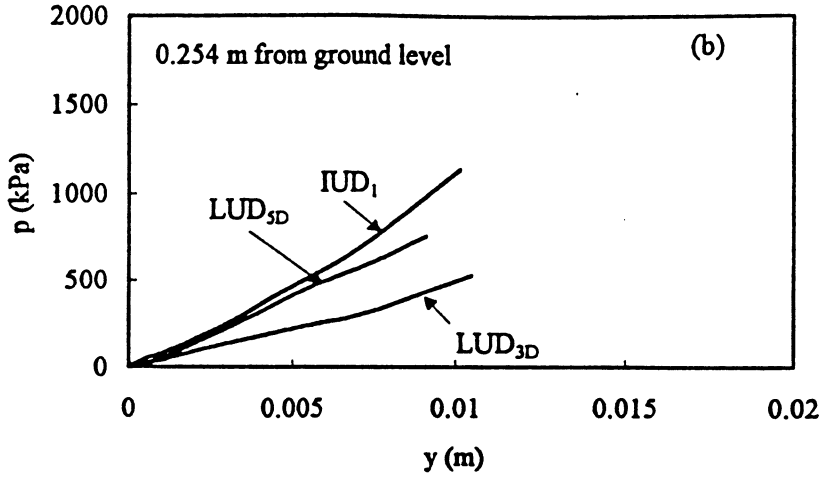

Figure 4.11 (b) (long pile, continued)

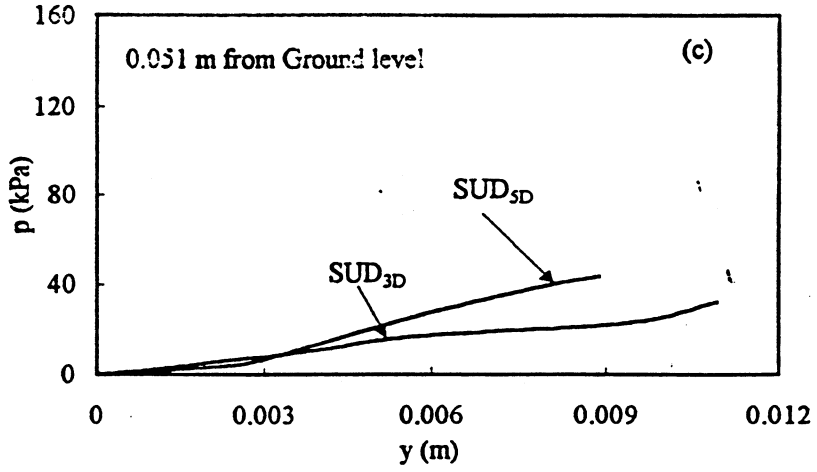

Figure 4.11 (c) p-y curve for short pile (unsaturated condition)

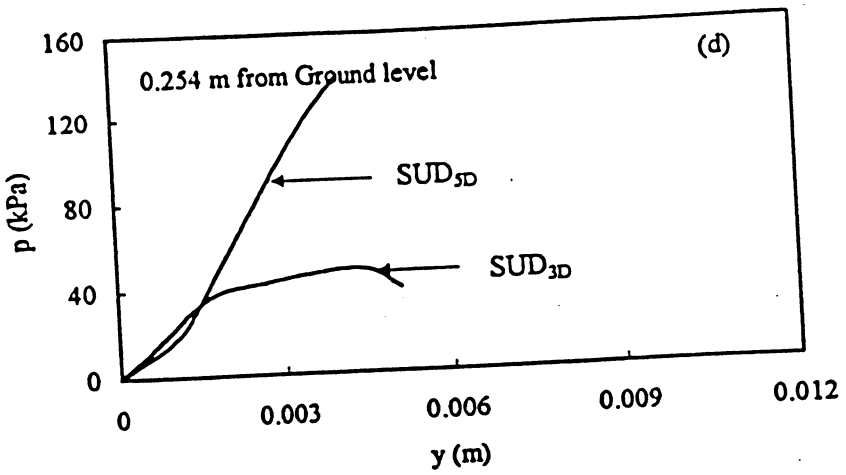

Figure 4.11 (d) (short pile, continued)

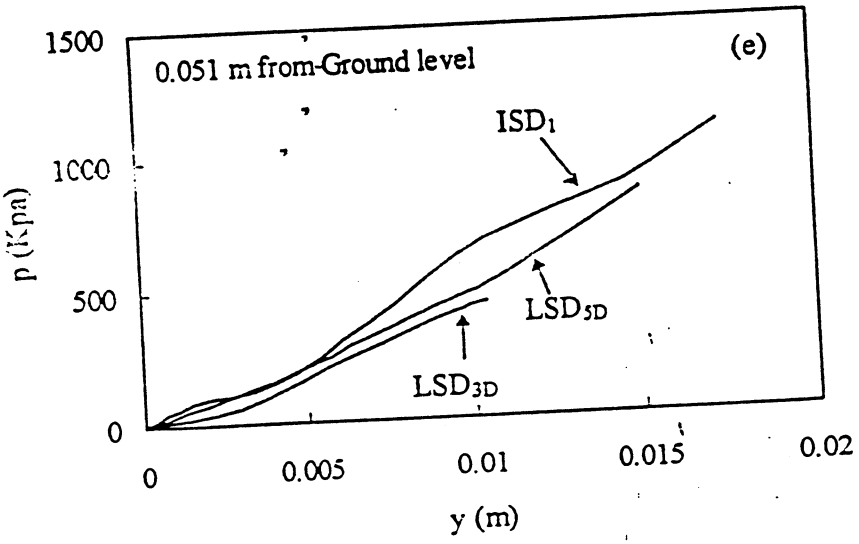

Figure 4.11 (e) p-y curve for long pile (saturated condition)

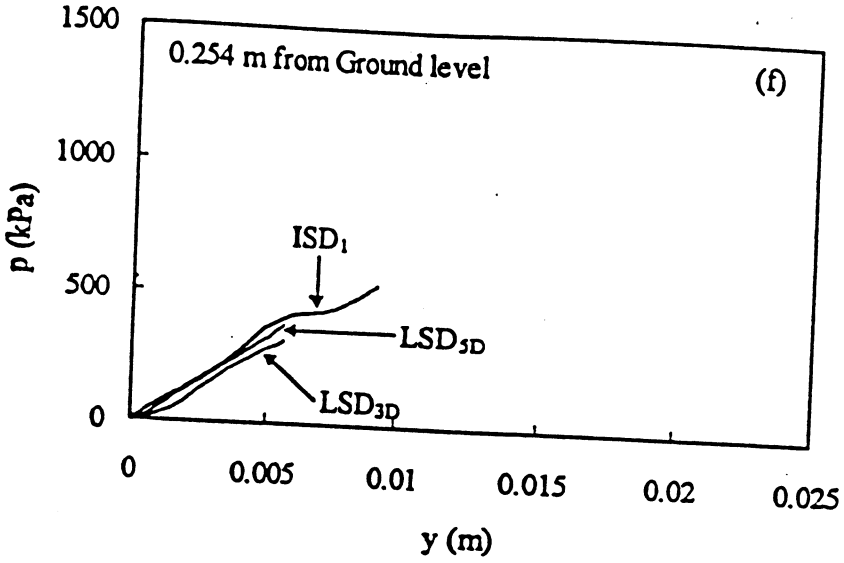

Figure 4.11 (f) (long pile, continued)

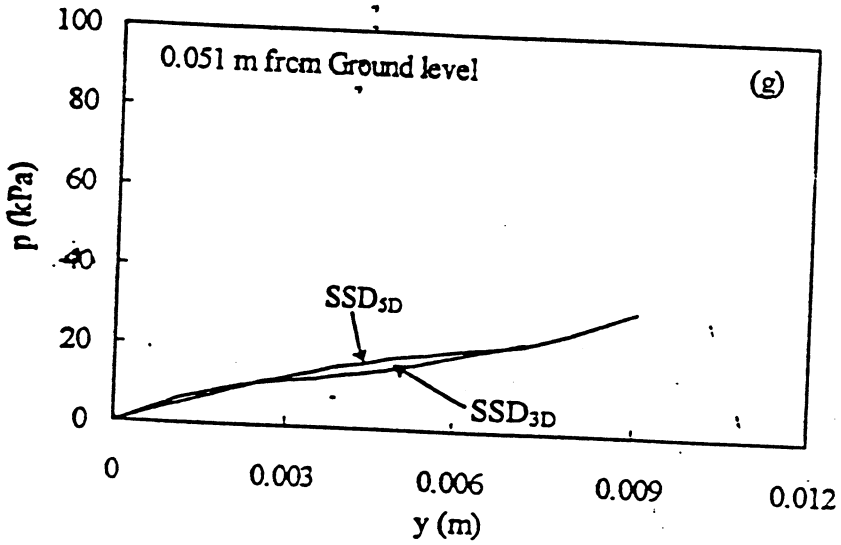

Figure 4.11 (g) p-y curve for short pile (saturated condition)

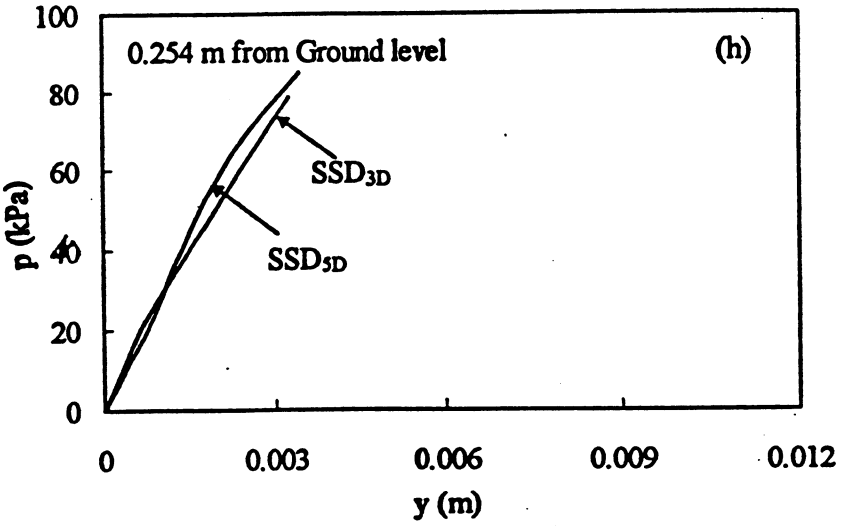

Figure 4.11 (h) (short pile, continued)

Fig. 4.11 (a) – (h) show the p-y curves at 0.051 m and 0.254 m depths below the ground level. It can be seen under unsaturated condition that the long driven piles exhibits stiffer lateral load characteristics compared to the short piles. The piles with jetting at 5D spacing shows higher lateral load transfer characteristics than that with jetting at 3D spacing. Further under saturated condition long and short pile shows the almost same p-y characteristics. However when jetting is done at 3D and 5D spacing (both long and short piles), changes in lateral load transfer characteristics of existing pile are not very significant when compared to those of the axial load transfer characteristics.

4.3. Finite Element Model

The behavior of piles was simulated using axisymmetric idealization in which there is symmetry around a central vertical axis. This axis is taken through the center of the pile. As the analysis involves modeling of fluid flow through soil and the analysis using effective stresses, the analyses were performed using composite type 8-noded axisymmetric elements for soil. These elements are defined with both displacements and pore pressure degrees of freedom (dofs) at the corner nodes and only the displacements are defined at the interior elements as shown in Figure 4.12. The elements representing the pile are modeled as ordinary 9-node element which does not have pore pressures as variables.

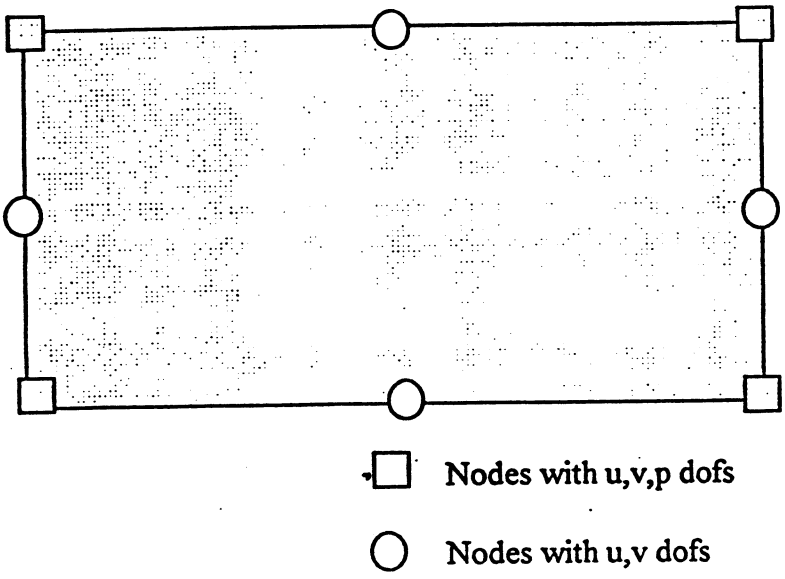

Fig. 4.12. 8-node composite type element used in the analyses

The nodes on the left side of the mesh are constrained from moving in the horizontal (radial) direction. The nodes on the base of the mesh are constrained in both horizontal and vertical directions. The nodes on the right side of the mesh are once again constrained from moving in the horizontal (radial) direction. The dimensions of the mesh were chosen to represent the laboratory test configuration used at the University of South Florida. The radius of the pile was taken as 0.29m (having equivalent plan area of a 2" square pile) and the length of the pile was taken as 0.76m (the actual length being 0.74m). The radial dimension of the mesh was taken as 0.53m (i.e. approximately 10 times the diameter of the pile) and the height of the mesh was taken as 1.3m.

The following soil properties were used in the analysis:

- coefficient of permeability of soil = 0.425 x 10^{-3} in/sec (1.08 x 10^{-3} cm/s)
- unit weight of the soil = 0.058 lb/in^3 (16.2 kN/m^3)
- degree of saturation = 100%
- specific gravity of soil solids = 2.68
- Young's modules of soil = 4354 lb/in^2 (30000 kPa)
- Poisson's ratio of soil = 0.3
- cohesive strength of soil (0.2 kPa ≈ 0)
- friction angle of the soil = 30°
- dilation angle of the soil = 0°

The constitutive behavior of the soil was simulated using the modified Drucker-Prager model with cap that limits the magnitude of hydrostatic compression stress. The β parameter in this model was obtained by matching the envelope of this model with the outer apices of the Mohr-Coulomb failure surface (for non-dilatant model) as $\tan\beta = \sqrt{3}\sin\phi$. Because of the no -dilatant mode., the resulting stiffness matrix will be unsymmetric. The equations were solved using the unsymmetric solution option in the ABAQUS.

4.3.1 Analysis for the Lateral Spread of Pore Pressure Due To Pile Jetting

In the first phase of the analysis, this problem was taken up. In the laboratory experiments, a water pressure of 690 kPa was used. The same was also used in these analyses. The extent of soil affected by the jetting was obtained by plotting the steady state pore pressure contours due to pile jetting. The finite element results give the pore pressures in the soil medium due to the imposition of pore pressures at the source location. The pore pressures around the pile (source location) were specified as boundary conditions in the program to get the solution. The solutions were obtained for three different assumed pore pressure variations as follows.

a. pore pressure specified at the pile tip only
b. pore pressures on equal magnitude specified at the nodes along the length of the pile
c. the specified pore pressures at the nodes along the length of the pile reduce linearly toward the surface.

In all the above cases, the magnitude of pore pressure used was 690 kPa. The pore pressure at the nodes corresponding to the surface of soil was set to zero. The solution was obtained by iteration

using the *SOILS* analysis option in the program. The steady state pore pressure contours from these analysis are shown in Figures A1-A3. The pore pressures are highest near the pile and gradually reduce as the distance from the pile increases. The pore pressures shown are the excess pressures beyond the hydrostatic pressure. There is a clear pattern of bulb shape of pore pressure distribution near the pile tip in all the cases. In the first case, the pore pressures reduce to 330 and 360 kPa, at a distance of about 1.5 times the diameter (D) and to less than275kPa at a distance of about 2.5 times the diameter from the pile edge. In the second case in which the pore pressure was assumed to be constant along the length of the pile (which is most unlikely to happed in the field), the pore pressure was constant at about 690 kPa, around the pile shaft for some distance. At a distance of about 5D, the pore pressure reduces to 50% of the jet pressure. In the 3rd case of analysis, the pore pressures have reduced to about 360kPa at a distance of 3D and to less than 345kPa at a distance of about 5D. These predicted zones of pore pressures are extremely conservative because of the axisymmetric idealization of a truly 3-dimensional problem.

From the results of these analysis, it could be said that at distance of about 3D from the edge of the pile, the pore pressures reduce to less than 50% of the jet pressure. This distance will very much depend on the coefficient of permeability of the soil. For example, when the coefficient of permeability of the soil was increased 10 times, the pore pressures were found to decrease to 50% value at about 2D from the edge of the pile.

4.3.2 Load Testing Of Piles

The analysis to study the influence of pile jetting on load capacity of piles was conducted in two stages. In the first stage of analysis, the pore pressures were specified at various distances from the pile edge and the distribution of pore pressures in the soil medium was obtained as described in the earlier section. For all these analysis, the pore pressures were assumed to decrease linearly towards the ground surface from a maximum at the pile tip. A solid rigid steel pile was assumed to be located at the center of the mesh and the pore pressures were specified at distances of 1D, 2D, 3D and 8D. The axisymmetric idealization of this problem implies that a large number of piles are jetted around the candidate pile which may be the worst case field situation.

In the second stage of analyses, equal displacements were specified on the nodes corresponding to the top of the pile and the stresses developed in the soil element below the pile was monitored. A typical deformation pattern of soil under the vertical loading of pile is shown in Figure A4. A typical variation of vertical stress (S_{22}) in the soil element below the pile and the pile head

movement is shown in Figure A5. When the pore pressures were specified at large distances, a maximum soil stress of about 375kPa was developed. When the pore pressures were specified at a distance of 1D, the solution diverged in the 1st increment itself indicating that the pile is not stable under these conditions. The collapse of pile may be assumed under this condition. When the pore pressures were specified at a distance of 2D, the maximum pressure reduced to about 325 kPa The variation of pressure with the pile head settlement for various cases are shown in Figure A6. It is clear that when the pore pressures are specified t distances of 3D or more from the edge, the effect on the soil stress is not very much. Hence, we may conclude that the vertical capacity of pile is not adversely affected if the jet is located at a distance of 3D or more. Similar conclusion was also arrived at based on the laboratory experiments at the University of South Florida. The finite element result may complement this experimental result.

4.4 Conclusions

Model pile tests and finite element analysis were conducted to identify the effects of pile jetting on adjacent driven piles. The test parameters considered were pile spacing and driven pile length. Based on this study, the following conclusions can be reached.

1. Under unsaturated soil conditions, the tip resistance of existing piles with jetting performed at 3D spacing is higher than that of piles with jetting performed at 5D spacing, probably because the densification due to final driving for firm seating predominates jetting effects. These effects tend to diminish with complete saturation.

2. Under unsaturated soil conditions, the shaft resistance of existing piles with jetting performed at 3D spacing is significantly lower than that of piles with jetting performed at 5D, probably due to the effects of jetting. These effects tend to diminish with complete saturation.

3. Higher lateral load capacities are obtained in existing piles when piles are jetted at 5D spacing than at 3D spacing obviously due to the reduction of the lateral confinement. Once again, these differences are insignificant under complete saturation conditions.

4. Finite Element analysis on the other hand indicates that, in completely saturated soils, the jet induced pore pressures reduce to less than 50% of the jet pressures at distances of 3D or more from the pile edge. Further, the axial load capacity of the piles with a water jet at a distance of 3D was found to be almost the same as that with a water jet at a large distance.

Hence, based on both approaches, a jetting influence zone of 5D would be a conservative assumption for unsaturated clayey sands while this could be considered as being less than3D under completely saturated conditions..

REFERENCES

ABAQUS (1995), Hibbitt, Karlsson & Sorensen, Inc., Version 5.5

Abendroth, R. E., and Lowel, F. G. (1990), "Pile Behavior Established from Model Test", *J. Geotechnical Engineering*, ASCE, Vol. 116, No. 4, pp. 571 - 578.

Bowles J. E., (1996), "Foundation Analysis and Design", 5th Edition, The Magraw - Hill Companies Inc., New York.

Broms, B., (1964), "Lateral Resistance of Pile in Cohesionless Soil", *J. Soil Mech. Found. Div.*, ASCE, Vol. 90, No. SM3, pp. 123 - 156.

Duncan, J. M., and Chin-Yung Chang, (1970), "Nonlinear Analysis of Stress and Strain in Soil", *J. Soil Mechanics and Foundation Division*, ASCE, Vol. 96, No. SM5, pp. 1629 – 1653.

Florida Department of Transportation (FDOT, 1996), Standard Specifications for Road and Bridge Construction, Section 430, pp. 392-393.

Finn, W. D. L., Barton, Y. O., and Towhata, I. (1983), "Seismic Response of Offshore Pile Foundation: Centrifuge data and Analyses", *Proc. 7th Pan-American Conference on Soil Mech. Found. Eng.* Vancouver, British Columbia, Canada.

Georgiadis, S. M., Anagnostopoulos, C., and Saflekou, S. (1991), "Centrifugal testing of laterally Loaded Piles in Sand", *Canadian Geotechnical Journal*, Vol. 27, pp. 208 - 216.

Glick, F. H., (1948), "Influence of soft ground in the design of long piles", 2nd *ICSMFE*, Vol. 4, pp. 84 - 88.

Hagerty, D. J., (1975), "Lateral Stress Related to Driven Piles", Lateral Soil Pressures Generated by Pipes, Piles, Tunnels and Caissons, ASCE, pp. 1 – 30.

Kondner, R. L., (1963), "Hyperbolic Stress-Strain response: Cohesive Soils.", *J. Soil Mech. Found. Div.*, ASCE, Vol. 89(1), pp. 115 - 143.

Li Yan, and Peter M. Byrne., (1992), "Lateral Pile Response to Monotonic Pile Head Loading", *Canadian Geotechnical Journal*, Vol. 29, pp. 955 - 970.

Murchison, J. M., and O'Neill, M. W., (1984), "Evaluation of P-Y Relationship in Cohesionless Soils.", In Analysis and Design of Pile Foundation, ASCE, New York, pp. 174 - 191.

Prakash, S., and Sharma, H. D., (1990), "Pile Foundations in Engineering Practice.", John Wiley & Sons, Inc.

Pyke, R., and Beikae, M., (1984), "A new Solution for the Resistance of Single piles to Lateral Loading", Laterally Loaded Deep Foundation: Analysis and Performance, ASTM STP 835, pp. 3 - 20.

Reese, L. C, Cox, W. R., and Koop, F. D., (1974), "Analysis of Laterally Loaded Piles in Sand", *Proc. 6th offshore Technology Conference*, Houston, Tex., paper OTC 2080, pp. 473 - 483.

Scott, R. F., (1980), "Analysis of Centrifuge Pile Test: Simulation of Pile Driving", Report for the American Petroleum Institute, OSAPR Project 13, California Institute of Technology, Pasadena, Calif.

Ting, J. M., Claudis, R. K., and Maryann, L., (1986), "Centrifuge Static and Dynamic Lateral Pile Behavior", *Canadian Geotechnical Journal*, Vol. 24, pp. 198 - 207.

Ting, J. M., (1987), "Full - Scale Dynamic lateral Pile Response", *J. Geotechnical Eng.*, ASCE, Vol. 113, No. 1, pp. 30 - 45.

Trevor, D. S., (1987), "Pile Horizontal Soil Modulus Values", *J. Geotechnical Eng.*, ASCE, Vol. 113, No. 9, pp. 1040 – 1044.

Tsinker, G. P., (1988), "Pile Jetting", *Journal of Geotechnical Eng.*, ASCE, Vol. 114, No. 3, pp. 326 - 334.

Vesic, A. S., (1972), "Expansion of Cavities in Infinite Soil Mass", *J. Soil Mechanics and Foundation Division*, ASCE, Vol. 98, No. SM3, pp. 265 – 290.

Weding Kaiser Aluminum (1967), Kaiser Aluminum & Chemical Sales, Inc., Kaiser Center, Oakland, California 94604.

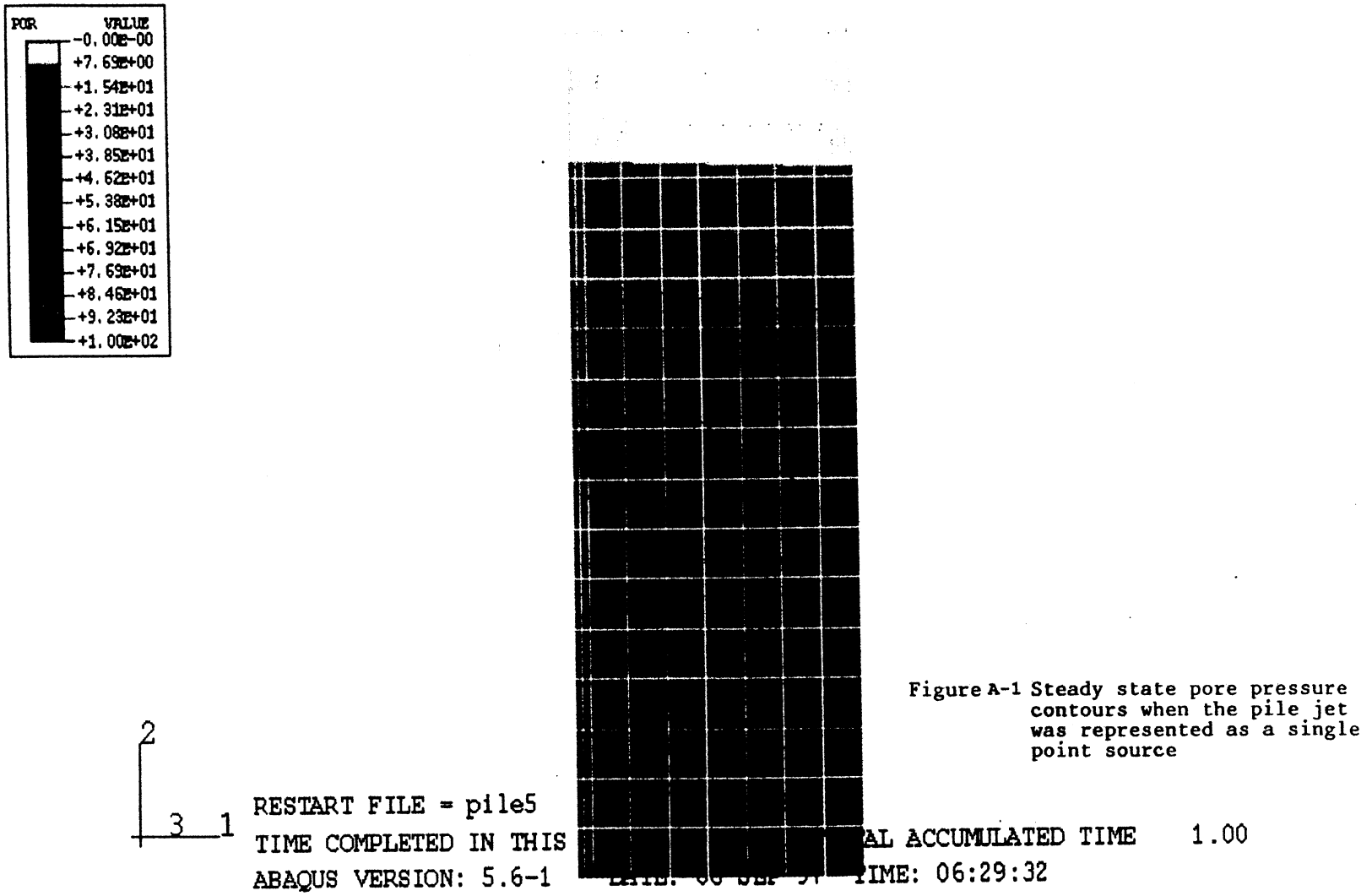

Figure A-1 Steady state pore pressure contours when the pile jet was represented as a single point source

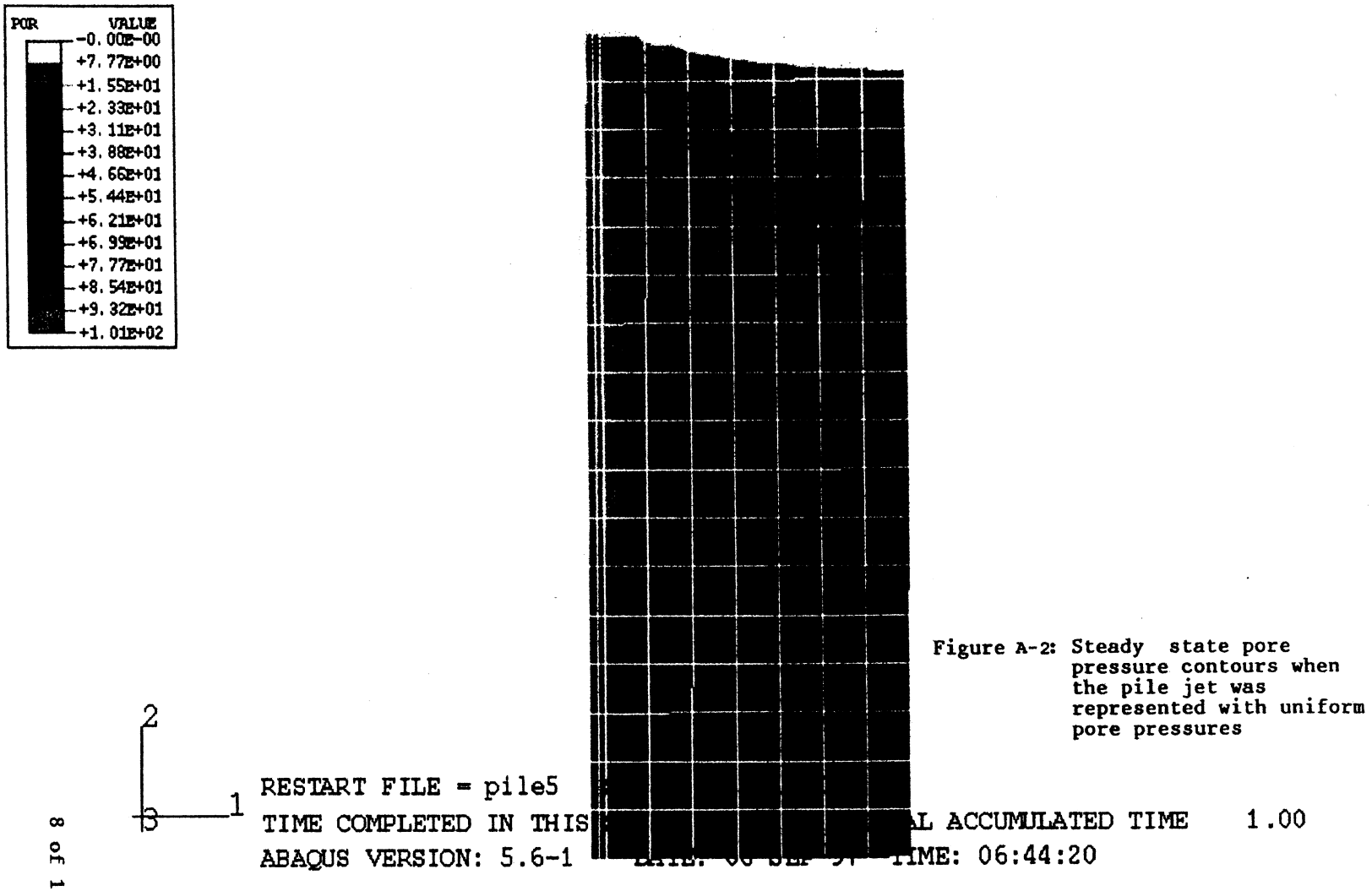

Figure A-2: Steady state pore pressure contours when the pile jet was represented with uniform pore pressures

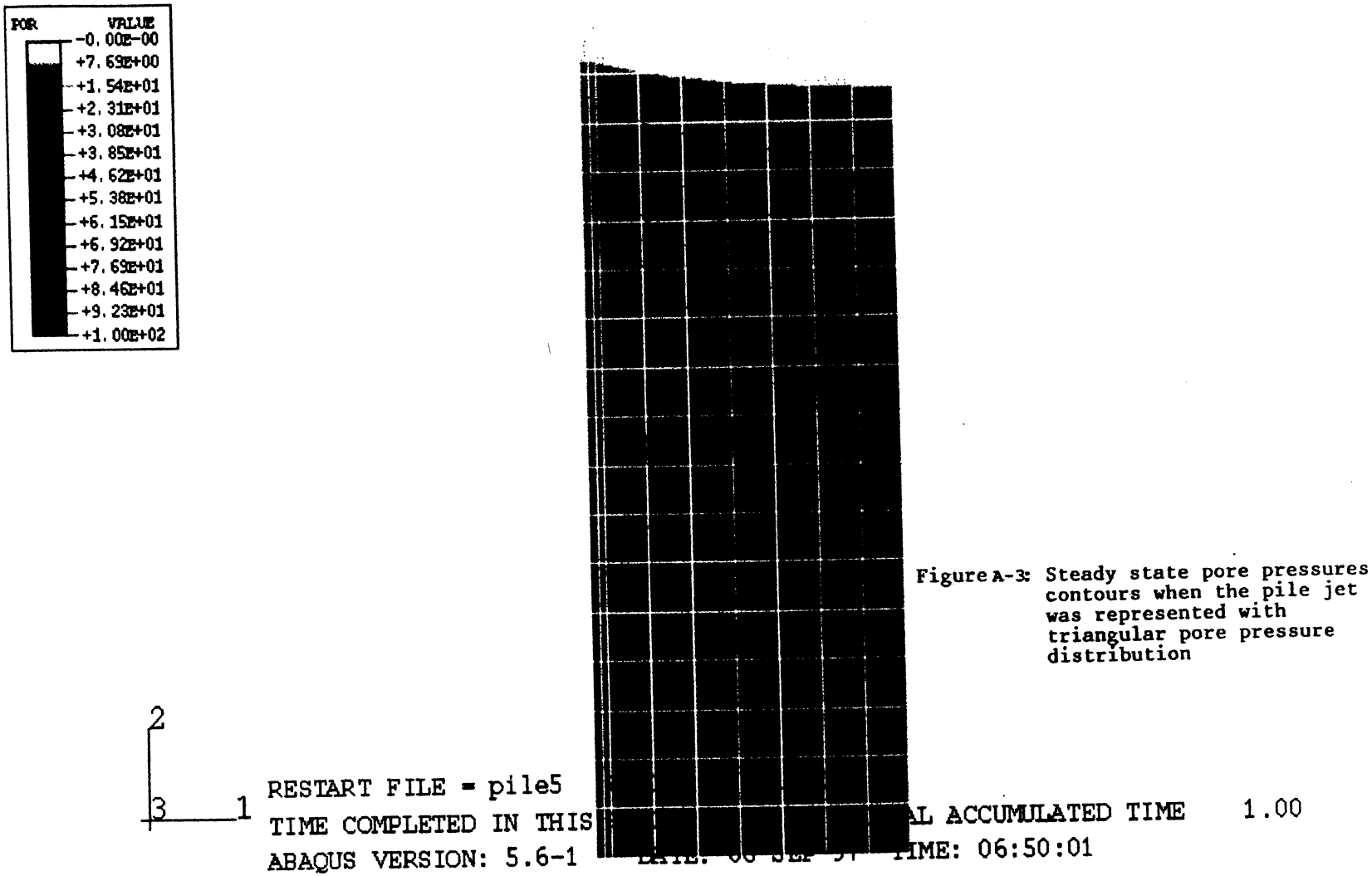

Figure A-3: Steady state pore pressures contours when the pile jet was represented with triangular pore pressure distribution

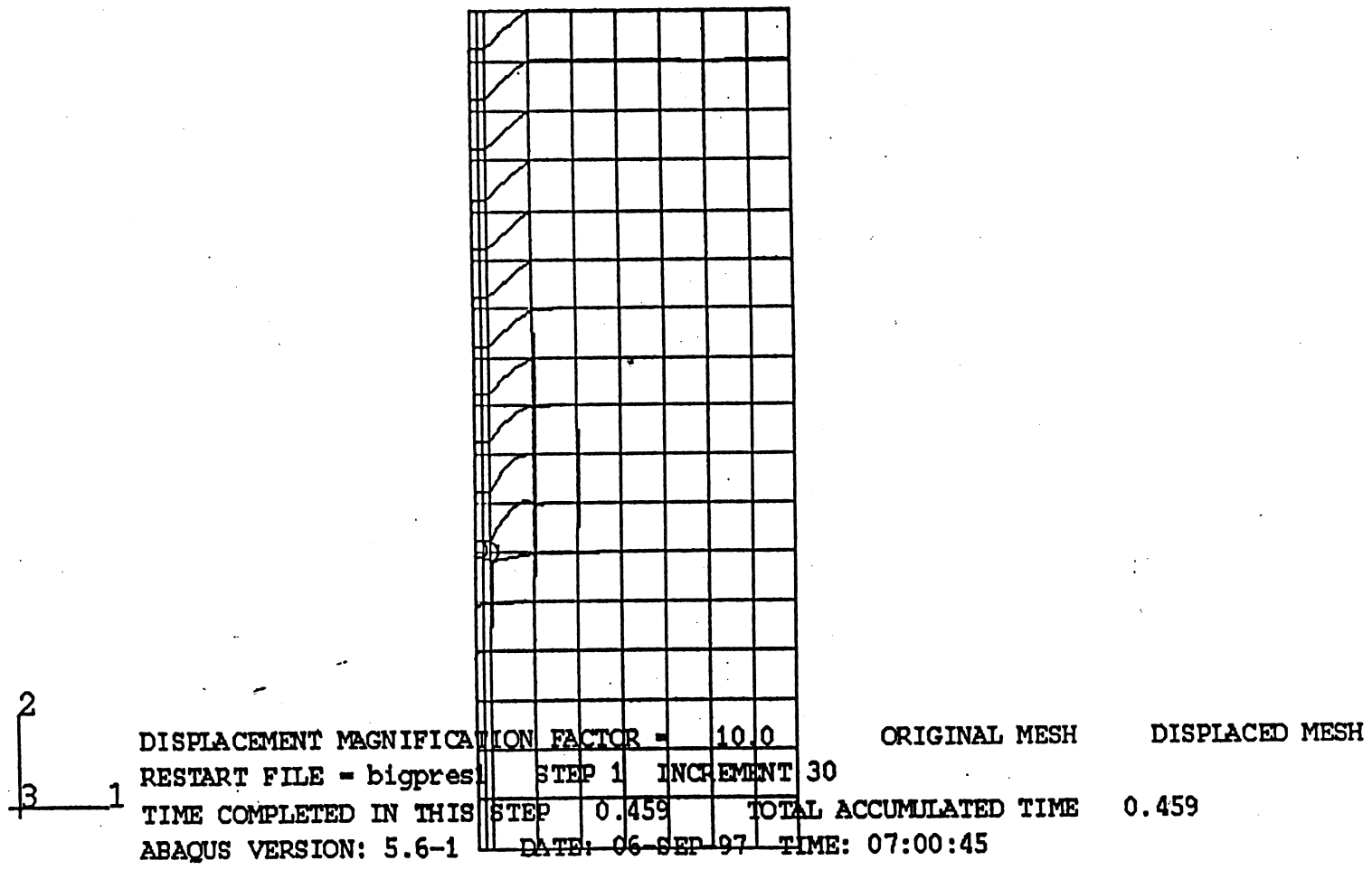

Fig. A4. Deformed shape of finite element mesh at the end of pile test

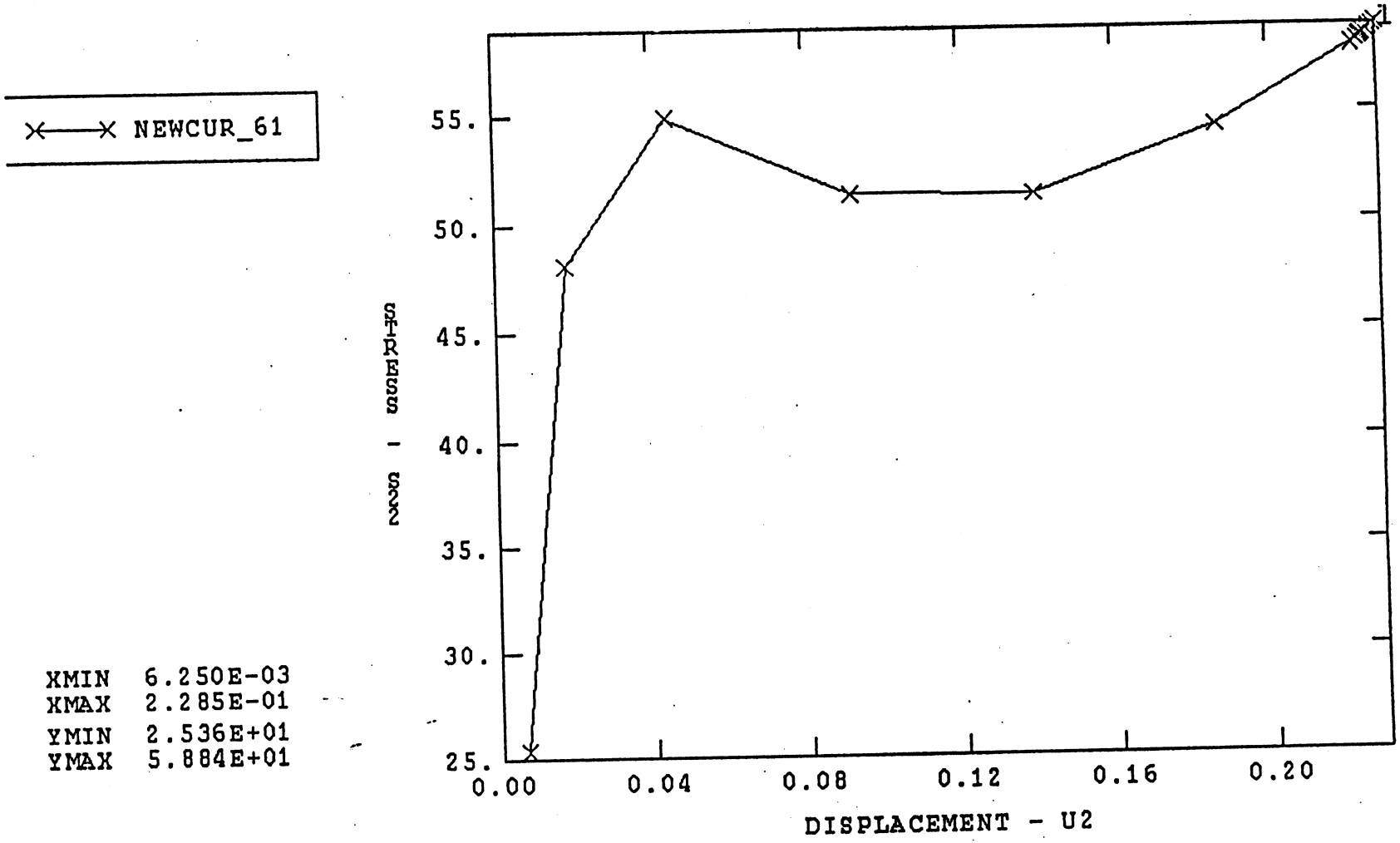

Fig. A5. Variation of vertical stresses in soil below the pile during the pile load test

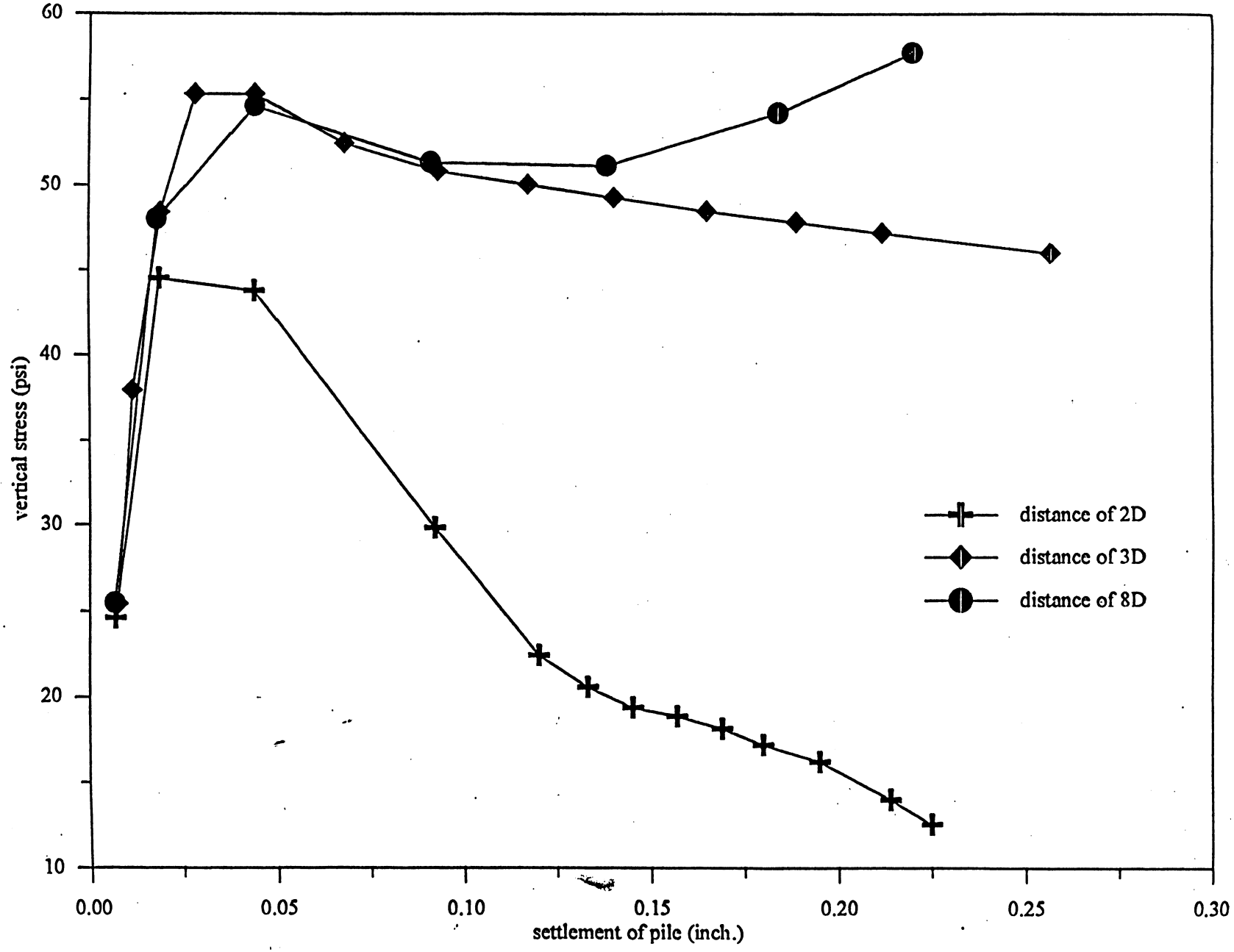

FIG.A6. Comparison of pile response to water jet at various distances